AD NUMBER

ADB008854

LIMITATION CHANGES

TO:

Approved for public release; distribution is unlimited.

FROM:

Distribution authorized to U.S. Gov't. agencies only; Test and Evaluation; 20 DEC 1974. Other requests shall be referred to Army Missile Command, AMSMI-RG, Redstone Arsenal, AL 35809.

AUTHORITY

usamicom notice, 10 mar 1977

TECHNICAL REPORT RG-75-24

SECOND BREAKDOWN IN THE PRESENCE OF INTENSE IONIZING RADIATION

Duane H. Pontius, Wallace B. Smith,
Aradhana Baruah, and Paul P. Budenstein
Physics Department
Auburn University
Auburn, Alabama 35830

Prepared for:

Guidance and Control Directorate
US Army Missile Research, Development and Engineering Laboratory
US Army Missile Command
Redstone Arsenal, Alabama 35809

20 December 1974

U.S. ARMY MISSILE COMMAND
Redstone Arsenal, Alabama

DISPOSITION INSTRUCTIONS

DESTROY THIS REPORT WHEN IT IS NO LONGER NEEDED. DO NOT RETURN IT TO THE ORIGINATOR.

DISCLAIMER

THE FINDINGS IN THIS REPORT ARE NOT TO BE CONSTRUED AS AN OFFICIAL DEPARTMENT OF THE ARMY POSITION UNLESS SO DESIGNATED BY OTHER AUTHORIZED DOCUMENTS.

TRADE NAMES

USE OF TRADE NAMES OR MANUFACTURERS IN THIS REPORT DOES NOT CONSTITUTE AN OFFICIAL INDORSEMENT OR APPROVAL OF THE USE OF SUCH COMMERCIAL HARDWARE OR SOFTWARE.

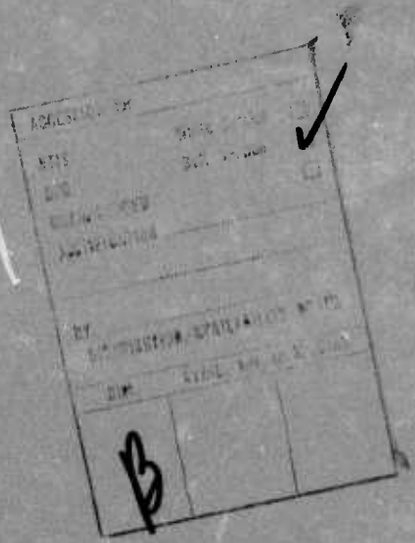

UNCLASSIFIED

SECURITY CLASSIFICATION OF THIS PAGE (When Data Entered)

REPORT DOCUMENTATION PAGE

READ INSTRUCTIONS BEFORE COMPLETING FORM

1. REPORT NUMBER: RG-75-24	2. GOVT ACCESSION NO.
3. RECIPIENT'S CATALOG NUMBER	
4. TITLE (and Subtitle): SECOND BREAKDOWN IN THE PRESENCE OF INTENSE IONIZING RADIATION.	5. TYPE OF REPORT & PERIOD COVERED: Technical Report
6. PERFORMING ORG. REPORT NUMBER: RG-75-24	
7. AUTHOR(s): Duane H. Pontius, Wallace B. Smith, Aradhana Baruah and Paul P. Budenstein, Auburn University	8. CONTRACT OR GRANT NUMBER(s)
9. PERFORMING ORGANIZATION NAME AND ADDRESS: US Army Missile Research, Development and Engineering Laboratory, US Army Missile Command, Redstone Arsenal, Alabama 35809	10. PROGRAM ELEMENT, PROJECT, TASK AREA & WORK UNIT NUMBERS: AMCMS Code 691000.22.10799
11. CONTROLLING OFFICE NAME AND ADDRESS	12. REPORT DATE: 20 December 1974; NUMBER OF PAGES: 83
14. MONITORING AGENCY NAME & ADDRESS (if different from Controlling Office)	15. SECURITY CLASS. (of this report): UNCLASSIFIED
	15a. DECLASSIFICATION/DOWNGRADING SCHEDULE

16. DISTRIBUTION STATEMENT (of this Report)

Distribution limited to US Government agencies only; test and evaluation; 20 December 1974. Other requests for this document must be referred to AMSMI-RG.

17. DISTRIBUTION STATEMENT (of the abstract entered in Block 20, if different from Report)

18. SUPPLEMENTARY NOTES

19. KEY WORDS (Continue on reverse side if necessary and identify by block number)

$p^+ - n - p^+$

20. ABSTRACT (Continue on reverse side if necessary and identify by block number)

The role of intense pulses of ionizing radiation on the second breakdown transition is investigated using silicon-on-sapphire $p^+ - n - p^+$ diodes. Superimposed on a high amplitude current pulse is a pulse of intense ionizing radiation from a Q-switched neodymium-glass laser. Photocurrents proportional to the radiation intensity are observed all the way to the threshold of damage by laser irradiation alone. The photocurrents do not affect the second breakdown transition until the intensity of the laser beam is close to that for

CONTINUED

DD FORM 1 JAN 73 1473 EDITION OF 1 NOV 65 IS OBSOLETE

UNCLASSIFIED

SECURITY CLASSIFICATION OF THIS PAGE (When Data Entered)

405 564

Block 20 Abstract continued

destruction by the laser alone. In this regime, for diodes of high n-region resistivity, the second breakdown transition is delayed by the presence of the photocurrent pulse. This delay is associated with circuit inductance; the photocurrent spike drives the voltage across the device to a low value or even reverses its polarity. Recovery of the voltage occurs with a time constant determined by the circuit. This is sufficient time for the junction, previously heated by a current pulse, to cool appreciably. No detectable change in delay time occurs for diodes having an n-region carrier density comparable to that produced by the photopulse or for forward biased diodes. In a study of the damage produced by the laser beam alone, no heating effects are detectable right up to the damage threshold. Damage occurs by vaporization of the silicon; the absorption coefficient of silicon changes within a few nanoseconds by more than a factor of 10 at the damage threshold. The mechanism of absorption is unknown. Second breakdown behavior is described in SOS diodes using double pulse excitation. Second breakdown in thin film MOSFET devices is described for several device geometries. Other studies include filamentation in plane silicon films, dynamic temperature measurements on SOS diodes, annealing of second breakdown damage, and microstructure of bulk transistors.

CONTENTS

ACKNOWLEDGEMENTS

The authors wish to acknowledge the craftmanship of D. Holt in making the Berg-Barrett camera, the kindness of R. A. Young (Georgia Institute of Technology) for allowing us to copy his Berg-Barrett camera, the aid of R. B. Mosley in computer programming, the generosity of D. J. Dumin (Inselek Corporation) for providing a silicon-on-sapphire wafer with transistors, the aid of J. D. Holder (US Army Missile Command) in transferal and operation of the laser, the encouragement of our technical supervisor, David Mathews (US Army Missile Command), the kindness of W. Raburn (University of Alabama) for providing the transistor specimens, and the efficient and cooperative help of our secretaries, A. J. Hawkins and P. L. Ray, during preparation of the final manuscript.

1. Introduction

Second breakdown is a descriptive term that covers a range of current filamentation phenomena in junction systems. Phenomenologically, it is a transition to a high conductance state that occurs at high current densities. If the external circuit constrains the total current in the device to be constant, the transition is accompanied by a voltage drop. The current and temperature distributions in the system change dynamically during the filamentation process; these changes cannot be modelled as a succession of steady state conditions. For many years, it was not possible to pin down the basic mechanisms associated with second breakdown, although numerous plausible suggestions were made and each contained merits. The breakthrough for delineating the correct mechanisms came with the work of Sunshine and Lampert [1-4]. Our own studies [5-8] followed, using the stroboscopic method developed by Sunshine. The stroboscopic method allows instantaneous current distributions to be observed in transparent thin-film silicon devices because the transmissivity is a strong function of the film temperature. From studies of silicon-on-sapphire thin film diodes, the following description of second breakdown has emerged [1-8]. The features of this description are consistent with the phenomena reported for three-dimensional systems of many different geometries and hence, we believe, are truly descriptive of second breakdown.

The geometry of a silicon-on-sapphire diode as used in References 5-8 is shown in Figure 1. Diodes of different base resistivities and different geometries were studied, but the most fruitful results came from the more highly-doped systems with wide n-regions and large size (21 mils diode width). Testing was done with constant current pulses, generally maintaining a fixed pulse length and varying the amplitude during a testing sequence. For low amplitude pulses of 100-μsec duration in a reverse-biased diode with a current density of about 4×10^3 Å/cm^2, the junction avalanched with a beaded light emission, but no noticeable heating of the device. Increase of the current by a factor of five made the avalanche light emission more intense and uniform over the junction and caused a perceptible rise in the junction temperature. With a slight additional increase in the current amplitude, the junction temperature increased greatly and, just a few microseconds before each pulse terminated, a tiny dark spot (hot spot) appeared in the junction when viewed stroboscopically in transmitted light. This was the start of current filamentation. The voltage across the device did not change perceptibly when the dark spot appeared. With further increase in the current amplitude, the dark spot occurred earlier in the pulse and several additional dark spots appeared. The number of dark spots (junction channels) increased with increasing current up to a saturation number for a given pulse duration. Further increase in current caused enlargement of the existing dark spots.

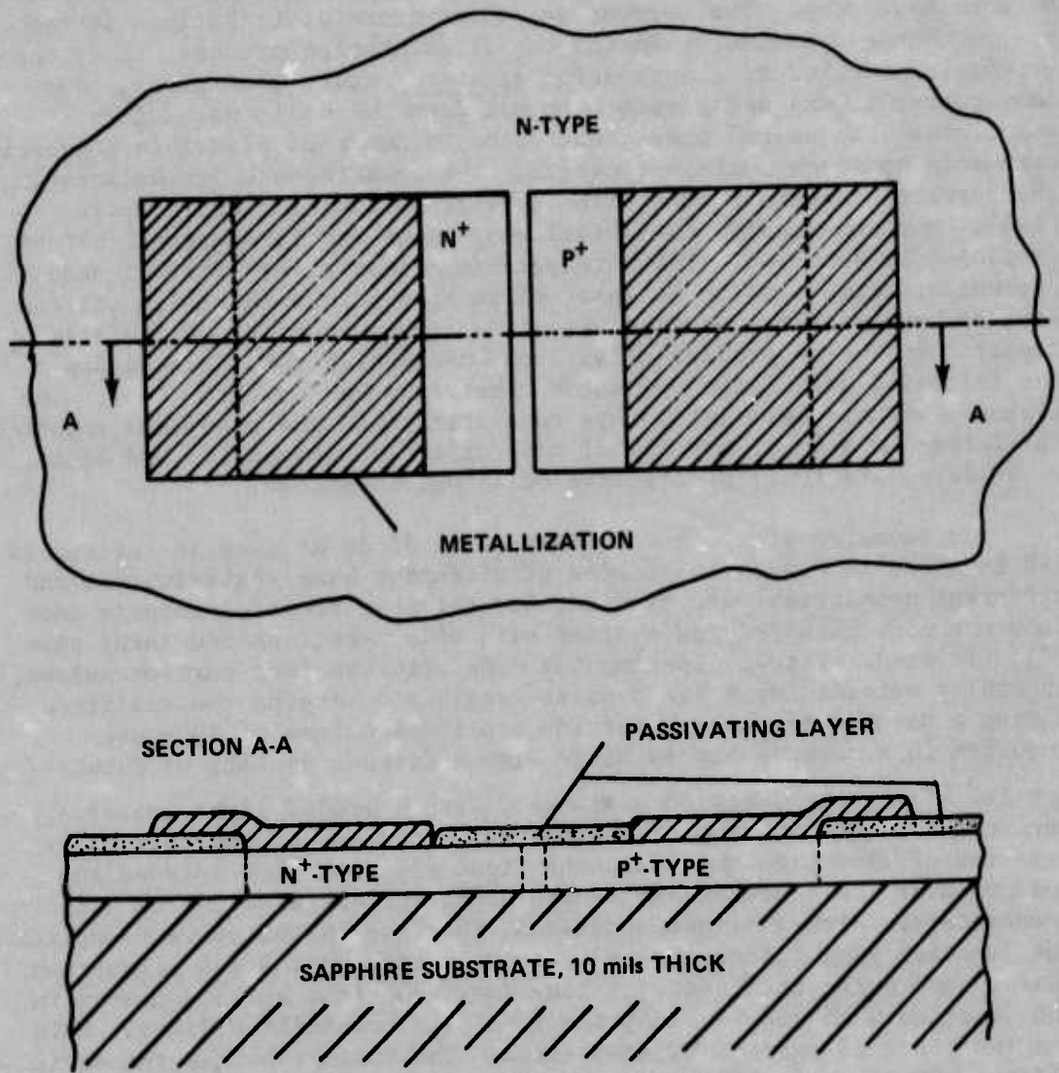

Figure 1. Silicon-on-sapphire diode geometry. (Doping materials are diffused into an n-type silicon film to form p^+ and n^+ regions. Metallizations are of aluminum, and the passivating layers are thermally grown oxide.)

The dark spots were strong thermal emitters while the regions of the junction adjacent to each dark spot were cool and nonemitting. (These cool regions had to be biased at a voltage less than the avalanche voltage because they emitted no avalanche radiation.) Thus current was funneling through the hot junction channels, and the junction regions adjacent to each were cut off. This implies that the voltage across the junction at each channel was very low and there was a large voltage gradient along the junction (associated with the converging current). Analysis shows that the voltage drop occurs at a junction site when the thermally generated current density becomes about 0.8 times the original current density. Each of the current channels is ballasted by the spreading resistance of the converging current and the series resistance of the relatively cool n-region. No voltage drop is observed when junction channels originate, so the onset of junction channeling has not in the past been taken as the start of second breakdown.

With further increase in current amplitude, each of the dark regions grows from the junction toward the opposite edge of the n-region. Growth occurs as the temperature of the filament edge goes over the peak of the resistivity-temperature curve (see ρ_{max} in Figure 2). Once over this peak the resistivity drops with rising temperature and more current tends to converge on the hot filament. The temperature at the center of the filament is estimated to be over 1000°C. Growth of the filaments is accompanied by a voltage drop; this is the nondestructive form of second breakdown (the form described by Sunshine and Lampert). If the current amplitude is further increased, one of the filaments will reach through the n-region and, because it is no longer adequately ballasted, its interior temperature will rise abruptly to the melting point and a narrow melt channel will form across the n-region. As the melt channel grows, the voltage across the filament (and the terminal voltage for the device) drops abruptly; this is the destructive form of second breakdown. The melt reaches a diameter of about 1 μm for pulses near threshold, but it may be much larger for higher amplitude pulses. Figure 3 shows voltage and current waveforms from a silicon-on-sapphire diode (of 21 mils width and with n-region resistivity of 0.064 ohm-cm) for the phenomena described above. Figure 4 shows the diode illuminated by the strobe light prior to pulse testing (transmission light photograph), the same diode examined by the transmitted light during pulse testing showing current filaments, and the low amplitude I-V characteristics before and after damage due to a single melt filament.

The number of junction channels that form prior to filament growth depends on the pulse length; as pulse length decreases the number of channels increases. The current amplitude for junction channel formation increases as pulse width decreases. Since the location of the channels is different for pulses of different length, it seems that inhomogeneities play only a secondary role in channel nucleation; the locations are determined primarily by the heat flow and electrical conduction equations.

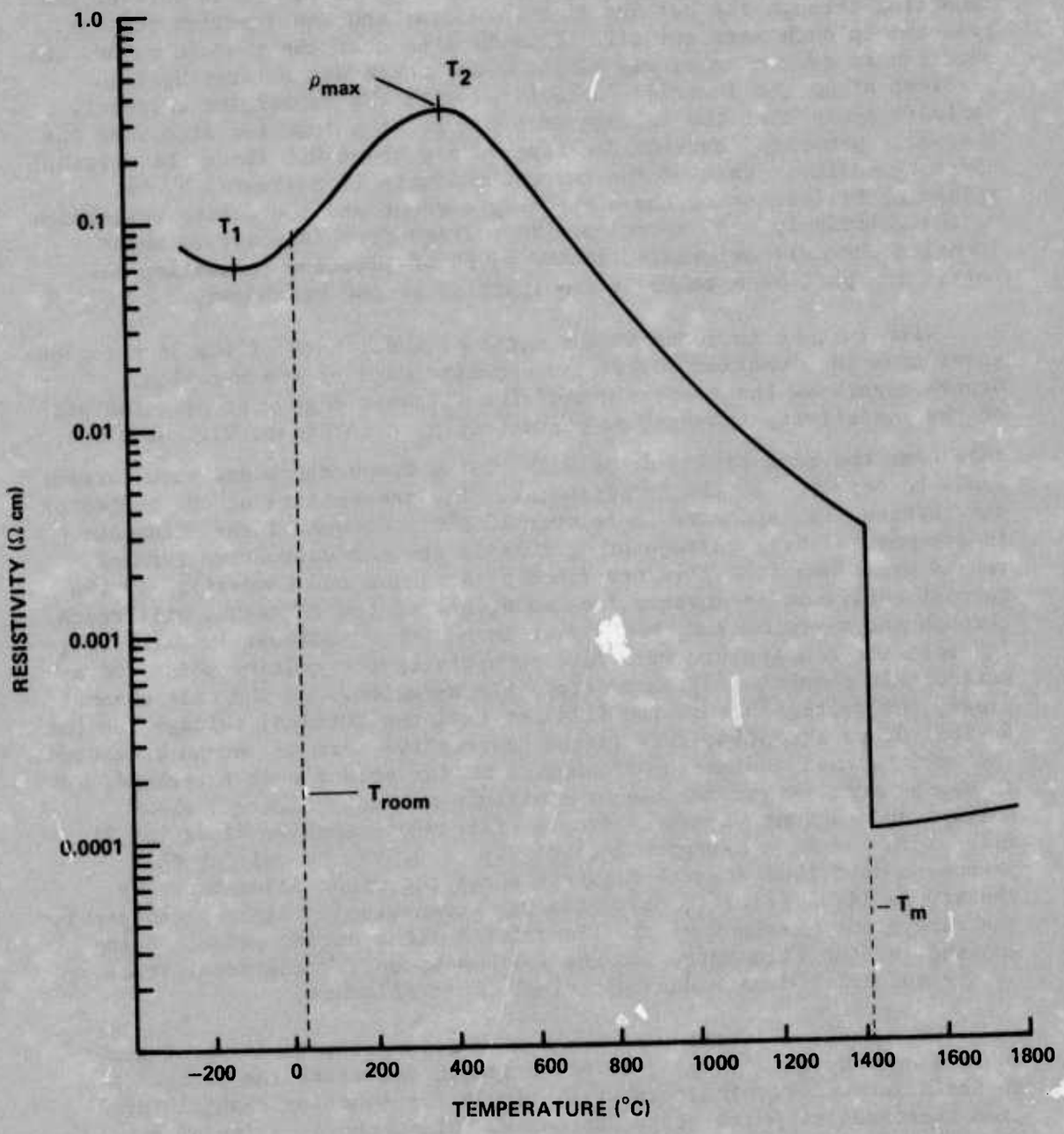

Figure 2. Resistivity as a function of temperature for n-type silicon having a doping density of 10^{17} cm^{-3}. (T_2 is the temperature of maximum resistivity, and T_m is the melting point of silicon.)

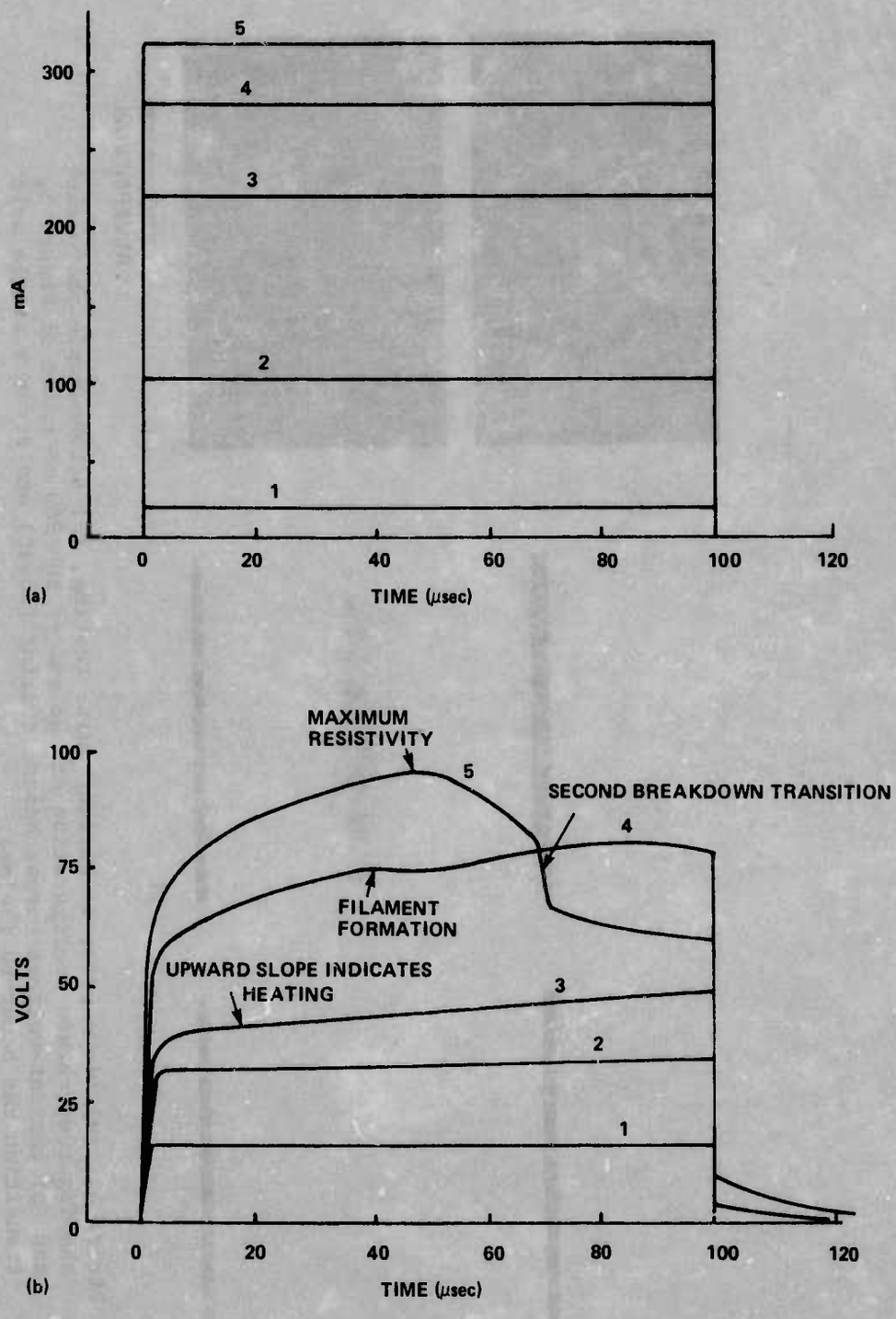

Figure 3. Current (a) and voltage (b) waveforms of second breakdown testing.

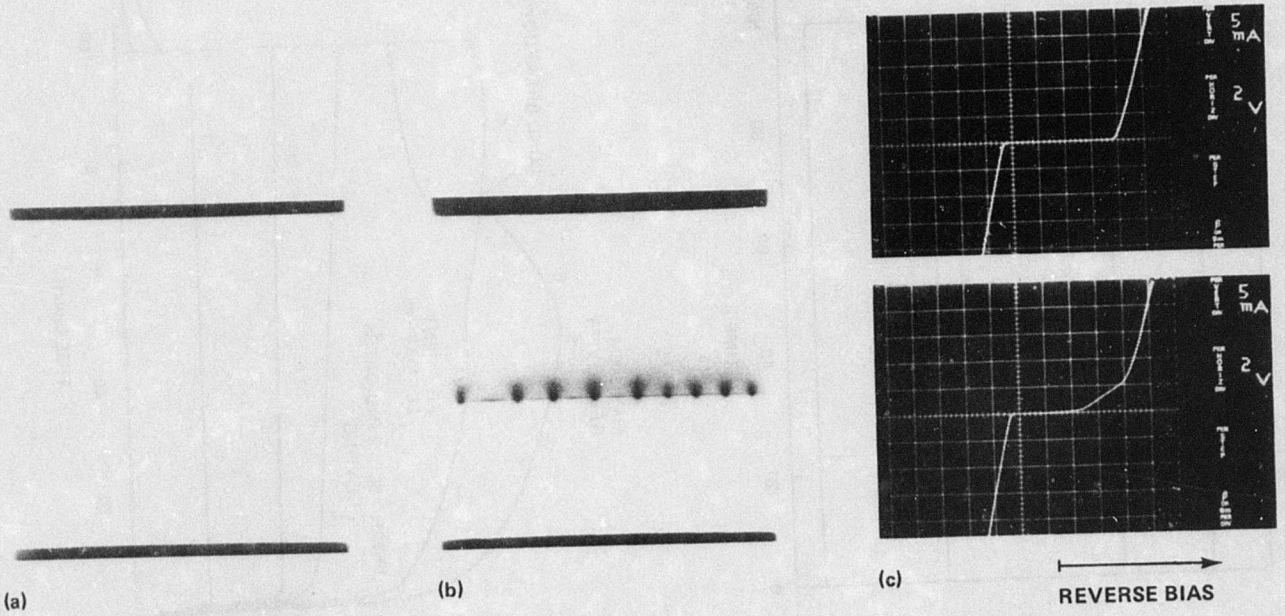

Figure 4. (a) Diode prior to current pulse testing, (b) stroboscopic photograph showing temperature configuration at the end of the 280 mA pulse of Figure 3, and (c) current-voltage curves before testing (above) and after a single melt transition has occurred (below).

In second breakdown studies, the time from the leading edge of the exciting pulse to the beginning of the voltage drop is called the delay time. For nondestructive second breakdown, the voltage drop starts after all filaments have nucleated, while for the destructive form the voltage drop occurs when the melt starts to grow. As can be seen in Curve 5 of Figure 3, these times are different. However, if the amplitude of the exciting pulse is increased far above threshold, then the two times occur in rapid succession. Filament growth involves heating of the n-region. At the threshold for melt formation, the portion of the n-region that is not part of the filament is at a temperature close to that of the peak of the temperature-resistivity curve. Thus the delay time (for destructive second breakdown) is associated with the heating of the n-region.

Sunshine and Lampert [4] made a detailed study of the delay time to second breakdown. Their silicon-on-sapphire diodes ranged in width from 12.5 to 100 μm, considerably smaller than those described above. Further, their light source for stroboscopic measurements was an AlGaAs laser operating at 7100 Å. This source was of relatively low intensity, high monochromaticity and at a wavelength where the human eye and photographic emulsions are insensitive. The high monochromaticity leads to interpretative problems because of interference effects in the thin silicon films, while the other source characteristics made it necessary to use image intensification methods for observing the diodes. This caused a loss of contrast, so that the stroboscopic method distinguished "cold" and "hot", but little in between. The dividing temperature was probably about 400°C. Thus, when they first perceived the junction dark spots, these were relatively well-developed. In the experiments described above, the transition to channeling could be made very gradual by carefully limiting the current amplitude or very abrupt by applying pulses of high amplitude. Thus the switching time from a state of nearly uniform avalanche conduction to that of a single filament, given as about 100 nsec by Sunshine and Lampert, is not a constant but a variable dependent on pulse amplitude.

The thermal time constant estimated by Sunshine and Lampert was about 5 μsec. This is probably a little shorter than the true time constant because of the small dynamic contrast range of their system. We find, for the same thicknesses of material, thermal time constants of about 10 μsec. In delay time measurements in the nanosecond range, Sunshine and Lampert did not find a constant energy input prior to the second breakdown transition (they used the voltage drop accompanying filament growth, the nondestructive form of second breakdown, as their criterion for the delay time), but they found that their data more closely fitted the relationship suggested by Flemming [9], $p\tau_d^{1/2}$ = constant. They regarded this behavior as a compromise between two effects: "On the one hand, the smaller τ_d is, the higher are the current density and the local temperature needed to quench the avalanche. On the other hand, the volume which is being heated is reduced. These

opposing effects tend to cancel, yielding the above described relation." They also discounted the assumptions made by Flemming in developing his equation.

In the description of second breakdown above, the delay time for the onset of destructive breakdown was related to the temperature of the n-region. When this temperature reached that corresponding to the peak of the temperature-resistivity curve, a filament would bridge the n-region and a melt channel would form. At high power levels, consistent with the results of Ferry and Dougal [10], the product $p\tau_d$ seemed to approach a constant value. The difference in criterion may explain the observed differences in the functional relationship between p and the delay time.

A portion of the recent literature reflects the state of knowledge prior to the stroboscopic studies. Since the events of second breakdown were not well-established, meaningful models were difficult to develop. Mars [11,12] assumed that current filamentation occurs when a spot in the junction reaches a critical temperature and he developed a spherical model of the constriction. He highly idealized the heat-flow problem, assuming that a steady state heat flow parallel to the current lines existed. By so doing and by using idealized functions for the thermal and electrical conductivities, he obtained an analytical expression for the voltage across the constricted region. His results give numbers of the correct order of magnitude for the voltage, size of the current constriction, and maximum temperature.

Tasca et al. [13] have attempted to develop a nondestructive method for screening devices resistant to second breakdown from those more prone to second breakdown. The intent was to guard against reduced second breakdown resistance when a manufacturer makes small changes in his procedures of fabricating a given device type. The authors regarded junction area and reverse bias depletion width as significant parameters. These, in turn, would influence junction capacitance, forward voltage drop and avalanche voltage. Tests were conducted on 225 IN4148 planar epitaxial passivated diodes fabricated similarly except that three different junction diffusion windows were used: 3-, 4.3-, and 6-mil square. A correlation was found between the 100-nsec second breakdown energy and the forward voltage at a forward current of 1 mA. The data presented show that more current is required to bring a device into second breakdown if the device's junction area is large, that is, current density is an important parameter. It is not clear that the method suggested would be useful if the manufacturer changed other aspects of device geometry besides the area. A second screening technique was to measure the energy required for the onset of the nondestructive form of second breakdown using a standard pulse length. The authors did not give details of the test circuit used, but it probably was not constant current pulses. Constant current testing, as emphasized by Sunshine, gives better control than does a circuit with constant external impedance.

Brown [14] applied pulses in the range of 3 to 55 nsec to high frequency transistors of known geometry in order to (1) determine the junction degradation produced as a function of pulse current, pulse power, and pulse duration, (2) develop a microscopic model for the degradation mechanism, and (3) suggest design modifications that would increase the tolerance of future devices to pulse degradation. The damage, regardless of the terminals used to excite the transistors, always appeared at the emitter-base junction. The apparent failure mechanism was the formation of conducting paths in parallel with the emitter-base junction, probably the result of localized junction melting during the application of a pulse. The author found that the current and power thresholds for damage exhibited power law dependences on the pulse length, a different exponential being required to describe each device. For eight different device types, pulse width dependences from $t_p^{-0.17}$ to $t_p^{-0.56}$ were obtained for the current at failure, while dependences from $t_p^{-0.32}$ to $t_p^{-0.84}$ were obtained for the power at failure. No perspective on the pulse length dependence could be given. However, the delay time studies described by Budenstein et al. [6,8] show that the pattern of current filamentation at the threshold of second breakdown is a function of pulse length. The filamentation pattern depends strongly upon device geometry. Brown concludes that the devices most resistant to second breakdown were those with the largest emitter peripheries and deep emitter diffusions. If we try to interpret these conclusions from the description of second breakdown given from the silicon-on-sapphire experiments, we believe the larger emitter periphery favors lower current density and hence less heating but we are not sure of the significance of the deep emitter diffusion. Experiments were also done on annealing of damage by placing devices in an oven (300°C for 1 hour) or by sending currents through the devices in a variety of arrangements (15 minutes). The transistor gain was monitored before pulsing, after damage, and after annealing. Each of the annealing procedures caused some improvement, but the one with the highest currents caused the greatest improvement. The amount of recovery varied with the device. No mechanism for annealing was suggested.

Voss [15] has shown that the radiation emitted at avalanche breakdown from large area high-voltage pn junctions and from pnp structures can be detected using an infrared converter in conjunction with a three-stage image intensifier. Patterns of the emitted light, which is buried well below the surface of the device, consisted of segments of circles and spirals, indicating an inhomogeneous breakdown across the area. The homogeneous breakdown is attributed to resistivity striations inside the silicon.

The filamentation phenomena associated with second breakdown have some similarity to that of switching in chalcogenide glasses. Warren [16] reviews the main features of chalcogenide glass switches and

interprets switching in terms of a thermal mechanism. It is shown that a simple one-dimensional model is insufficient for describing thin films, and several developments are discussed, including field-dependent effects, channeling instabilities, and electrode hot spots. Suggestions are offered on the direction that future theoretical and experimental efforts might take in order to separate the roles of thermal and electronic effects in the switching problem. Sheng et al. [17] have analyzed the pressure and frequency dependences of threshold voltage and switching delay time in chalcogenide glasses using a thermal model.

The principal goals of the current study were to determine experimentally the influence of short duration, highly intense pulses of ionizing radiation on the second breakdown transition and to place the observed phenomena in perspective with an appropriate theoretical interpretation. Secondary goals were to further characterize the phenomena associated with second breakdown and to develop convenient microstructure techniques for studying the damage due to second breakdown. The work performed will be described in the following sequence: Section 2 contains a description of the stroboscopic method, the arrangement of the pulsed laser used as the source of ionizing radiation, and a description of the microstructure techniques. Section 3 describes the synergistic experiment, the influence of simultaneous electrical and laser pulses on the second breakdown transition. Section 4 treats damage due to laser pulses alone. Sections 5 through 10 discuss filamentation in homogeneous films, temperature measurements during pulse testing, annealing tests, double pulse experiments, thin-film transistor experiments and microstructure studies. Finally, in Section 11, a summary of the entire effort is presented.

2. Experimental Methods

The stroboscopic method as it will be used in this study has been described in detail [6,8] so that it will be presented here only in summary form. Then a description of the laser system will be given, followed by an account of the techniques used for studying microstructure.

a. Stroboscopic Method

In the stroboscopic method, repetitive current pulses are applied to the test device. Synchronized with each current pulse is the flash of a strobe light, an adjustable delay allowing control of the position of the light flash relative to the leading edge of the current pulse. The strobe light is focused on the device under study and the transmitted light through the device is observed. Since devices were small, observations had to be made microscopically.

The experimental arrangement is shown in Figures 5 and 6. The light source was a Xenon Corporation Nanolamp, an air arc that could be triggered at a pulse repetition rate up to 100 pps. Each output pulse

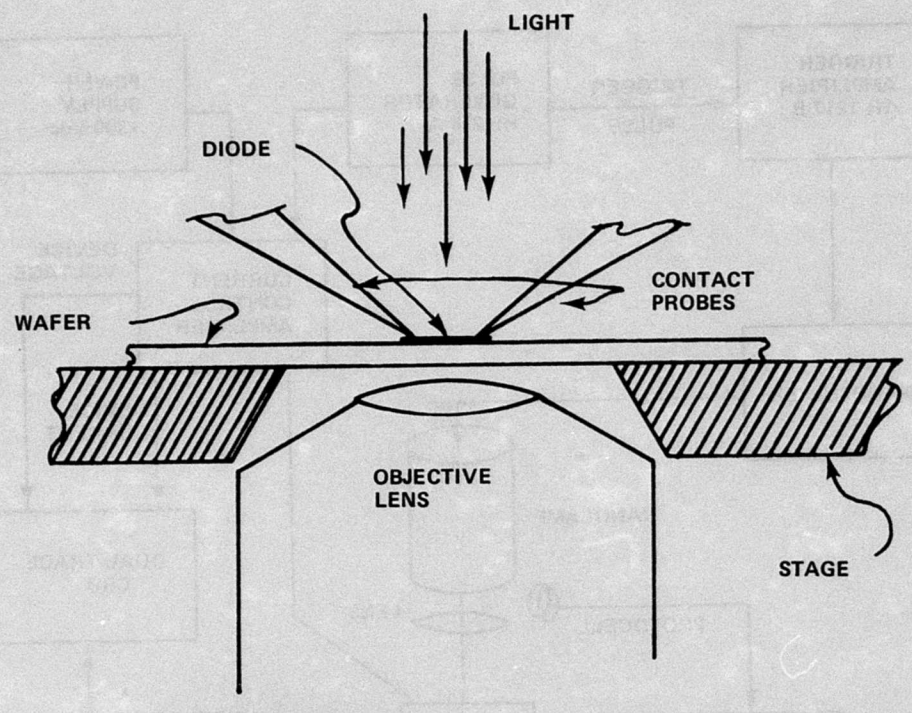

Figure 5. Experimental arrangement of the optical system used in making stroboscopic observations of transmitted light. (Light emitted due to avalanche conduction was observed by turning off the light source above the device.)

was approximately Gaussian in shape with half-power points about 20 nsec apart and peak power of about 50,000 W. Its spectrum was continuous so that interference effects in the thin film devices were not observed. The spectrum peaked at about 300 nm, falling to about 0.1 peak intensity at 600 nm. The light output varied ±20 percent over many flashes, so that quantitative studies required integrating over a large number of flashes. In a period of months, the intensity gradually decreased but, on the whole, the Nanolamp was a faithful and dependable light source well suited to these studies. On occasion, a grating monochromator was inserted between source and system to investigate the role of wavelength.

All of the specimens studies were thin film silicon devices on sapphire substrates. Substrates were optically polished on both sides, about 10 mils thick and from about 0.5 to 1.5 inches across. Diodes and homogeneous films were specially fabricated for these experiments by Autonetics Division, North American Rockwell, while transistors were fabricated by Inselek and provided through the courtesy of D. J. Dumin. Specimens were positioned on a specially constructed microscope stage, so that contacts could be made to any device on a substrate using pressure

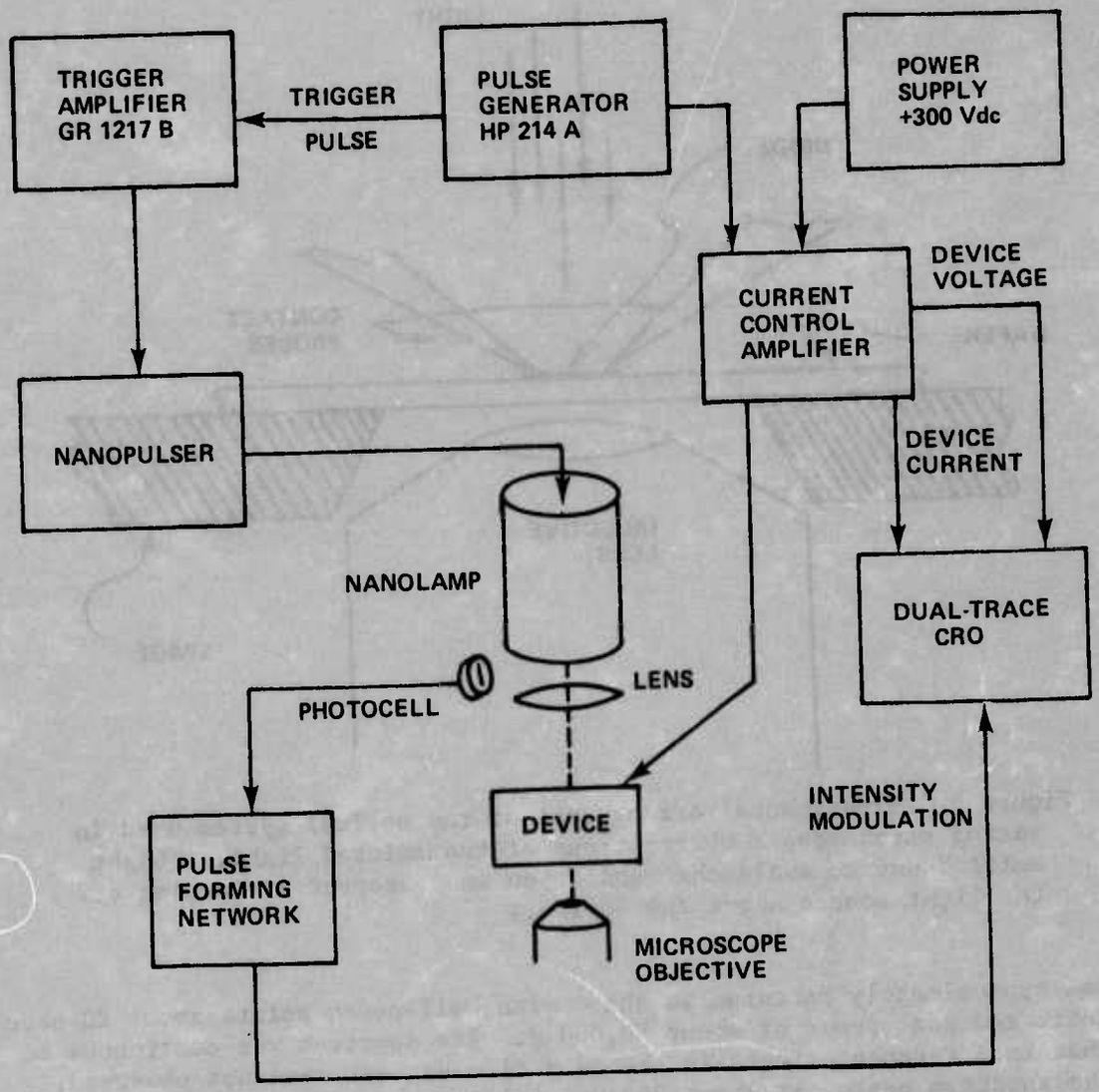

Figure 6. Block diagram of the stroboscopic system. (Electrical measurements were made using the dual-trace oscilloscope simultaneously with observations of thermal distributions through the microscope.)

probes and the device then positioned at the center of the field of an inverted microscope. Probes were positioned with the aid of a stereo-microscope located above the stage of the inverted microscope. The intensity of the strobe light was great enough that events could be readily followed using the regular optical system of the inverted microscope or data could be photographically recorded. Temperature changes in the devices cause a decrease in the optical transmittance, as indicated in the white light calibration curves of Figure 7. The transmittance changes by a factor of about 100 for a 700°C temperature change. Since photographic film can cover an intensity range of about a factor of 100,

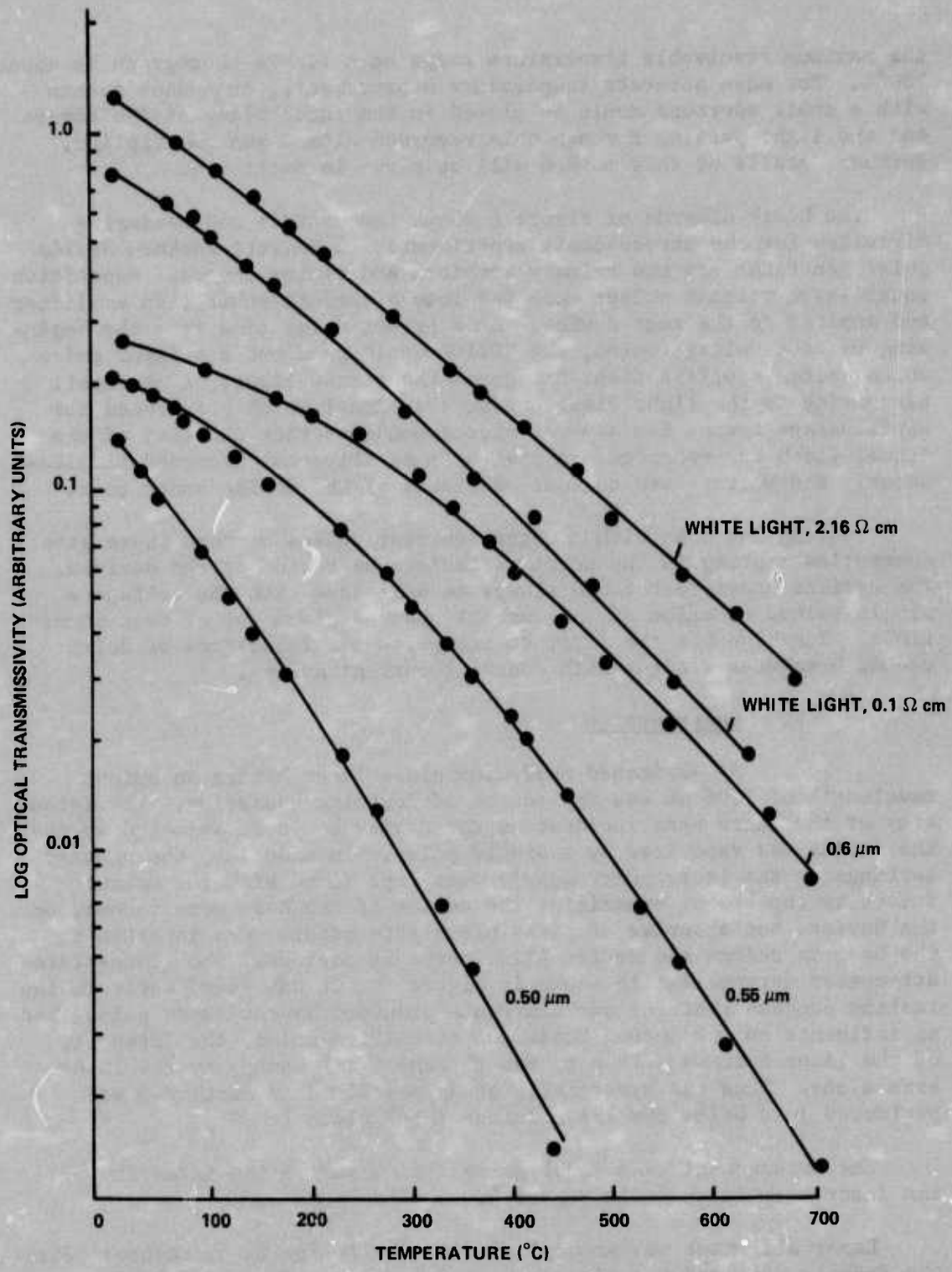

Figure 7. Optical transmittance of thin silicon films as a function of temperature. (The upper two curves are for white light, and the lower three for monochromatic light through a 0.1 ohm-cm film.)

the maximum resolvable temperature range on a single photograph is about 700°C. For more accurate temperature measurements, an opaque screen with a small aperture could be placed in the focal plane of the camera and the light passing through this recorded with a photomultiplier. Further details of this method will be given in Section 6.

The block diagram of Figure 6 shows the control and measuring circuitry for the stroboscopic experiments. A Hewlett-Packard HP214A pulse generator was the primary waveform and timing source. Repetitive square-wave voltage pulses were fed into a current-controlled amplifier and applied to the test device. At a preset delay time from the beginning of each voltage pulse, the HP214A would send out a trigger pulse which, after amplification, triggered the strobe light. A photocell responding to the light flash produced a signal which brightened the oscilloscope traces for several microseconds so that the time of the actual flash was recorded. A dual-beam oscilloscope recorded simultaneously the voltage and current waveforms of the device under test.

Testing was done with constant-current pulses because these gave controlled testing in the negative resistance region of the devices. The devices under test could always be described with the voltage a single-valued function of the current under a given set of test conditions. Sunshine was the first to recognize the importance of doing second breakdown studies with constant-current pulses.

b. Laser System

A Q-switched neodymium glass laser having an output wavelength of 1.06 μm was the source of ionizing radiation. The intensity of the laser beam incident on the device could be adjusted so that the device was vaporized by a single pulse. In practice, the voltage settings on the laser power supply were kept fixed with the output intensity capable of vaporizing the device if the beam were focused on the device, but a series of glass-plate attenuators were inserted in the beam to reduce the device illuminance as desired. The glass-plate attenuator arrangement is shown in Figure 8. It was found early in the testing program that the photocurrents produced by the laser pulses had no influence on the second breakdown transition unless the intensity of the laser beam was close to the threshold for damage by the laser beam alone. Thus the synergistic study described in Section 3 was performed just below the laser damage threshold.

The arrangement used in aligning and measuring the intensity of the laser beam is shown in Figure 9.

Laser alignment was accomplished by the following procedure: First the Pockels cell and the mirrors M_1 and M_2 were removed from the system and a ground glass screen was placed in front of the Nd rod at position A. The position of the He-Ne alignment laser was adjusted so that the beam passed through the center of both of the end faces of the neodymium

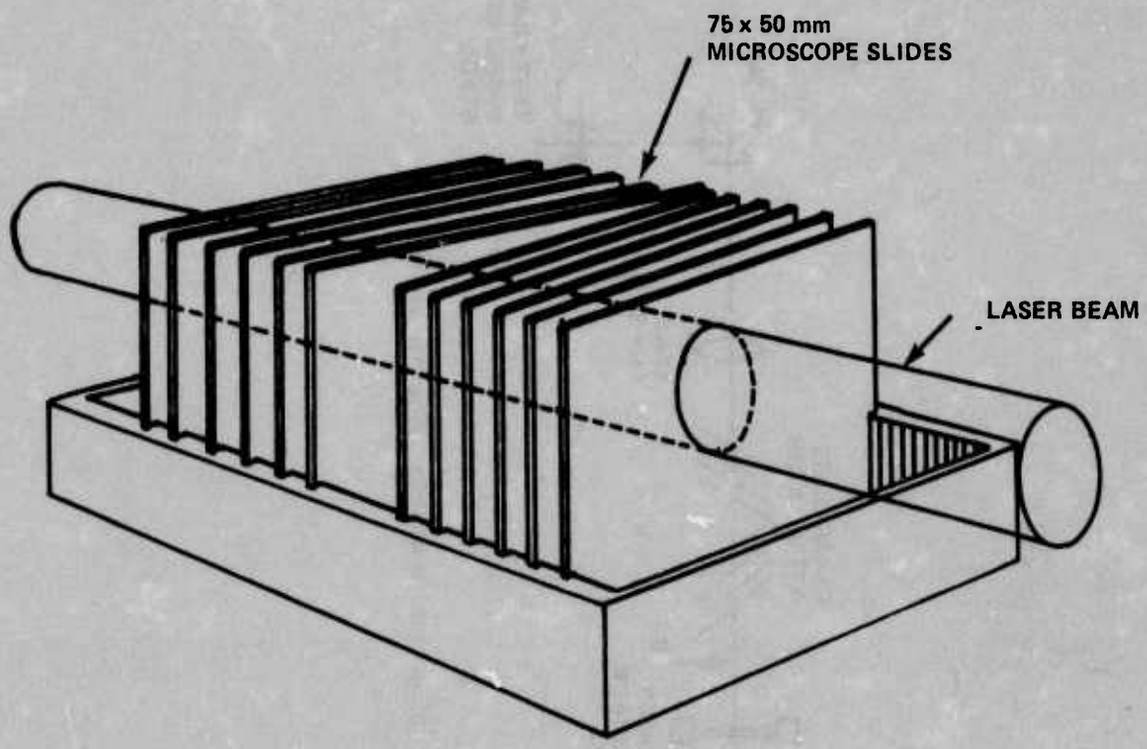

Figure 8. Glass plate attenuator for laser system. (Normal to each plate is at an angle of approximately 3.5 degrees with the direction of the laser beam.)

rod. Multiple reflections from the ends of the Nd rod produced a pattern of spots on the screen. By fine adjustment of the alignment laser the spots can be made to merge into a single spot. The beam of the alignment laser is now parallel to the axis of the Nd rod. The ground glass is then moved away to position B and the front mirror M_1, in a gimballed mount, is positioned. Multiple reflections between M_1 and the face of the Nd rod again produce a spot pattern on the ground glass, which, when merged to a single spot by adjustment of M_1 only, indicates that the front mirror is aligned with its normal parallel to the alignment beam. The rear mirror M_2 is then positioned in exactly the same manner, without changing any of the positions of the components already aligned. Finally, the Pockels cell, with the Brewster's angle glass polarizer attached, is placed in position. Alignment of this component is the least critical operation in the procedure. Reflections on the rear mirror M_2 are sufficient to estimate alignment of the Pockels cell. Multiple reflections from the many surfaces in the cell

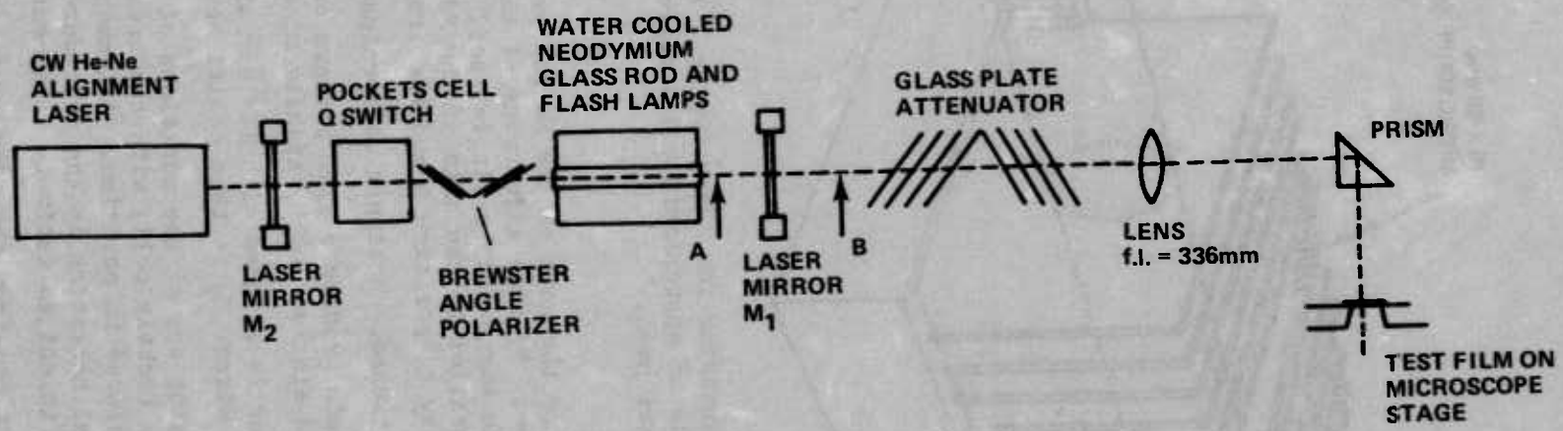

Figure 9. Arrangement used in aligning and measuring the intensity of the Q-switched Nd-glass laser.

and polarizer produce an array of spots which cannot be converged to a single spot. But it is generally not difficult to recognize principal bright spots and cause them to coincide. After placing the protective enclosure over the Pockels cell and rear mirror and removing the ground glass screen from B, the neodymium laser is ready for operation.

The beam from the laser was passed through a system of attenuators and lenses to apply ionizing radiation on the microscope stage over an area a few times larger than the area of the silicon-on-sapphire devices to be examined. A long focal length lens (f.l. = 336 mm) was used to converge the beam slightly, and a short focal length lens (f.l. = 25 mm) placed above the microscope stage provided for the final convergence to the desired area. A right-angle prism above the short focal length lens was used to direct the beam downward. The 336 mm lens could be moved back and forth slightly, along the direction of the beam to make fine adjustments in the radiation intensity at the microscope stage.

With no attenuation in the beam, the laser radiation was sufficiently intense to vaporize the silicon layer. The method used for attenuation was based on reflection losses in a beam passing through glass plates placed at a small angle to the wavefront. In order to make intensity measurements the beam was first attenuated to a level below the damage threshold by increasing the number of glass plates (50 × 75 mm microscope slides) in the beam until no damage was observed in a test silicon-on-sapphire film.

The radiation level at the microscope stage was then measured by placing a homogeneous silicon-on-sapphire film on the stage and observing the amplitude of photocurrent pulses produced by laser irradiation. Rectangular films 100-μm^2, of various resistivities were available for these measurements. Radiation intensity was calculated using [18]

$$\dot{\gamma} = I_p/(qg_o V_{eff}) \quad ,$$

where $\dot{\gamma}$ is the radiation energy deposition rate (rd/sec), I_p is the photo-current amplitude, q is the electronic charge, and V_{eff} is the effective volume of the irradiated device (taken to be the total volume in these 100-μm^2 thin film devices). The quantity g_o is the number of electron-hole pairs generated per unit volume of silicon by one rad of ionizing radiation ($g_o = 4.0 \times 10^{13}$ carrier pairs/cm^3 rd). For the level just below the damage threshold, a radiation level of approximately 2×10^{11} rd/sec was found. At this intensity, a single 20-nsec laser pulse yields a total dose of approximately 4×10^3 rd (Si), generating about 1.6×10^{17} carrier pairs/cm^3.

In order to construct standard attenuators for the system, glass plates were inserted in the beam until the intensity measured at the microscope stage dropped to one tenth (or any desired fraction) of the first measured value. These plates were then mounted so that they could be inserted into the beam, or removed quickly and conveniently. Several such attenuators were constructed, so that by making a single measurement of radiation intensity, known values of intensity over a range of several orders of magnitude could be obtained by inserting attenuators in the beam.

A simple monitor was constructed from a large (1 × 1 cm) homogeneous silicon-on-sapphire film with pressure contacts at the edges. The monitor was not calibrated, but was used to observe variations in the laser output during the experiments. The monitor was mounted in a position to intercept part of the radiation rejected by the attenuator system. As long as the geometry was kept constant, photopulses generated in the monitor indicated the relative variations in successive pulses of the laser. The photo-current pulses normally varied by up to ±10 percent on single shots. An average over 10 pulses showed variations of about ±3 percent.

As a general procedure to produce a desired level of radiation, the beam was first attenuated to well below the damage threshold. A small homogeneous silicon-on-sapphire film was placed on the microscope stage, and a measurement was made. The position of the 336-mm lens was adjusted to produce either the desired level or one tenth of the desired level. Then the device to be tested was substituted for the homogeneous film on the microscope stage, and, if necessary, a known amount of attenuation was removed from the beam.

c. Microstructure Techniques

Silicon is a brittle material at temperatures below about 800°C. The response of the material to an applied stress in this brittle range is elastic strain up to the elastic limit, then the material fractures. In the growth of the crystal and during device processing, the temperature is raised well above 800°C. During such times, the response of the system to applied stress above the elastic limit is a generation and movement of dislocations. The elastic limit occurs at a lower stress as the temperature rises.

The assessment of damage in bulk silicon devices that have undergone second breakdown is difficult because the damage is frequently concealed in the interior of the device, although evidence of damage is clear from the electrical behavior of the device. Since second breakdown damage is due to the formation of melt channels, we have sought to detect the presence of such melt channels by looking for the dislocation patterns that they have produced. These dislocation patterns should be localized to the regions surrounding each melt that have been at a temperature above about 800°C. Studies of filamentation in silicon-on-sapphire diodes

show that short duration, high amplitude pulses produce many current channels, each of which has a narrow region at the requisite temperature for generation of dislocations. (For pulses of 5-μsec duration and of amplitude just short of the second breakdown threshold, the diameter of the high temperature region is about 5 μm. For pulses of 100-μsec duration and of amplitude just short of the second breakdown threshold, the diameter of the high temperature region is about 25 μm. In each case the melt channel, for pulses near threshold, is about 1 μm in diameter. The width of this melt channel increases if the pulse is maintained for an appreciable time after the melt transition.)

Three techniques have been pursued: optical microscopy of polished and etched devices, electron microscopy of replicas of surfaces of polished and etched devices, and x-ray topography. Each of these assumes that the dislocation density will be changed enough by the melt channel to be distinguishable from the background density of dislocations. The first two techniques assume, in addition, that the dislocations intersect the surface of the device that has been exposed during the polishing procedure. The x-ray topographic method yields a photograph of the projection of the interior of the device. The device is first oriented so that a particular Bragg reflection strikes the film plane of the camera. A well-collimated monochromatic x-ray beam floods the device, and the intensity distribution of the chosen diffracted beam is sensitive to the slight changes in crystal orientation associated with dislocations. The pattern is effectively a shadow graph of the dislocations within the device. More details on each of the methods are given in Section 10.

The principal reason for wanting to determine the geometry of damage was to find how the damage geometry of a transistor depends upon the emitter-base bias when a large pulse is applied between collector and base. It is known that the current distribution in a device changes as the operating conditions change. It was hoped that knowledge of the damage geometry for different biases would provide a guide on how to design transistors to improve their resistance to second breakdown.

3. Synergistic Experiments

a. Experimental Procedure

The combined effects of ionizing radiation and electrical excitation in silicon-on-sapphire diodes were examined by energizing the devices with the constant current pulse system used for stroboscopic studies and irradiating with high intensity ionizing radiation from a Neodymium-glass laser during current excitation. A block diagram of the apparatus is shown in Figure 10. The components on the left hand side of the block diagram are those used in previous stroboscopic work. On the right are the laser control and timing components.

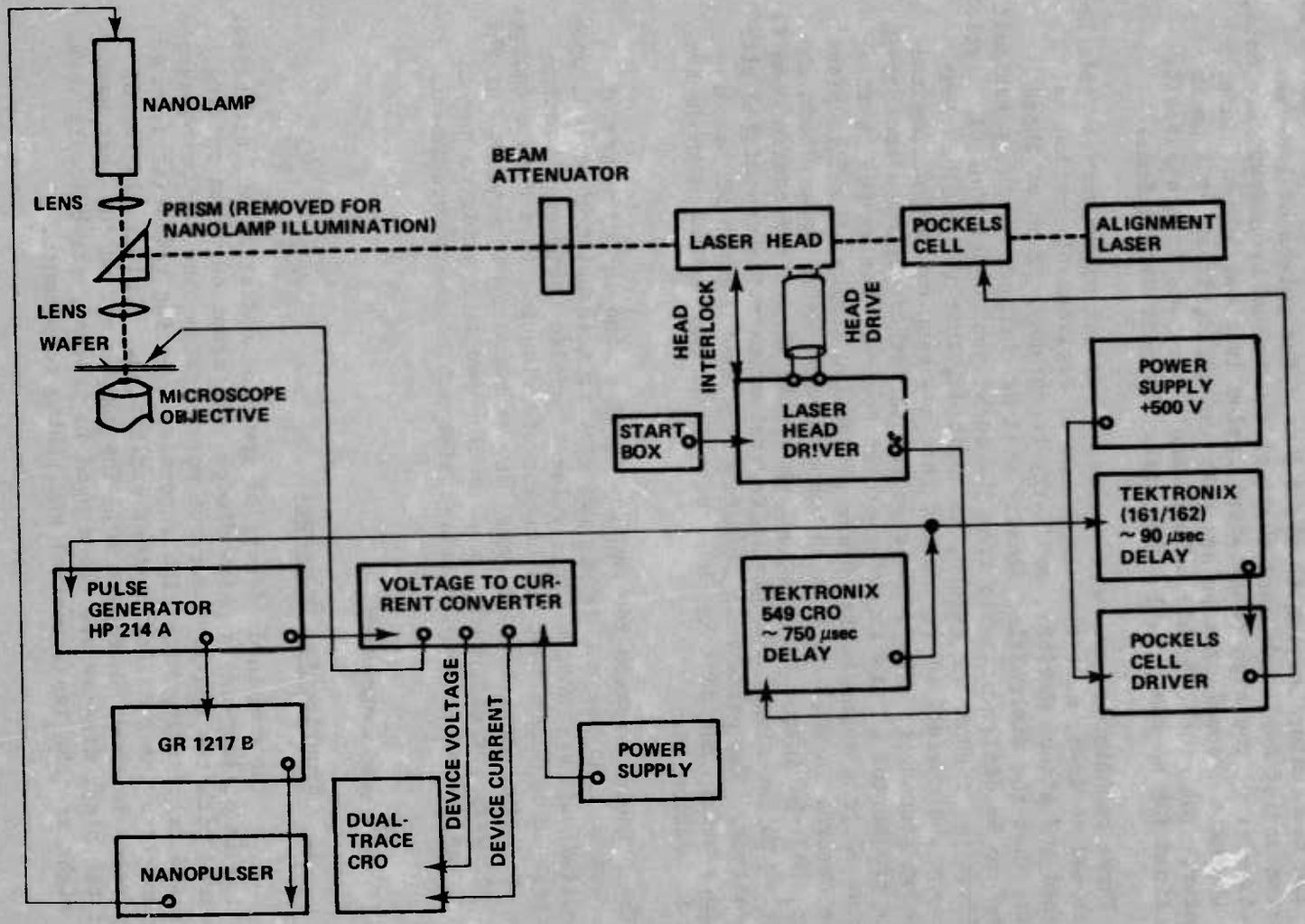

Figure 10. Experimental arrangement for simultaneous electrical and laser light pulsing of silicon-on-sapphire diode.

It requires approximately 30 seconds to build up the voltage to the necessary level (about 2300 V) for firing the flash lamps in the laser head and another 850 μsec for the lamp intensity to reach optimum brightness for firing the laser. Delay circuits are used to synchronize the current excitation with the laser output. The system idles as the laser head driver builds up to the firing voltage. When the lamps are fired, a synchronizing pulse is generated and delivered to the Tektronix 549, which serves as a delay of about 750 μsec. The output trigger from this delay occurs about 90 μsec before the laser output is to occur. In the final 90 μsec, the HP 214A pulse generator is triggered, starting the current pulse excitation of the test diode. The pulse generator is operated in the delayed pulse mode so that the excitation will start at a preset time before the laser pulse occurs. Finally, upon completion of the 90-μsec delay a command signal is delivered to the Pockels cell driver, which Q-switches the laser, firing a 20-nsec pulse of ionizing radiation at the test device.

The system is set up by first aligning the laser system and adjusting the focus and beam attenuation to provide the desired irradiation level on the microscope stage where the test diode is to be mounted. The test device is then put in position and the current pulse excitation level is adjusted. During this phase of the procedure the laser is turned off and the HP 214A pulse generator is operated in the free-running mode. Stroboscopic illumination is used. The 90-μsec delay in the Tektronix 161/162 was adjusted to coincide with the fixed delay between trigger input to the HP 214A and the Nanolamp output, so that in setting up the system the Nanolamp pulse will occur at the same time relative to the current excitation pulse that the main laser will fire when it is energized. This provides for fine adjustment of the synchronism between the excitation and laser pulses, using the pulse delay control on the HP 214A.

When the desired current level and delay time adjustments have been made in the excitation pulse, a prism is placed as shown in Figure 10 and the main laser axis is aligned for irradiation of the test diode using the alignment laser. The HP 214A is then switched to the externally pulsed mode, and the firing sequence is initiated by energizing the laser head driver. The diode is thus energized by a single, preset constant current pulse, during which a prescribed level of ionizing radiation occurs at a set time after the beginning of the current pulse.

Because there are statistical fluctuations in the laser output and in the second breakdown delay time, even in the absence of radiation, a sequence of many simultaneous current and radiation pulses was applied. On alternate pulses the laser beam was blocked from the diode to show the effects of the current pulse alone. The photocurrents due to laser irradiation were of such high amplitude that it might be suspected that part of the effect was due to stray electrical pickup. To ensure that this was not the case the laser was fired with every current pulse, but

the test diode was shielded from the beam by a solid object on every other shot of the laser. No stray signals were observed in the test device current and voltage waveforms when the diode was shielded from the laser beam.

b. Results

In preliminary tests it was found that delay times measured on different diodes of a given geometry and base resistivity differed by about the same amount as when repeated excursions into second breakdown were made on a single diode. Since the latter procedure was far more convenient experimentally, and only a limited number of diodes were available, extensive data were obtained on a relatively small number of diodes. In all, about 20 diodes were studied. The results that follow are typical for each resistivity range.

A sequence of 20 measurements of second breakdown delay time was made on a diode having 0.88 ohm-cm n-region resistivity. A current of 65 mA, reverse bias, produced a second breakdown transition near the middle of a 100-μsec pulse. No adjustments of the system were made during the series of measurements, except that the laser beam was blocked in the odd-numbered shots, and the beam was allowed to irradiate the test diode in the even-numbered shots. Sample data without and with radiation during the current pulse are shown in Figures 11a and 11b, respectively. The pulses are negative, so the baselines in the oscillograms are at the tops of the waveforms.

Typical second breakdown behavior is illustrated in Figure 11a. The voltage-to-current converter (Figure 10) maintains the current nearly constant during pulse excitation of the test diode. This circuit cannot, however, maintain a constant current pulse when there are extremely large, rapid changes in the diode resistance. Such changes may result in current spikes or ringing in the current waveform as the system adjusts to a new condition. Some sacrifice in the speed on the voltage-to-current circuit was necessary to provide sufficient power to break down the test devices.

In Figure 11a, the voltage rises to approximately 125 V with the leading edge of the current pulse, and the diode conducts in the avalanche mode. The voltage rises gradually as the n-region heats up to maximum resistivity, and then it decreases at temperatures beyond the peak of the resistivity-temperature curve. In this example the peak voltage occurs when the temperature of the n-region is about 250°C, and the voltage decrease is very slight before second breakdown takes place. At 44 μsec after the beginning of excitation, second breakdown occurs, as indicated by the abrupt drop in voltage from 115 to 25 V. The oscillations in both the current and voltage waveforms after the transition are due to stray circuit reactance. The voltage remains nearly constant at 25 V until the excitation is removed at the end of

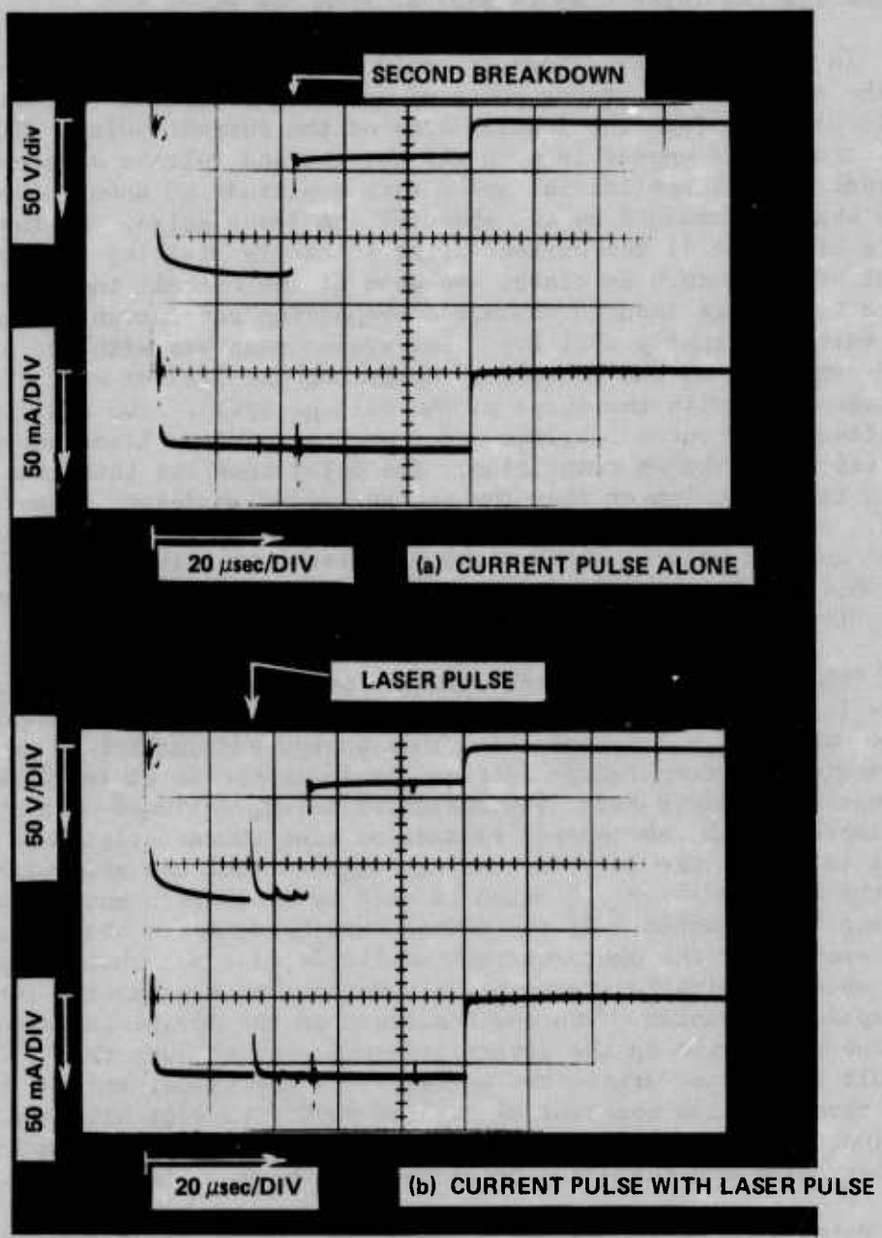

Figure 11. Change in second breakdown delay time due to ionizing radiation in a 0.88 ohm-cm diode with 100-μsec current pulses.

the 100 μsec pulse. (The marker at 32 μsec is a reference, generated externally to indicate the point at which the laser is fired. In Figure 11a the laser beam is blocked from the diode.)

In Figure 11b the diode is again energized with a 65 mA pulse as in the above, and a strong pulse of ionizing radiation strikes the device 32 μsec from the leading edge of the current pulse. High amplitude transients appear in both the current and voltage waveforms. The current has a large initial spike with amplitude of about 350 mA and a wave shape determined by the shape of the laser pulse. On the time scale of Figure 11 the current spike is barely visible; only the undershoot of the return is clear. Because of the circuit inductance (~ 1 μH) there is a large induced voltage accompanying the current spike, driving the voltage slightly positive. The system recovers with its normal time constant, as can be seen by comparing the leading edge of the voltage pulse with the shape of the voltage spike. Two additional low amplitude photocurrent pulses occur due to spurious laser output before the second breakdown transition. The delay time for this case is 50 μsec, which is 6 μsec longer than the second breakdown delay without irradiation. Delay times for the 20 measurements on an 0.88 ohm-cm diode for 65 mA current pulses, without and with laser irradiation are summarized in Table 1. The average delay time increased by 8 ±1 μsec when ionizing radiation was applied, representing an increase of 14 percent.

The oscillograms show no evidence of heating due to the laser radiation, even though the laser beam energy per pulse incident on the diode was about 0.1 J, and twice this energy was sufficient to vaporize the device. A temperature increase would appear as an increase in the voltage immediately after the radiation pulse, followed by a return to equilibrium with the thermal relaxation time characteristic of the diode, about 10 μsec. The lack of heating suggests that the absorption mechanism for the 1.06-μm laser radiation is only by ionization until the damage threshold is reached. At the damage threshold, a new absorption mechanism must occur, for the photo-current amplitude does not change appreciably even when vaporization takes place. We have no explanation for this new absorption mechanism. The photo-current in the device can account for a temperature rise in the irradiated region of no more than 2°C. The circuit inductance drives the voltage to a low value, and the relatively long recovery time constant allows the device to cool slightly. The hot junction region, in particular, is thermally quenched during the recovery time and the onset of second breakdown is delayed.

Using a diode similar to the one discussed above a test was made with the pulse length shortened to 18 μsec, and the current amplitude increased to 70 mA, bringing about a second breakdown transition at about 5 μsec after the beginning of the pulse. Sample data are shown in Figures 12a and 12b, without and with the laser radiation, respectively. The average increase in delay time due to the laser radiation was 1.1 ±0.2 μsec, an 18 percent increase (Table 1).

TABLE 1. SUMMARY OF SECOND BREAKDOWN DELAY TIME MEASUREMENTS MADE ON DEVICES OF VARIOUS DOPING LEVELS, WITH AND WITHOUT LASER IRRADIATION.

n-Region Resistivity	Current Pulse		Delay Time (μsec)	
			Without Radiation	With Radiation
0.88 Ω cm	65 mA 100 μsec	Average Maximum Minimum	(44.2 ± 0.3) 48 43	(51.7 ± 0.7) 56 49
0.88 Ω cm	70mA 18 μsec	Average Maximum Minimum	(5.0 ± 0.1) 5.2 4.7	(6.1 ± 0.1) 6.2 6.0
0.46 Ω cm	110 mA 25 μsec	Average Maximum Minimum	(15.5 ± 0.2) 16.3 15.0	(19.5 ± 0.2) 19.9 19.0
0.064 Ω cm	450 mA 25 μsec	Average Maximum Minimum	(17.2 ± 0.2) 17.8 17.0	(17.2 ± 0.2) 17.9 16.8

NOTE: Standard deviations are indicated by ± in the average values.

Figures 13a and 13b show results for a diode having a 0.46 ohm-cm n-region, using current pulses of 110 mA amplitude and 25-μsec duration. The avalanche threshold for diodes having low resistivity n-regions is smaller than that found for high resistivity devices. At a given reverse-bias current level, less junction heating occurs in the low resistivity devices. The current required to cause second breakdown in a low resistivity diode is therefore greater than in the case of a high resistivity device. Figure 13a shows the increasing voltage as the n-region heats up, followed by the abrupt transition into second breakdown. There is no ringing in this case after the breakdown because the output of the drive circuit is better matched to this low resistance load than to the one discussed previously. A double laser pulse occurred in the result shown in Figure 13b. The voltage was driven nearly to zero on the first pulse. The average increase in the reverse-bias second breakdown delay time due to the effects of irradiation was 4.0 ±0.4 μsec in a series of six measurements (Table 1).

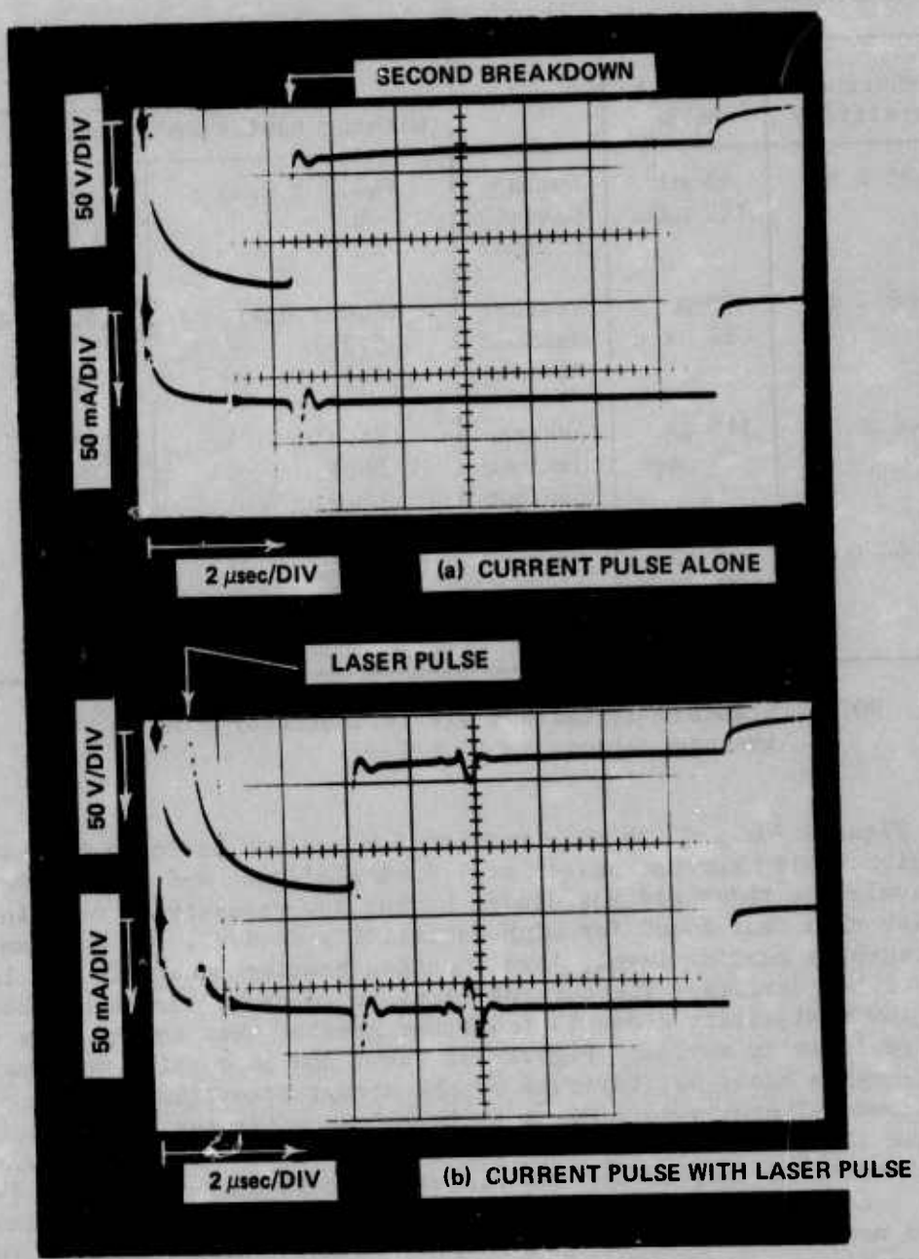

Figure 12. Change in second breakdown delay time due to ionizing radiation in a 0.88 ohm-cm diode energized with an 18 μsec constant current pulse.

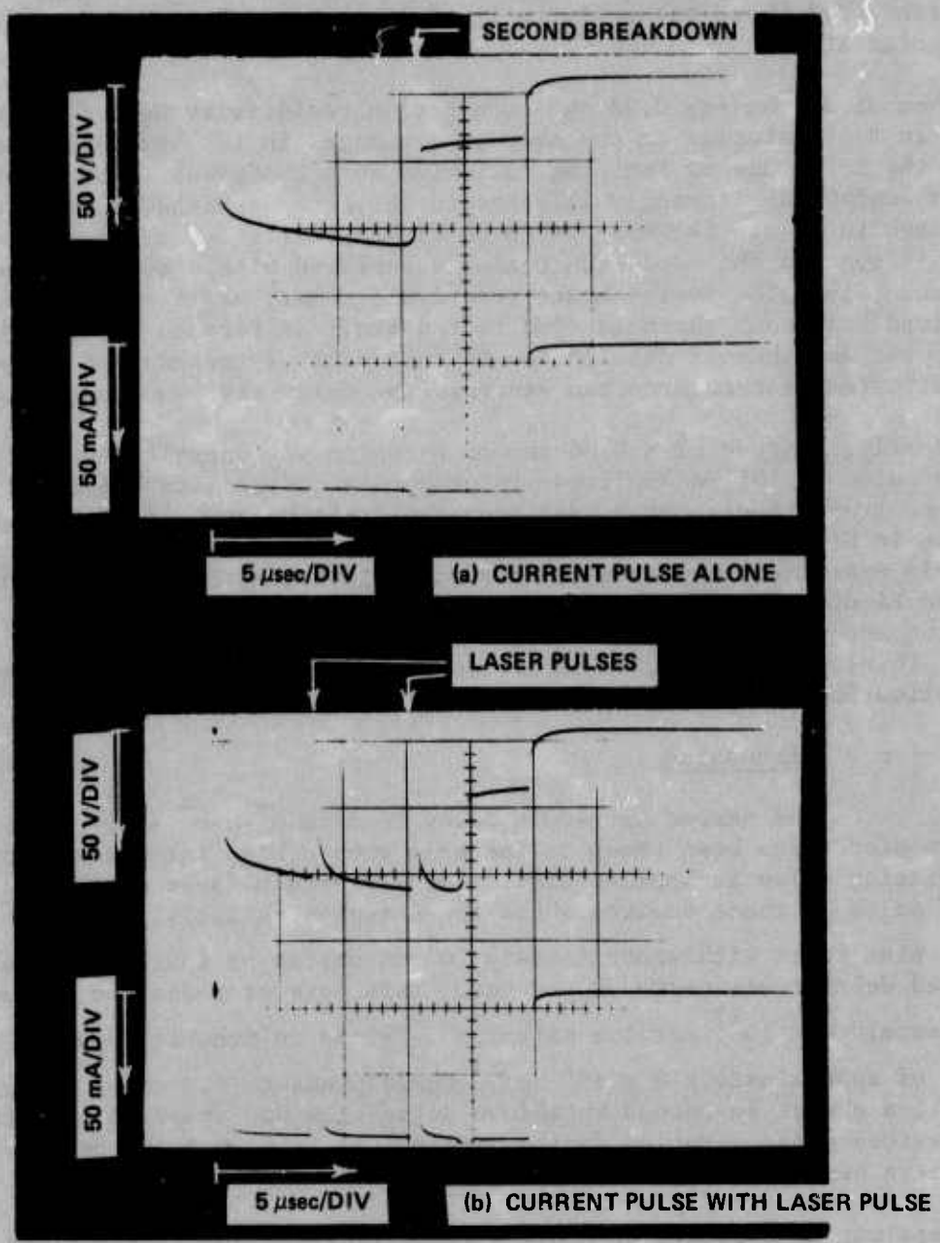

Figure 13. Effect of ionizing radiation on second breakdown delay time in a 0.46 ohm-cm diode energized with a 25-μsec constant current pulse.

In tests on other diodes, having resistivities of 0.147 and 0.064 ohm-cm, statistical fluctuations in the delay times were greater than any changes that could be attributed to the presence of laser radiation. Table 1 shows the results of eight measurements made on a diode with 0.064 ohm-cm n-region. The effects of ionizing radiation are thus most pronounced where the resistivity of the most lightly doped region is the highest.

When diodes having 0.88 ohm-cm n-region resistivity were forward biased in tests similar to the above, no changes in the breakdown times due to the influence of ionizing radiation were observed. Since devices of this doping were strongly affected in the reverse-biased condition, the change in delay time appears to be linked to the interaction between the radiation and the depletion region associated with a reverse biased junction. Since the device heats relatively slowly as it approaches the second breakdown threhold (due to the small difference between the input power and thermal dissipation in that part of the heating curve) a moderate temperature drop can decrease the delay time substantially.

Finally, a diode with 0.46 ohm-cm n-region was energized with a 25-μsec pulse of 105-mA amplitude to produce a reverse-bias second breakdown transition about 3 μsec from the trailing edge of the pulse as shown in Figure 14a. Without adjusting the drive level the diode was again energized, and then irradiated as indicated by the photocurrent spike in Figure 14b. The increase in delay time was sufficient to force the second breakdown transition beyond the end of the current pulse. Thus, in this special case, second breakdown was prevented by the application of a pulse of ionizing radiation.

c. Discussion

The second breakdown delay time in p^+-n-n^+ silicon-on-sapphire diodes has been shown to increase when a high intensity ionizing radiation pulse is applied simultaneously with a large amplitude current pulse in those devices where the n-region resistivity is high. Reverse bias tests with approximately 10^4 rd pulses of ionizing radiation increased delay times up to 20 percent. This dose of radiation generates approximately 4×10^{17} carrier pairs/cm^3. Since an impurity doping density of approximately 4×10^{17} cm^{-3} corresponds to 0.2 ohm-cm n-type material, a change in second breakdown delay time was observed only in those devices whose n-region doping density was less than the density of carriers generated by the ionizing pulse.

There was no evidence of heating in test diodes due to the laser radiation up to the threshold of vaporization of the specimen by the laser output, regardless of when the laser pulse occurred relative to the excitation pulse. The photocurrent spike had an amplitude of about 350 mA during test conditions. No great increase occurred in the amplitude of the spike as the laser intensity was increased to the damage threshold. Damage due to laser radiation is therefore not directly associated with the generation of electron-hole pairs.

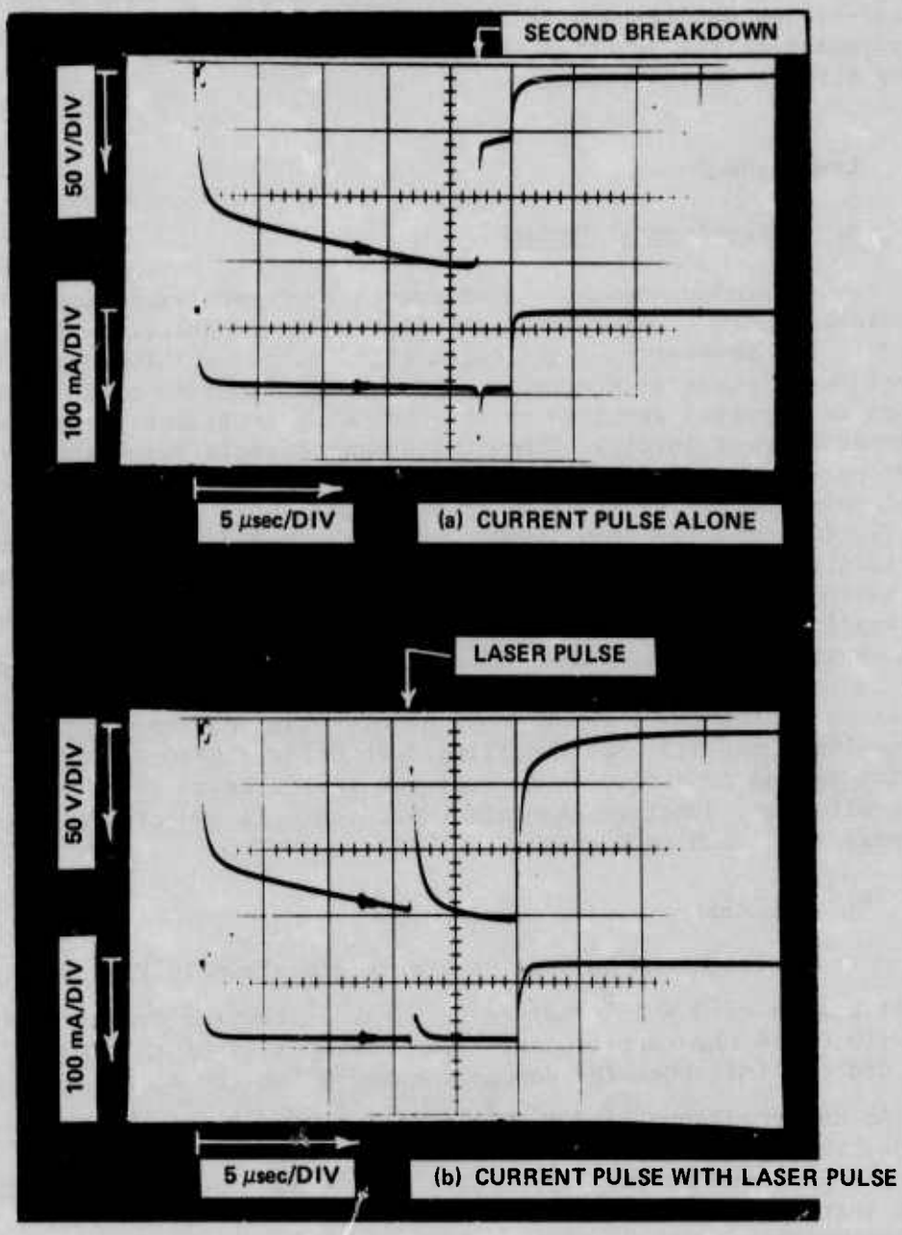

Figure 14. Second breakdown prevented in a 0.88 ohm-cm diode by application of a laser pulse.

Application of ionizing radiation to diodes operating in forward bias produced no effect on the breakdown delay times, even for the highest resistivity devices. This indicates that the effects observed in reverse-biased devices are associated with cooling of the very hot region adjacent to the junction as a result of the voltage drop due to inductive effects in the circuit.

4. Laser Damage

a. Experimental Method

Simultaneous pulses of constant current excitation and laser radiation were applied to diodes in the manner described in Section 3a. The intensity of the laser illumination was increased from the lowest level where a detectable photocurrent occurred to a level sufficient to vaporize portions of the device. Experiments were done at different current levels. Since the damage effects associated with the laser pulses were independent of the current amplitude, data are presented only for pulses of high amplitude and short duration. The high amplitude means that the device was heated rapidly by the current pulse. Additional heating effects by the laser would be in the direction to hasten a second breakdown transition. Thus the arrangement is very sensitive to detecting thermal affects associated with the laser interactions with the test diodes. Pulses of short duration were employed so that the time scale of observation was comparable to the time duration of the laser pulse (~ 20 nsec). Thus current pulses of 700 mA amplitude and 1.2 μsec duration, just below the threshold for destructive second breakdown, were employed in the tests to be described. At this excitation, junction channels (dark spots in the stroboscopic experiments) form with each pulse.

b. Results

Voltage and current waveforms are shown in Figure 15 when laser pulses of 3×10^9 rad/sec to 5×10^{11} rad/sec are applied to a diode with 0.064 ohm-cm n-region. (The resistivity of the diode n-region did not influence the damage threshold for the diodes of this study.) At an irradiance of 3×10^9 rad/sec, the voltage waveform, Figure 15a, shows a barely perceptible drop in voltage due to the photocurrent produced by the laser pulse at t = 360 nsec. (The laser pulse has increased the number of carriers. If there had been an appreciable heating effect, there would be an increase in resistance of the n-region. In studies using longer pulse lengths, such a heating effect could be detected because the thermal time constant of the system is about 10 μsec. No recovery is found with such a time constant, so that we conclude the slight voltage drop is due to the photogenerated carriers only.) Figures 15b, 15c, and 15d show the waveforms when the irradiance is 3×10^{10}, 3×10^{11}, and 4×10^{11} rad/sec,

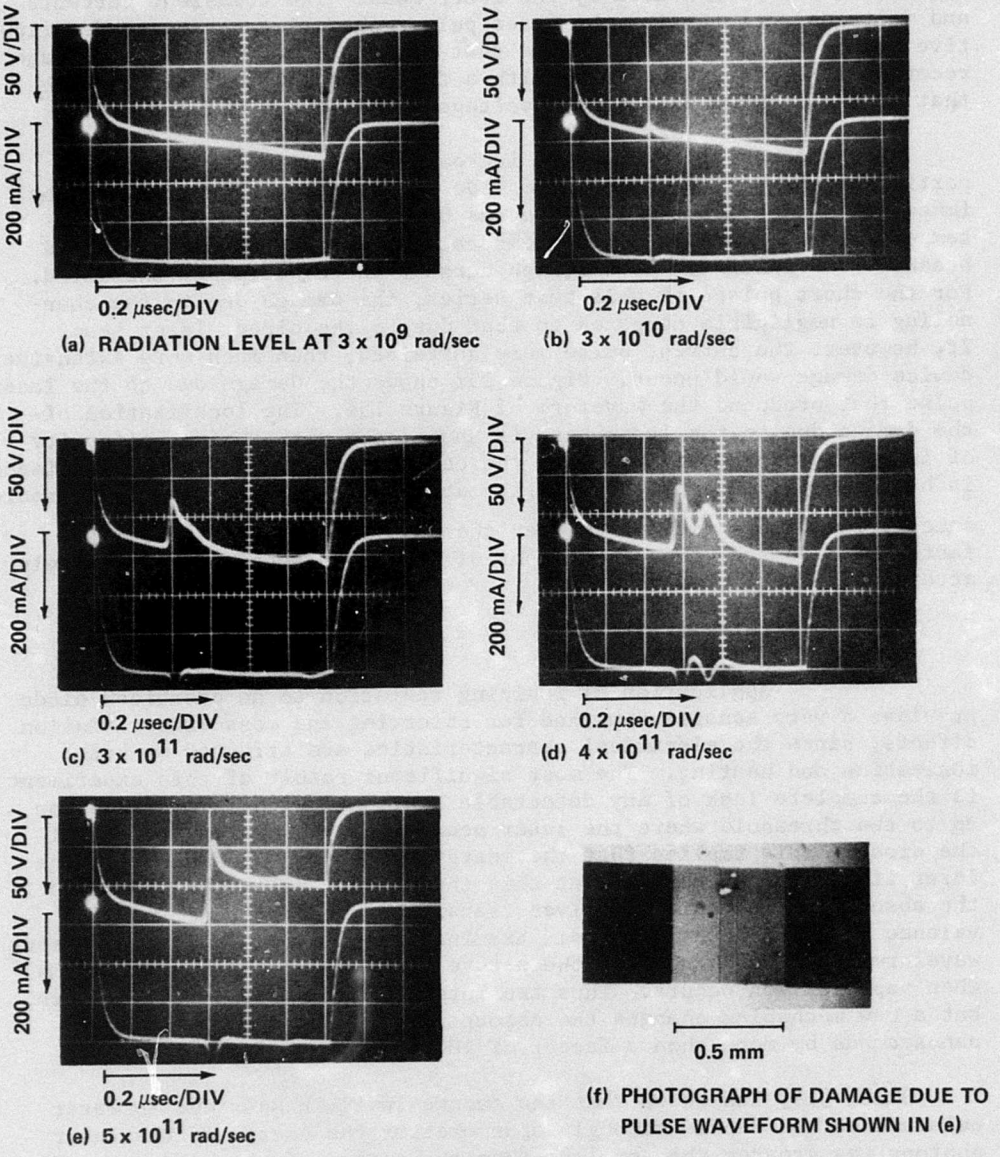

Figure 15. Effect of laser radiation on conduction in a diode operating near the second breakdown threshold.

respectively. The latter is about 80 percent of the irradiance required to vaporize portions of the device by the laser alone. In none of these cases, in spite of the large photocurrents, is there any indication that the device has been heated by the laser beam. The transient currents and voltages accompanying the laser pulses show time constants descriptive of the diode circuit. (Note that after a laser pulse the voltage recovers to its previous value with a time constant that agrees with that of the leading edge of the voltage pulse, about 0.1 μsec.)

When the radiation level is increased to 5×10^{11} rad/sec, a portion of the device about 30 μm wide vaporized. Further, since the immediate region about that which has been vaporized is above the temperature of the peak of the temperature-resistivity curve, second breakdown is initiated so the high current in the diode is channeled. For the short pulses of this test series, the damage due to the channeling is negligible compared to that due to the direct laser beam. If, however, the current pulse were sustained, then much more extensive device damage would occur. Figure 15f shows the damage due to the laser pulse that produced the waveform of Figure 15e. The localization of the damage due to the laser beam is associated with the nonuniformity of intensity of the beam. Since the calibration of the laser irradiance is based on the integrated intensity across the beam, the actual irradiance at the damage site is greater than 5×10^{11} rad/sec by about a factor of 2 (based upon photographs of the cross section of a strongly attenuated beam).

c. Discussion

Application of ionizing radiation to an energized diode provides a very sensitive method for observing and measuring radiation effects, since the electrical characteristics are affected by both ionization and heating. The most significant result of this experiment is the complete lack of any detectable heating due to laser radiation up to the threshold where the laser beam alone vaporizes portions of the diode. This implies that the energy absorption mechanism for the laser light changes abruptly at this threshold. Below the threshold the absorption mechanism involves transitions of electrons from the valence to the conduction band. Examination of the voltage and current waveforms show no changes in the nature of the photocurrent waveforms when vaporization occurs. Thus the interband transition still occurs, but a new mechanism changes the absorption coefficient within a few nanoseconds by more than a factor of 10.

Smith [19] has shown that the damage level in GaAs due to laser pulses does not depend strongly upon whether the energy of the laser photons was greater than or less than the energy of the band gap. His experiments were on wafers about 0.010-inch thick and he had no convenient way of isolating heating effects below the damage threshold. Damage was accompanied by high surface temperatures, vaporization, and microcracking. Fountain et al. [20] catalogued plausible mechanisms

for laser damage with reference to a damage study of $LiNbO_3$ crystals, listing 17 mechanisms: (1) local heating due to absorption, (2) thermal shock, (3) the pyroelectric effect, (4) two-photon or multiphoton absorption, (5) intense optical electric fields, (6) beam trapping, (7) optical rectification, (8) surface dielectric stress, (9) radiation pressure, (10) ionization at a surface, (11) piezoelectricity, (12) the converse piezoelectric effect, (13) electrostriction, (14) avalanche breakdown caused by the acceleration of conduction-band electrons to ionizing energies, (15) phonons driven at the difference frequency between two frequency components of the laser, (16) photons produced by energy transfer through "cold" conduction-band electrons, and (17) stimulated Raman or Brillouin scattering. The thin film experiments seem to rule out the mechanical effects and the discontinuity in the absorption mechanism rules out the simple thermal effects. Beam trapping cannot occur in the thin film geometry. The most plausible processes are those dependent strongly on the intensity of the laser excitation, such as the multiphonon or electron avalanche processes. Some form of collective excitation is also plausible [21]. Agranal et al. [22] observed no nonlinear absorption effects in a damage study of PMMA and polystyrene. They concluded damage was nonthermal in nature, nor could it be associated with electrical breakdown in the electromagnetic field of the laser radiation. Multiphonon processes seemed to be the most plausible explanation for the source of gas that initiated cracks in the media. Yablonovitch [23] and Fraden et al. [24] favor electron avalanche as the mechanism of laser damage in single crystals of alkali halides free of blemishes. Their basic argument is the similarity of the breakdown fields with dc excitation and with laser excitation. No direct evidence is offered for the avalanche mechanism.

At the present time, we conclude the mechanism for laser damage in semiconductors and insulators remains unknown.

5. Filamentation in Homogeneous Films

Current filamentation accompanying high amplitude pulse excitation in thin homogeneous silicon films has been described experimentally for a point-to-point probe geometry and theoretically for a parallel electrode geometry [6,7]. At the time the above experiments were performed, we did not have homogeneous films with a parallel geometry. However, in the wafer supplied by Dumin, there were a number of test strips with a parallel electrode geometry. Current pulses were applied to these with amplitudes below and above the melt channel threshold.

In the theoretical model, the film was divided into strips of equal size, each extending from one electrode to the other. Heat conduction to the substrate and between strips was allowed, but the current was constrained to be perpendicular to the electrodes. The temperature at the sides of the film was assumed constant and equal to the ambient

temperature of the substrate. The temperature dependences of the electrical and thermal conductivities of the silicon were included in the model. For constant current pulses of low amplitude (so that no part of the film reached a temperature above that of the peak T_2 of the temperature-resistivity curve), the current was almost uniformly distributed with the center strip being slightly hotter than the outer strips. However, when the temperature of the center strip exceeded T_2, filamentation began. With increasing current amplitude, the filament rapidly localized about the central strip. The model could not be carried out through the melt transition because of convergence problems in the mathematical solution. In the experimental work with point probes, the melt channels that did form, for pulses having an amplitude just sufficient for melt formation, had a width of a few micrometers.

Attempts were made to show the temporal and spatial development of filamentation in 100 μm square homogeneous films using the stroboscopic apparatus, but the conduction pattern proceeds too rapidly from uniform conduction, through filament development and to melt formation as the applied current level crosses the filamentation threshold. Thus, in practice, the current level could not be controlled with sufficient accuracy to permit stroboscopic observations of filament formation before the occurrence of a melt. The melt channel formed by a single breakdown occurs through the geometric center of the square as predicted by the model [6,7]. Figure 16a shows a single melt channel formed in a 0.78 ohm-cm silicon square.

In films having resistivity of the order of 0.01 ohm-cm or less, however, a different form of damage appears. The damage, shown in Figure 16b, in a 0.003 ohm-cm film takes the form of an isolated melt spot near the geometric center of the square. And in Figure 16c the damage in a 0.013 ohm-cm film consists of a melt spot with faint filament streaks reaching part of the way from the melt spot toward the electrodes.

The formation of a melt spot in the center of a film may be explained in terms of heat flow in the plane of the film, coupled with the resistivity-temperature characteristics of the material. As noted in previous filamentation studies there is a ballasting effect in the direction transverse to the direction of the current as long as the film temperature is below the turnover point, or maximum resistivity point T_2, in the resistivity-temperature curve. But there is no ballasting of thermal gradients in the direction of the current. If a strip across the film parallel to the electrode ends becomes hotter than the rest of the material, its resistivity increases. Since the hot strip must carry the same current as the cooler regions the increased resistivity causes greater Joule heating. Thus a mechanism exists for a buildup of thermal gradients parallel to the direction of the current. Because heat may flow out of the film toward the electrode ends, a high temperature region may develop in the central section of the film as

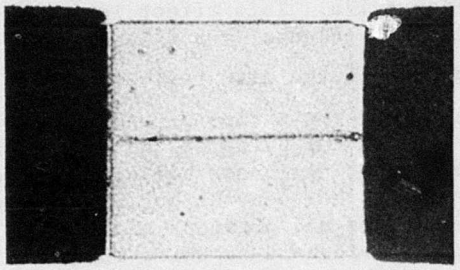

(a) HIGH RESISTIVITY FULL LENGTH MELT CHANNEL

100 μm

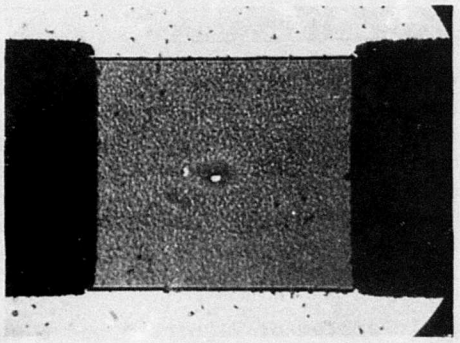

(b) LOW RESISTIVITY, SINGLE MELT SPOT

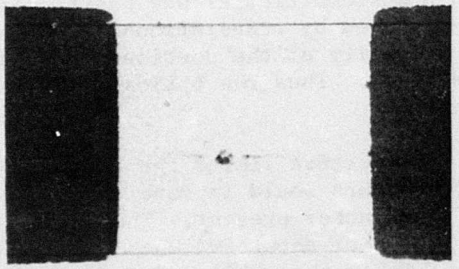

(c) INTERMEDIATE CASE

Figure 16. Damage in homogeneous silicon-on-sapphire films.

illustrated in Figure 17a. This effect is greatest in low resistivity films where T_2 is high (Figure 2) and large temperature gradients may exist before any part of the film reaches the unstable regime above T_2. When the central transverse strips of the film reach the turnover temperature the ballasting in the plane of the film perpendicular to the direction of the current no longer holds, and a localized filamentation occurs--but only in the hot central portion of the film. Judging from the nature of the damage and previous theoretical results on filamentation in homogeneous silicon-on-sapphire films it is expected that the thermal distribution at the threshold of melt spot formation should appear somewhat as illustrated in Figure 17b.

6. Temperature Measurements During Pulse Testing

a. Experimental Procedure

Temperature configurations of silicon-on-sapphire devices energized with dc current have been mapped by the authors [6]. Spatial resolution of about 10 μm was achieved in those measurements, but the study was limited to steady state cases. In order to demonstrate the capability of the stroboscopic technique, this section will describe time-resolved temperature measurements on the same diodes. Temperature configurations of about 1 μsec, the jitter in the triggering circuit for the nanolamp.

The stroboscopic system of Figures 5 and 6 was modified as shown in Figure 18. The test diode was positioned on the microscope stage and imaged on the film plane of the camera.

To obtain the necessary spatial resolution, a screen with a circular aperture approximately 0.5 mm in diameter was placed in the image plane of the camera and a photomultiplier was positioned behind the aperture. Scanning was accomplished by translational movement of the microscope stage, the light intensity of the portion of the specimen imaged at the aperture being measured. Thus the optical path remained constant throughout a scan.

The size of the aperture limits the spatial resolution to about 10 μm. A smaller aperture would improve the spatial resolution were not a second limiting factor present. The transmittance through the diode drops by a factor of about 100 when the temperature rises 700°C. Since temperatures higher than this occur in the dark spots (junction channels), the transmitted light through the dark spots is found to produce a signal comparable to the noise level of the photomultiplier. The 0.5 mm aperture used was found experimentally to be the best compromise between adequate signal level and good spatial resolution.

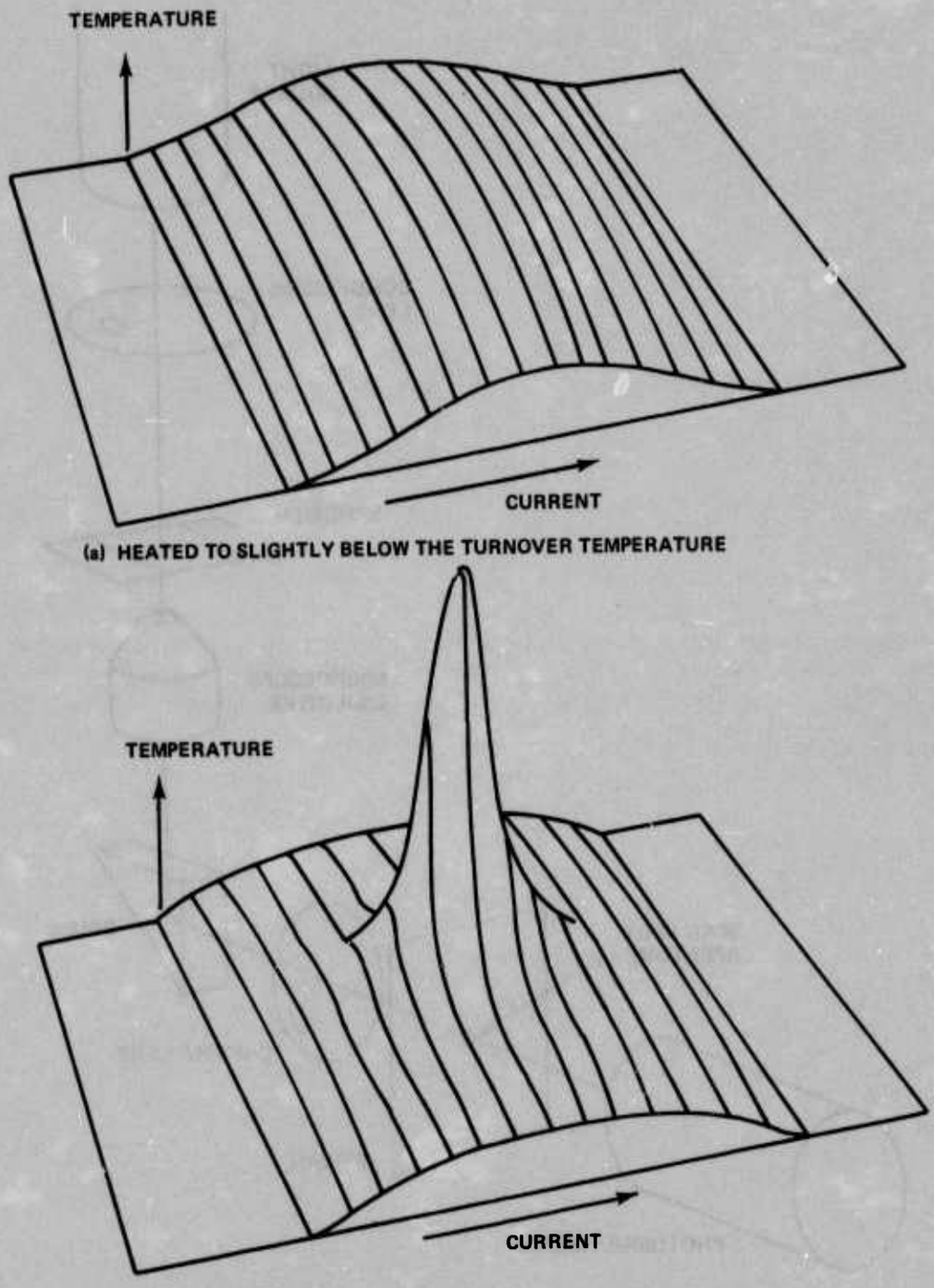

Figure 17. Temperature distribution in a low resistivity film.

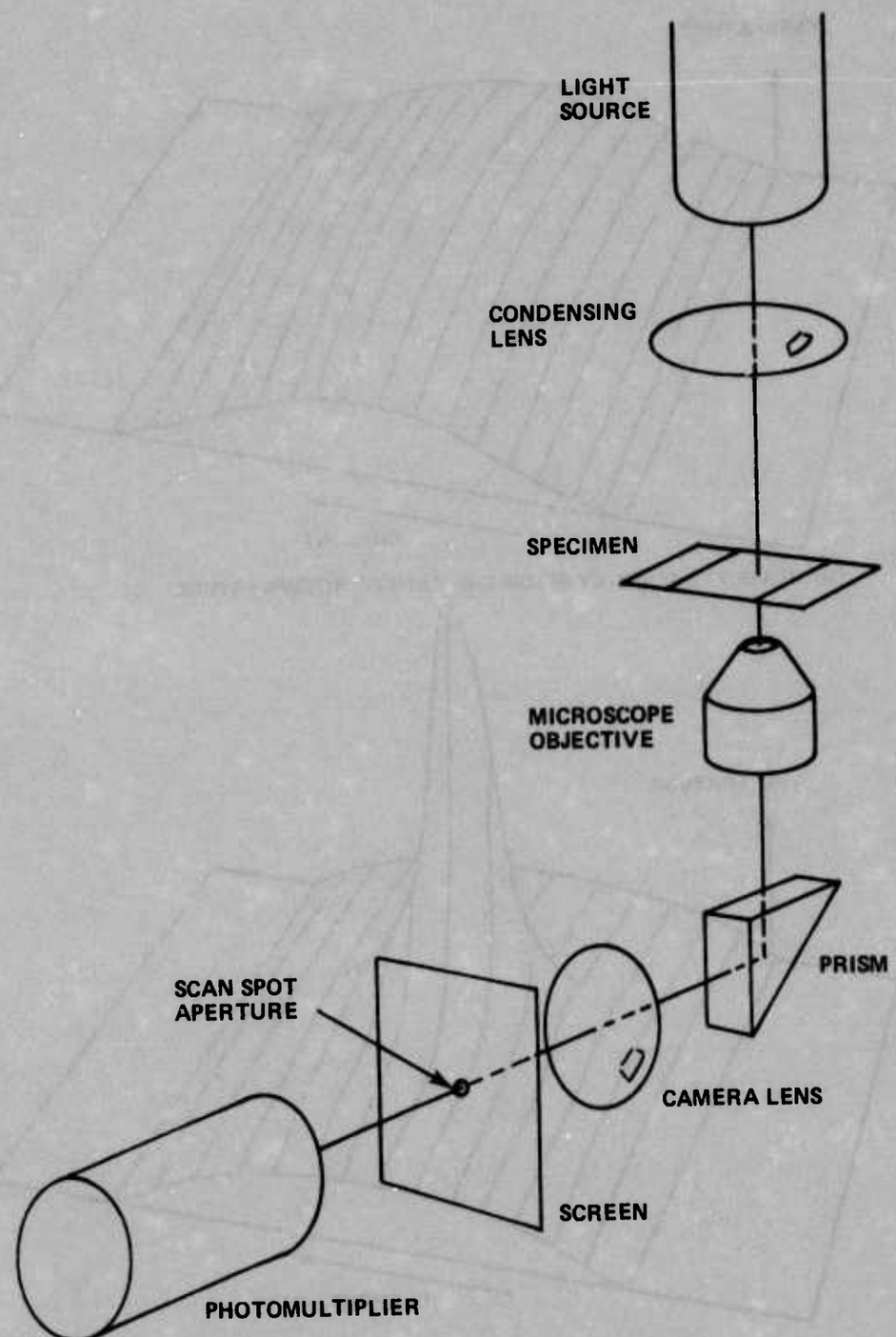

Figure 18. Optical arrangement used for making time-resolved temperature measurements.

The intensity of the stroboscopic source (Nanolamp) varies from pulse to pulse with a range of ±20 percent about its mean value. The intensity distribution measured in a sequence of 5000 pulses is shown in Figure 19. Thus it is necessary to measure the average transmittance over a large number of pulses if a meaningful temperature measurement is to be obtained. The output of the photomultiplier for a given position of the diode, which is proportional to the intensity of the light incident on the diode, was accumulated in a 100-channel pulse height analyzer. In a sequence of 500 pulses, the integrated output was repeatable within ±2 percent.

The measurement procedure was to scan the diode in steps of 0.5 mil, using the multichannel analyzer to accumulate the amplitudes of 500 successive pulses at each diode position.

b. Results

Figure 20a shows a stroboscopic photograph of a diode with three dark spots. The current pulses were 100 μsec long and 420 mA in amplitude; the strobe light was positioned close to the end of each current pulse at t = 97 μsec. Figure 20b is a plot of the temperature profile measured at t = 97 μsec on a line parallel to the junction and 0.5 mil away from the junction. The temperature scale of Figure 20b was determined from the curves of optical transmission versus temperature shown in Figure 7.

The temperature profile contains three strong peaks at the junction channels indicated by the dark spots. Two additional regions on either side are approaching the temperature for junction channeling. The rapid drop in temperature at the edges of the diode attests to the importance of including lateral heat flow in any model attempting to describe the current and temperature configuration. (Lateral heat flow was included in the model referred to in Section 5.a.) The peak temperature of 500°C is lower than the true peak temperature because of the spatial averaging and the temperature gradient from peak to adjacent valley (about 150°C/mil) is less than the true temperature gradient for the same reason. The stability of the pattern in the presence of these high lateral temperature gradients implies that the principal heat flow path is into the substrate. (This has previously been demonstrated using the stroboscopic technique to observe the decay of the dark spots upon termination of each current pulse; no lateral diffusion is observed during the 10-μsec decay time.)

The hot regions of the diode become self-luminous as they become hotter and the light signal reaching the photomultiplier is the sum of the strobe light transmitted through the specimen and the emitted light at the same portion of the specimen. The duration of a strobe flash is 20 nsec while the hot spots emit for many microseconds in each pulse. In photographs, the integrated emission is recorded. However, in the photomultiplier-multichannel analyzer system, for pulses above the

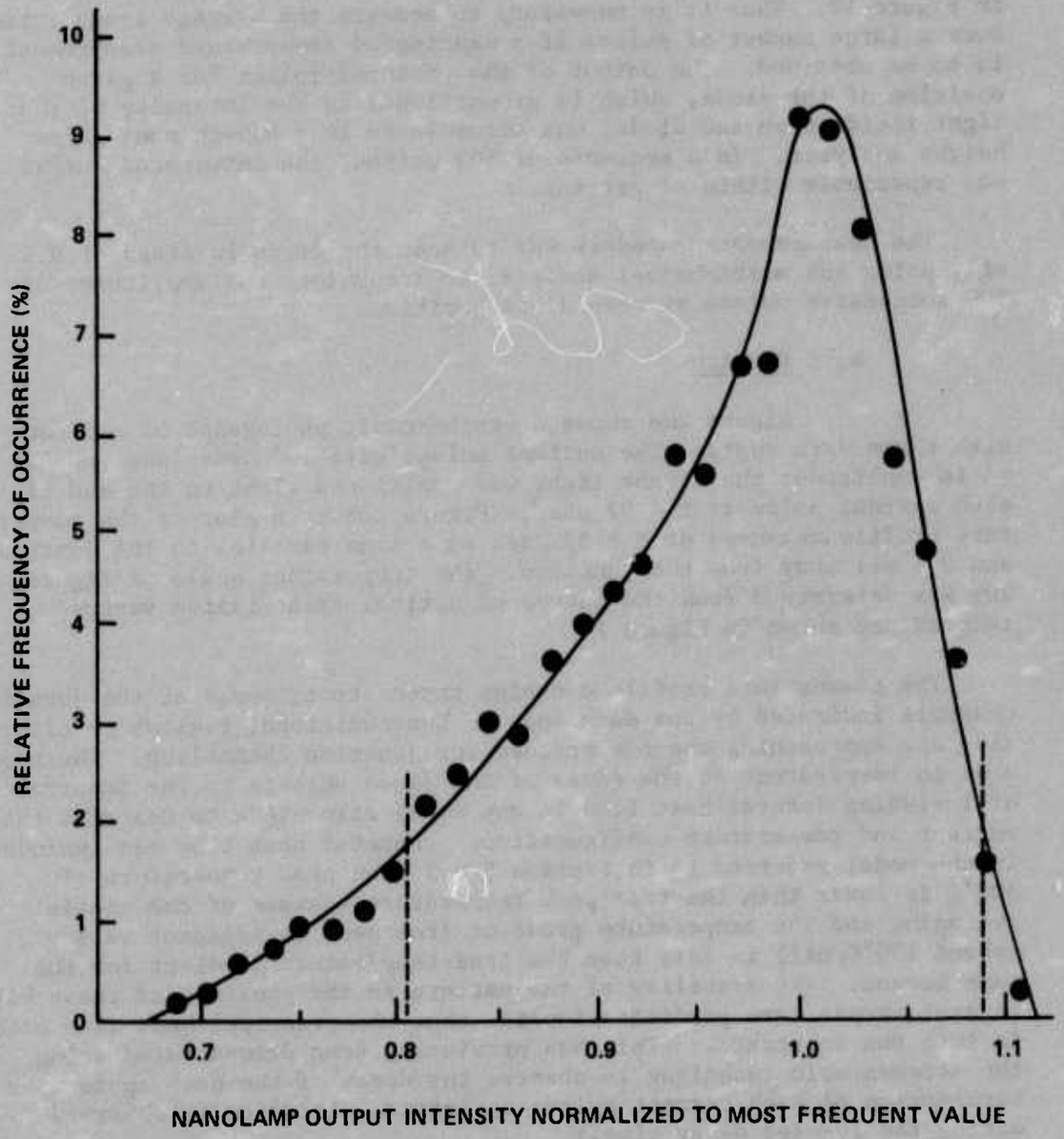

Figure 19. Output intensity distribution for 5000 Nanclamp pulses.

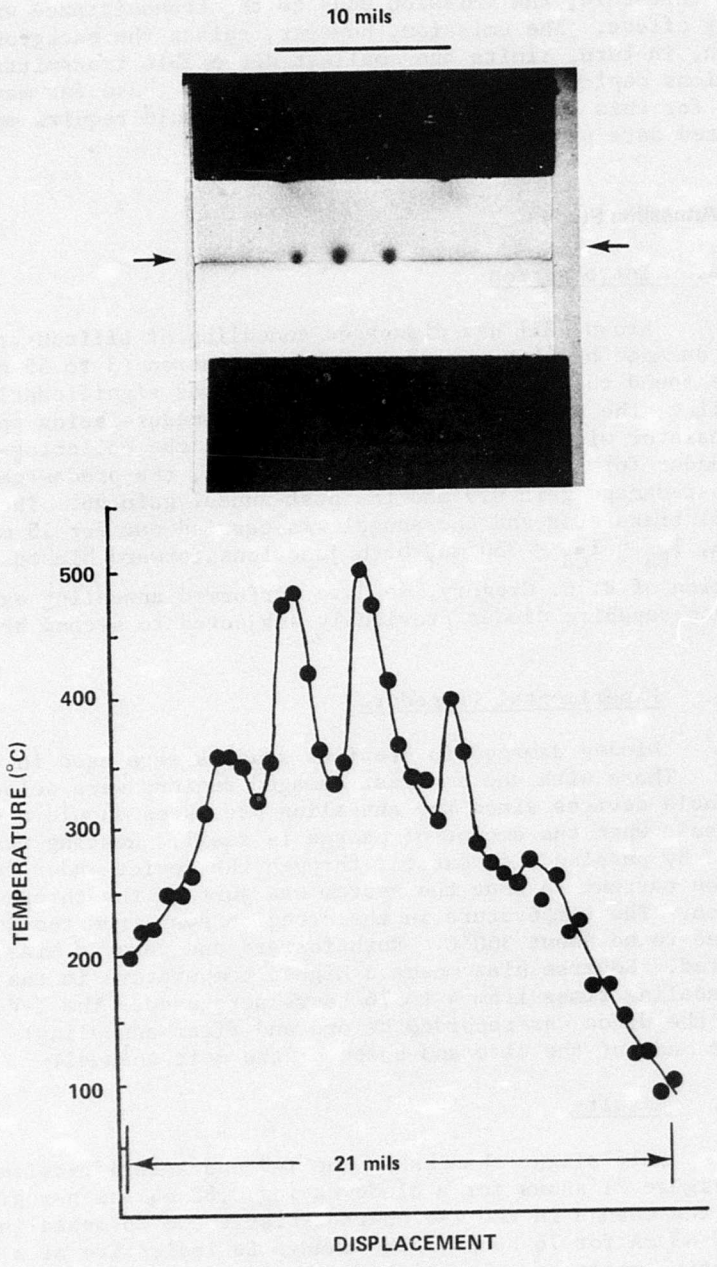

Figure 20. Time-resolved temperature measurement of the cross section of a diode exhibiting three junction channels.

triggering threshold, the emission adds to the transmittance without an integrating effect. The emission, however, raises the background noise level which, in turn, limits the smallest detectable transmittance. The conditions depicted in Figure 20 are close to those for maximum resolution for this system. Better resolution would require much more sophisticated data processing methods.

7. Annealing Study

a. Introduction

Brown [25] has discussed annealing of silicon transistors which were damaged by high amplitude, short duration (3 to 55 nsec) pulses. He found that the gain of his devices was significantly improved upon annealing, the most effective annealing procedure being operation of the transistor with both the emitter-base and the collector-base junctions under forward bias. In a typical case, the predamage gain was 132, the post-damage gain 0.9 and the post-anneal gain 96. The device was a 2N4251 transistor and the anneal was carried out for 15 min with I_B = 700 mA, $I_{EB} = I_{CB}$ = 350 mA, both junctions forward biased. At the suggestion of B. L. Gregory, we have performed annealing experiments on silicon-on-sapphire diodes previously subjected to second breakdown damage.

b. Experimental Procedure

Diodes damaged in previous studies were used in these experiments. Those with the smallest damaged regions were selected from among available devices since the annealing processes should give the greatest result when the amount of damage is small. Heating was accomplished by passing a dc current through the device under test, adjusting the current so that the system was just on the threshold of filamentation. The temperature in the n-region away from the junction was estimated to be about 300°C. Both forward and reverse bias tests were conducted. Reverse bias means a higher temperature in the junction region. Annealing times from 4 to 76 hours were used. The I-V characteristic of the diode was recorded before and after annealing. Comparison was also made of the size and shape of the melt channel.

c. Results

Only slight changes in the I-V characteristics were observed. Figure 21 shows for a diode having 0.88 ohm-cm n-region resistivity the change in the I-V characteristic due to annealing with a current of 43 mA for 76 hours. The change is indicative of a decrease in the effective resistance parallel to the junction, possibly due to a slight change in the doping profile.

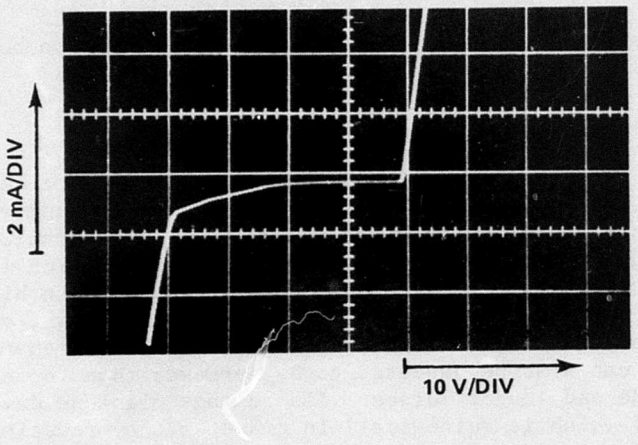

(a)

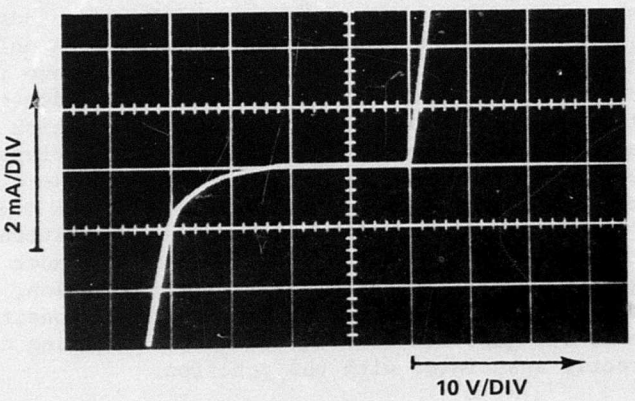

(b)

Figure 21. Change in the current-voltage characteristic of a diode subjected to 76 hours of annealing.

The original melt channels in the devices employed in the annealing study were 1 to 3 μm in diameter, a single melt in each device. Microscopic examination failed to show any detectable changes in the melt channels as a result of the annealing process.

The degradation accompanying annealing was slight in both forward and reverse bias, the latter having the smaller effect.

d. Discussion

The results of Brown and the above results seem to be contradictory. However, it is necessary to interpret them with caution. The silicon-on-sapphire study seems to show that recrystallization of the solidified melt does not occur. The review in Section 1 pointed out that junction filaments were more closely spaced with high amplitude pulses. With the short duration pulses employed by Brown, very high amplitudes are required for second breakdown. The melt channels accompanying these can also be expected to be narrower than those due to lower amplitude and longer pulses. Also damage might be due to multiple melts, each of which is quite small in diameter. By reducing the diameter of the melt, its resistance is correspondingly increased, so the shorting effect of the melt is not so severe. The narrow melt is accompanied by local heating in a region surrounding the melt (that corresponding to the dark spots in the stroboscopic study). The size of this hot region decreases as the pulse amplitude increases. Accompanying the formation of a melt is a region of high stress because silicon expands about 10 percent upon melting. Dislocations can occur in silicon only above about 800°C; at lower temperature stress, relief must come from elastic strain or fracture. Thus, one might anticipate a high density of localized dislocations in the small region about each melt which is above 800°C. Such a region should reduce the lifetime of carriers. The annealing process of Brown might be the movement of these dislocations so that they can annihilate each other and thus increase the lifetime. Some support to this idea is obtained by Brown's observation that annealing is most effective under forward bias conditions. Under such conditions, heating is primarily in the high resistivity region, the same region where the melt is located. Under reverse bias conditions, the hottest region is the junction itself. Thus the annealing does not seem to be directly associated with the junction.

8. Double Step Pulse Testing

a. Experimental Procedure

The stroboscopic apparatus used in previous experimental work was modified slightly to provide for two pulse inputs to the drive circuit (voltage to current convertor), as shown in Figure 22. Separate pulse generators, coupled by a variable time delay, provide a negative primary pulse and a positive secondary pulse to the emitter and base,

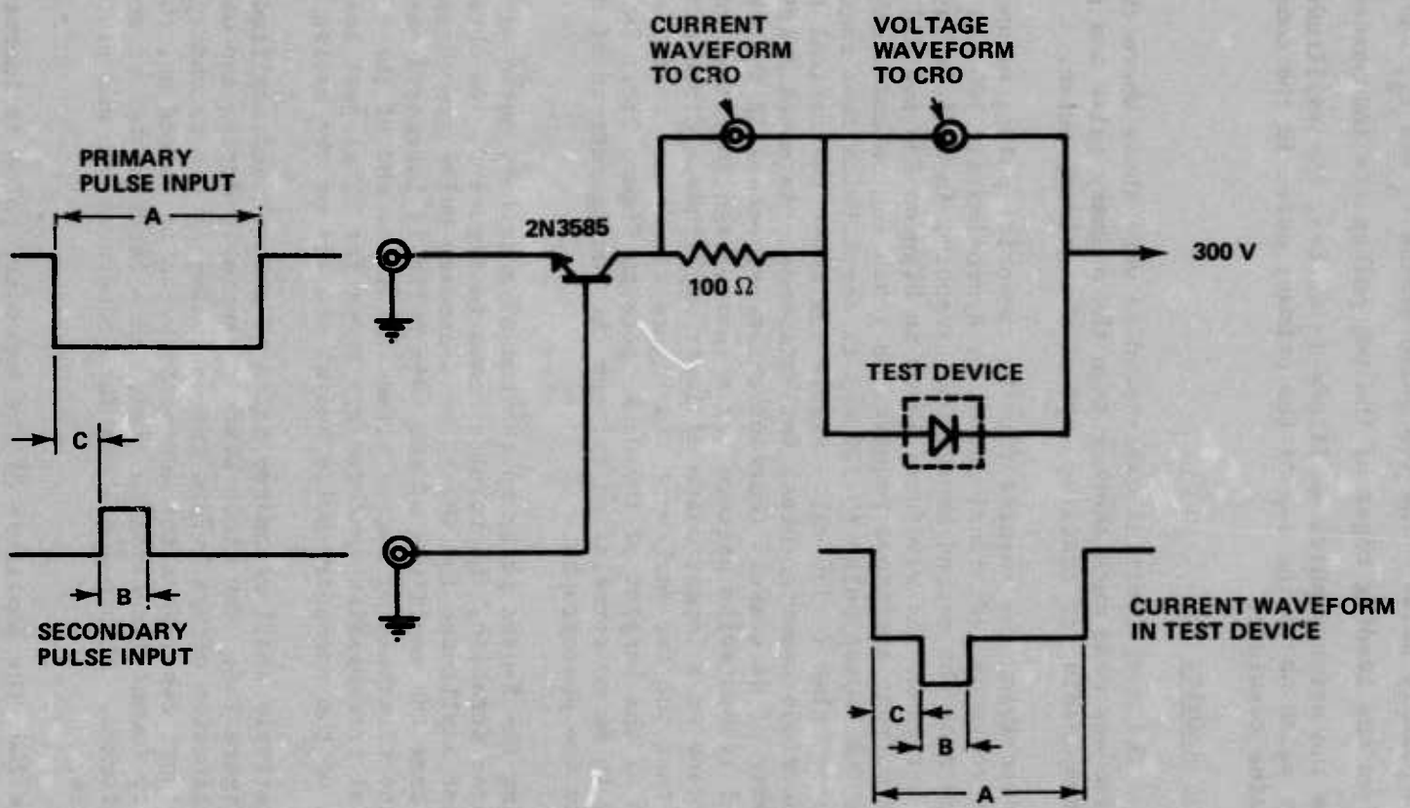

Figure 22. Constant current drive circuit modified for double step pulse testing.

respectively, of the drive transistor. The current through the test device has a composite waveform consisting of the secondary pulse riding on the primary pulse. The two pulse widths t_A and t_B, and the time t_C between the leading edges of the two pulses are independently variable. As the primary pulse amplitude is varied, the amplitude of the secondary pulse above the top of the primary pulse in the composite waveform remains constant.

b. Results

The most fruitful cases studied were those where the secondary pulse was made much shorter than the primary pulse and placed near either the leading or trailing edge of the primary pulse.

Before describing the results for the composite pulse, we shall examine the effects of individual pulses of approximately 100 and 5-μsec duration, each near the second breakdown threshold, in a diode having 0.147 ohm-cm n-region. The waveforms shown in Figures 23a and 23d indicate that the current amplitude required to reach the second breakdown threshold for the 5-μsec pulse (~ 320 mA) is about twice that required for the 100-μsec pulse (~ 150 mA). Figure 23b shows the optical transmission of the diode under no bias, for reference. As noted previously, a greater number of dark spots (current channels) occurs in the stroboscopic optical transmission pattern for a short, high amplitude pulse than for the case of a longer pulse of lower amplitude. Close examination reveals that the two dark spots in Figure 23c do not coincide with the positions of the largest of the dark spots in Figure 23e. In fact, there appears to be no correlation between the configurations of dark spots in these two photographs.

By placing the 5-μsec pulse on the end of a primary pulse of approximately 100-μsec duration, the results shown in Figure 24 are obtained. Three different amplitudes for the short secondary pulse are chosen, and for each case the amplitude of the main pulse is increased until the diode is at the threshold of second breakdown at the end of the composite pulse. Optical transmission patterns are shown for times just before the beginning of the secondary pulse and at the end of the entire pulse.

A comparatively small secondary pulse of about 25-mA amplitude is employed in Figure 24a. The diode heats appreciably during the main pulse, and nucleation occurs before the beginning of the secondary pulse, as shown in Figure 24b. When the secondary pulse is turned on, the channel already formed increases in size, and a large number of smaller channels are formed. Figure 24c shows the pattern at the end of the composite pulse.

In Figure 24d, the amplitude of the secondary pulse is increased to about 50 mA. A smaller main pulse is required to bring the diode to the second breakdown threshold. No nucleation occurs before the onset

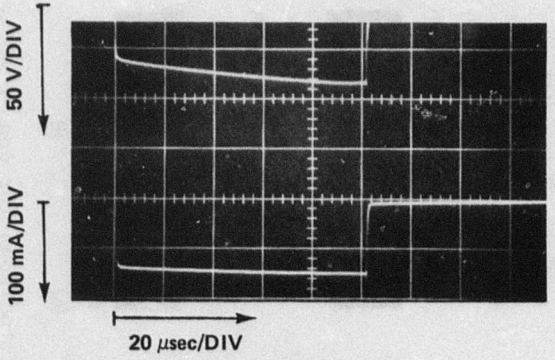

(a) 100-μsec PULSE WAVEFORMS

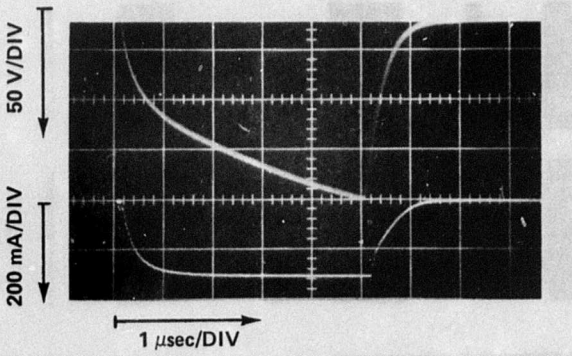

(d) 5-μsec PULSE WAVEFORMS

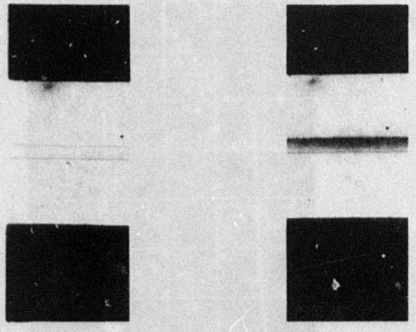

NO BIAS

(b) TRANSMITTED LIGHT PATTERN FOR DIODE WITH NO EXCITATION

(c) OPTICAL TRANSMISSION PATTERN FOR DIODE AT THE END OF THE 100-μsec PULSE

(e) HOT SPOT CONFIGURATION AT THE END OF THE 5-μsec PULSE

Figure 23. Separate pulses to be combined in double step pulse testing.

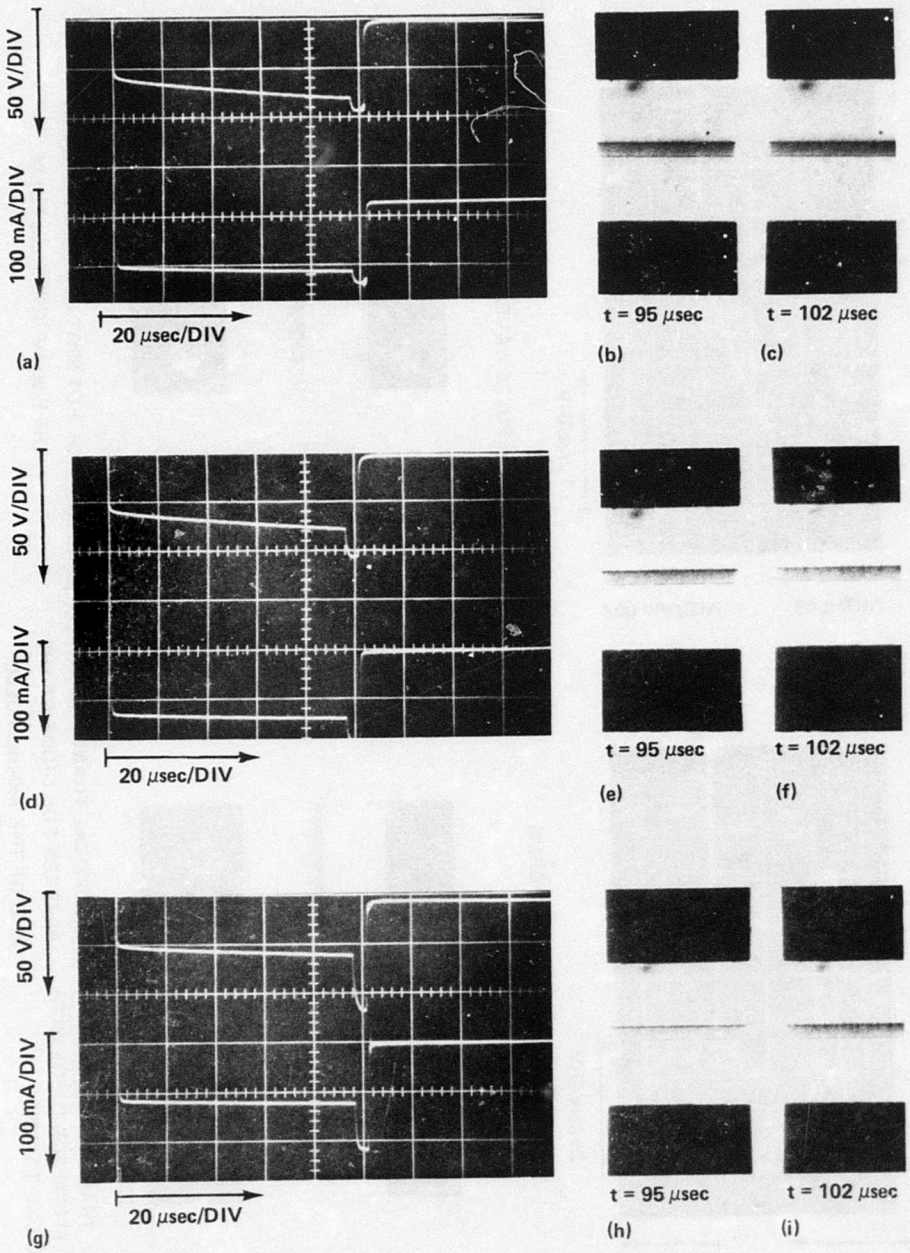

Figure 24. Waveforms and stroboscopic photographs for double pulse excitation with short pulse superimposed at the trailing edge of the longer pulse. (Times noted for the stroboscopic pictures refer to the waveforms to the left.)

of the secondary pulse, and the heating effects shown in Figure 24e are not as severe as those in Figure 24b. A larger number of dark spots appears in Figure 24f than in Figure 24c.

Finally, in Figure 24g, the amplitude of the secondary current pulse is increased to 100 mA. Comparatively little heating occurs before the beginning of the secondary pulse (Figure 24h), and the pattern of dark spots in Figure 24i is very similar in appearance to the pattern observed for the short pulse alone in Figure 23e.

As the amplitude of the secondary pulse is increased and the main pulse amplitude decreased, the dark spot configuration at the end of the pulse undergoes a gradual transition from that characteristic of the longer main pulse to the form observed for the short, high amplitude pulse. Even with a pulse amplitude small compared with the main pulse, the secondary pulse definitely alters the conduction pattern.

If the secondary pulse is set on the leading edge of the main pulse, four distinct second breakdown situations may occur, depending on the amplitudes of the pulses. These are illustrated in Figure 25 for a diode having 0.88 ohm-cm n-region. Primary and secondary pulse durations are approximately 100 and 12 μsec, respectively.

In Figure 25a, the primary pulse amplitude is about 90 mA and the amplitude of the secondary pulse is about 15 mA. Second breakdown occurs late in the pulse. The secondary pulse had little effect in this case.

The amplitude of the secondary pulse is increased to about 25 mA in Figure 25b. Second breakdown occurs during the short secondary pulse. There is a slight increase in the voltage accompanying the decrease in the current at the end of the secondary pulse, since the system is operating in the regime of negative differential resistivity. In this case the diode conducts in the second breakdown mode from the transition at about $t = 5$ μsec to the end of the entire composite pulse.

In Figure 25c, the secondary pulse amplitude is increased to 60 mA, and the primary pulse amplitude decreased to about 70 mA. The second breakdown transition again occurs during the secondary pulse, but in this case the primary pulse current level is not sufficient to sustain conduction in the second breakdown mode. Thus, at the end of the secondary pulse the diode relaxes into avalanche conduction and remains stable throughout the remainder of the pulse.

The fourth case, illustrated by Figure 25d, includes two complete second breakdown transitions. Rapid heating occurs during the early part of the pulse, and second breakdown occurs at $t = 8$ μsec. When the secondary pulse ends at $t = 12$ μsec, the power input is not sufficient to sustain conduction in the second breakdown mode. As the voltage increases with cooling (negative thermal coefficient of resistivity)

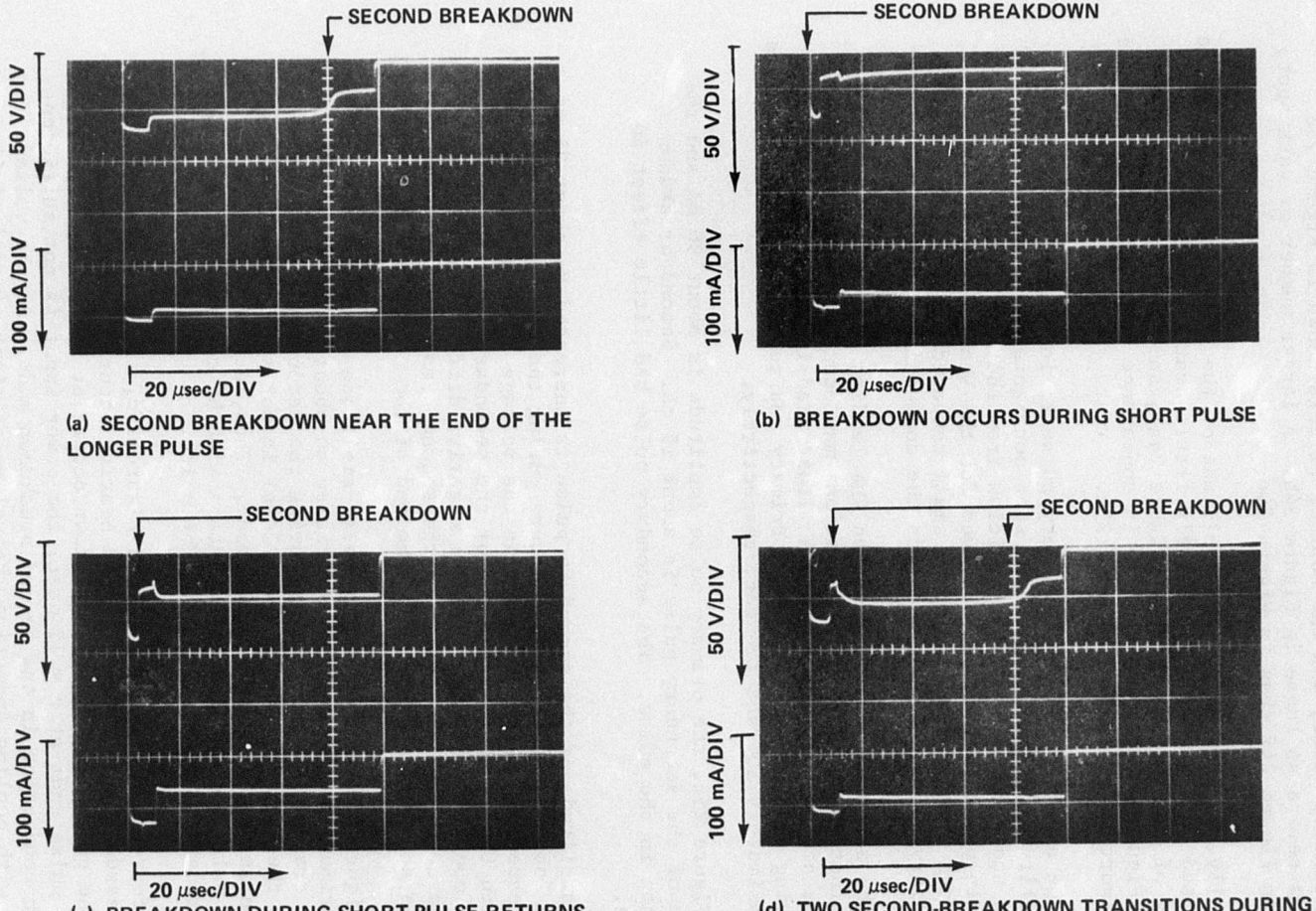

Figure 25. Four second breakdown cases for composite pulse with the short pulse superimposed at the leading edge of the longer pulse.

the power input begins to increase and the device again begins to heat up. At about t = 85 μsec the diode again goes into second breakdown.

The conduction patterns associated with a secondary pulse near the leading edge of the main pulse are shown in Figure 26 for a diode having a 0.146 ohm-cm n-region. The device is at the second breakdown threshold at the end of the secondary pulse, and again at the end of the main pulse. A pattern of about 14 current channels appears in Figure 26b, where the strobe is at the trailing edge of the secondary pulse. All but one of the dark spots fade away through Figures 26c and 26d. The junction remains quite hot, however, and at t = 40 μsec (Figure 26f) a new set of dark spots begins to nucleate. At the end of the pulse (Figure 26h), the system is again at the second breakdown threshold. With a small increase in current, second breakdown could occur either in the primary or secondary pulse, or even in both.

c. Discussion

A variety of effects related to filamentation and second breakdown occur when diode excitation is in the form of a composite controlled current pulse, composed of a short duration pulse superimposed on one of long duration. The nature of the results depends upon the relative amplitude and duration of the two superimposed pulses, and the timing between them.

If the short pulse is placed near the trailing edge of the longer pulse so that the excitation increases abruptly for a short time before the pulse ends, the increased current provides higher voltage drops parallel to the junction, creating a larger number of current filaments. Increasing the amplitude of the short pulse while decreasing the amplitude of the long pulse causes the pattern of dark spots at the end of the composite pulse to change gradually from the pattern characteristic of the long pulse alone to that of the short pulse alone.

When the leading edges of the short and long pulses coincide, so that the composite pulse starts out at a high amplitude, and quickly drops to a lower level for the remainder of the pulse, second breakdown may occur either during the initial high amplitude part of the pulse or, after some delay, during the lower amplitude part. If second breakdown occurs during the initial higher amplitude portion of the pulse the diode may remain conducting in the second breakdown mode or revert to avalanche conduction when the amplitude reduces to the lower level, depending on whether the lower current amplitude is sufficient to sustain the filamentary conduction.

Two second-breakdown transitions can occur during a single composite pulse if the pulse begins at a high amplitude and drops to an intermediate level. A second breakdown transition may occur during the initial high amplitude part of the pulse, and when the current is reduced to the intermediate level, conduction may drop to the avalanche mode. If the

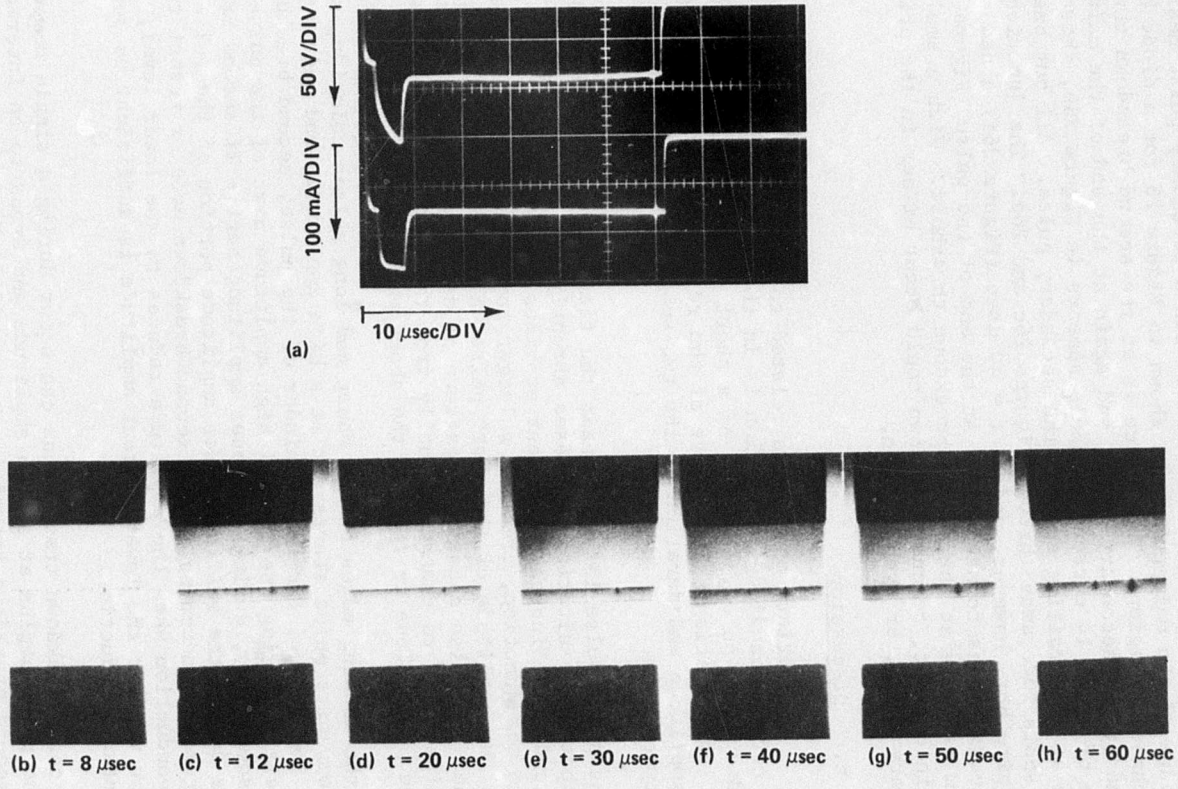

Figure 26. Stroboscopic sequence and waveforms for a diode at the second breakdown threshold near the end of the short pulse and the longer one. [The times noted for (b)-(d) refer to the voltage and current waveforms in (a).]

intermediate current amplitude is left on long enough, heating will eventually build up to the point where another second breakdown transition can occur at this reduced current level.

These experiments also demonstrated that there is no true steady-state multiple filamentation. It was reasoned that filaments formed at some current level might remain in the same configuration if the current were reduced to a level high enough that the filaments would not dissipate, but low enough to prevent further heating resulting in thermal runaway. But any change in the total current changes the transverse current components along the junction. Since it is the voltage drop parallel to the junction, associated with the transverse current component, which is responsible for the mechanism for multiple filamentation, the multiple filaments vanish within a thermal time constant after the current level is reduced, and the conduction pattern adjusts to fit the normal pattern for the reduced current level.

The conduction pattern at any time during a multilevel current pulse depends principally upon the amplitude at that time, rather than upon the history of conduction during the pulse. The transition in conduction pattern is not immediate, however, when the current level is changed. Delay in the transition occurs because of the thermal time constant associated with changes in the thermal distribution.

9. Transistor Experiments

a. Experimental Procedure

A wafer of silicon-on-sapphire integrated circuits containing a large number of accessible MOS-FET transistors was made available through the courtesy of Dr. D. J. Dumin of Inselek Company. Avalanche radiation and damage were examined in transistors of three different types as a function of source-gate bias. The intent was to determine how the device geometry and bias influenced the location of the second breakdown melt filament and the threshold for filamentation.

A test device consisting of two transistors and a diode, configured as shown in Figure 27, was included with each integrated circuit module on the wafer (about 450 in all). In the test device a rectangular area of n-type silicon was doped with boron to form p^+ regions as shown in the cross section of Figure 27b. An oxide layer was grown over the silicon, and openings through the oxide were etched for electrodes 1, 3, 5, and 6. The gate electrodes, 2 and 4, were deposited over the oxide and remained insulated from the silicon layer. Each of the transistors is end-to-end symmetrical; i.e., in FET-A, electrode 1 may be used as the source and electrode 3 the drain, or vice versa. Electrode 3 is common to both transistors. The electrical characteristics of the transistors are shown in Figure 28. Between electrodes 5 and 6 is a p^+-n diode.

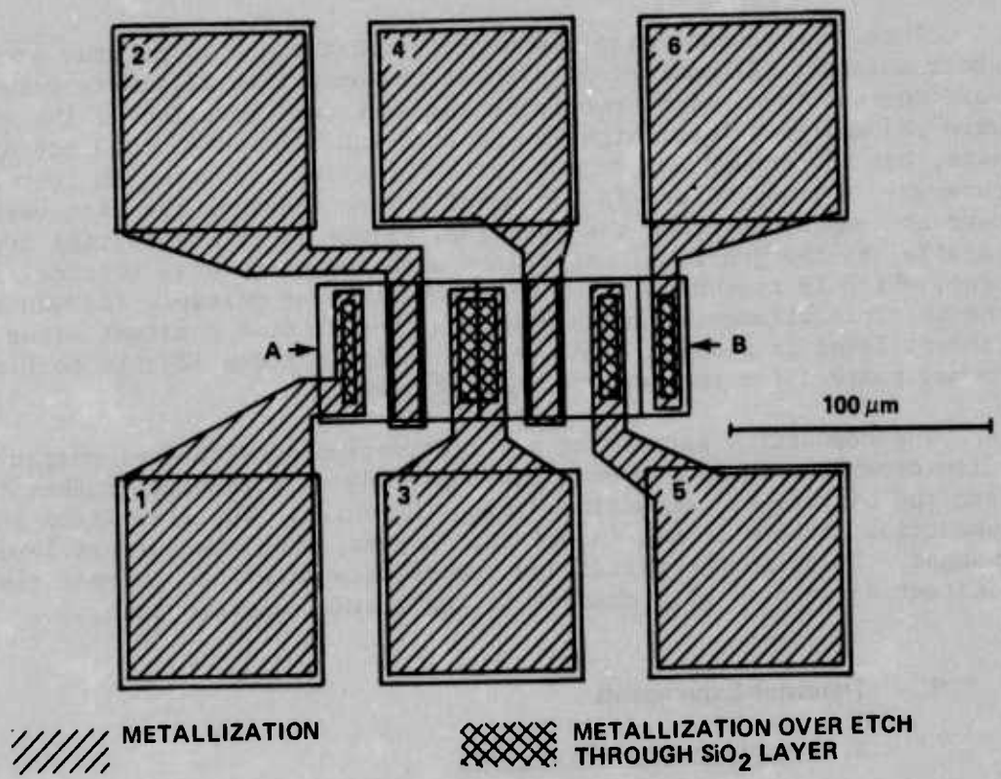

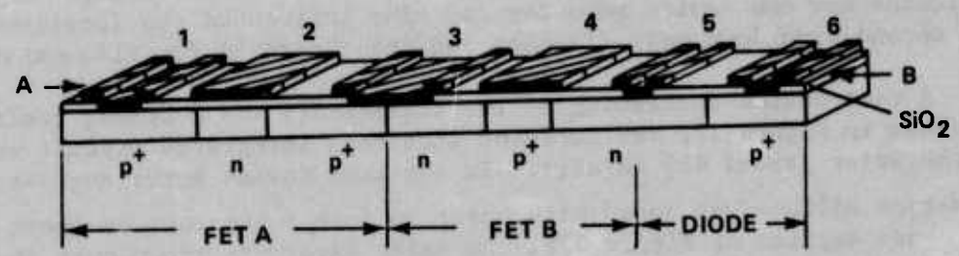

Figure 27. Configuration of silicon-on-sapphire MOS transistor test device. Two transistors and a diode are included.

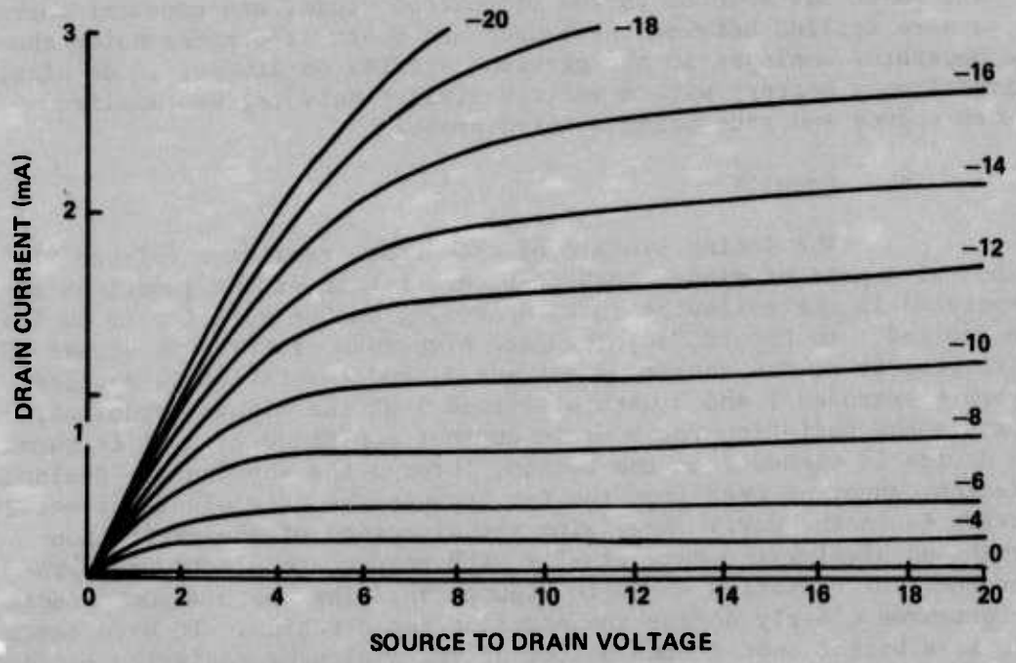

(a) n-GATE TRANSISTOR

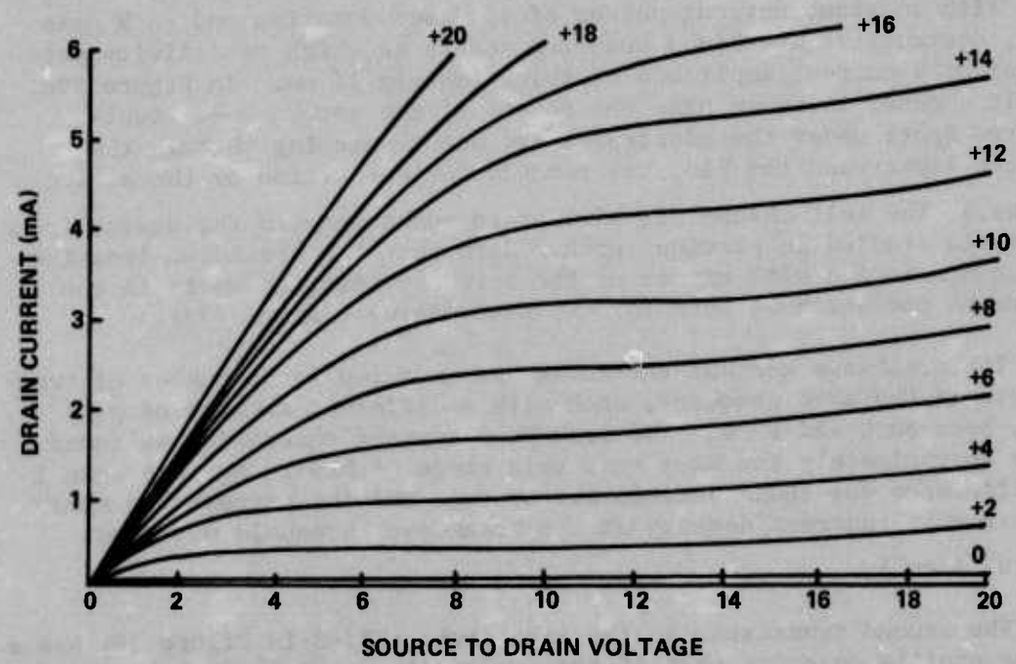

(b) p-GATE TRANSISTOR

Figure 28. Electrical characteristics of the transistors shown in Figure 27.

The wafer was mounted on the microscope stage, and constant current pulses were applied between the source and drain electrodes using the same apparatus employed in the previous studies on diodes. A dc bias, derived from a battery with a voltage divider network, was applied between source and gate using a third probe.

b. Results

The doping profile of each test transistor (Figure 27) is that of a pair of diodes back-to-back. Either of the junctions may be operated in the avalanche mode, depending on the polarity of excitation applied. In Figure 29a, the gate electrode of FET-A is biased -5 V with respect to the source, electrode 3, and excitation is applied between electrodes 1 and 3 with electrode 1 at the higher potential. The avalanche radiation for a drain current amplitude of 5 mA is shown. (The device is viewed from the bottom, through the substrate. Avalanche radiation cannot be seen from the top because the gate electrode metallization is in the way.) Reversing the direction of the excitation current and biasing the gate at -5 V with respect to electrode 1 produces the 5 mA radiation shown in Figure 29b. The two avalanche radiation pictures clearly define the edges of the n-region. In both cases there is a bright spot at the bottom of the avalanche radiation pattern, indicating an inhomogeneous current distribution. This behavior was observed in nearly all cases, but the presence of such a brightly radiating spot does not necessarily indicate a likely breakdown location.

With constant current pulses of 100-μsec duration and -5 V gate bias, destructive breakdown occurred across the high resistivity gate region at a current amplitude of approximately 11 mA. In Figure 29c, a melt channel is shown near the center of the gate. (The light-colored spots under the electrodes are due to etching through the silicon layer when the SiO_2 was removed for deposition of these electrodes.) The melt channel is similar in appearance to the damage found in diodes studied in previous work. Note that the breakdown location does not coincide with either of the brightly emitting spots in the avalanche radiation pattern for the same device (Figure 29a).

The breakdown current threshold was measured for a number of transistors of the same geometry, each with a different setting of gate bias, between 0 and 20 V. The breakdown current threshold was found to be approximately the same over this range of bias. No more than 1 mA difference was found between the average and the extremes in these measurements (current density at the breakdown threshold was about 2×10^4 A/cm^2).

The second transistor on the test strip (FET-B in Figure 27) has a doping profile opposite that of the device discussed in the above. The gate region is the more heavily doped portion. Figures 30a and 30b show avalanche radiation for 6 mA excitation with 5 V gate bias. When

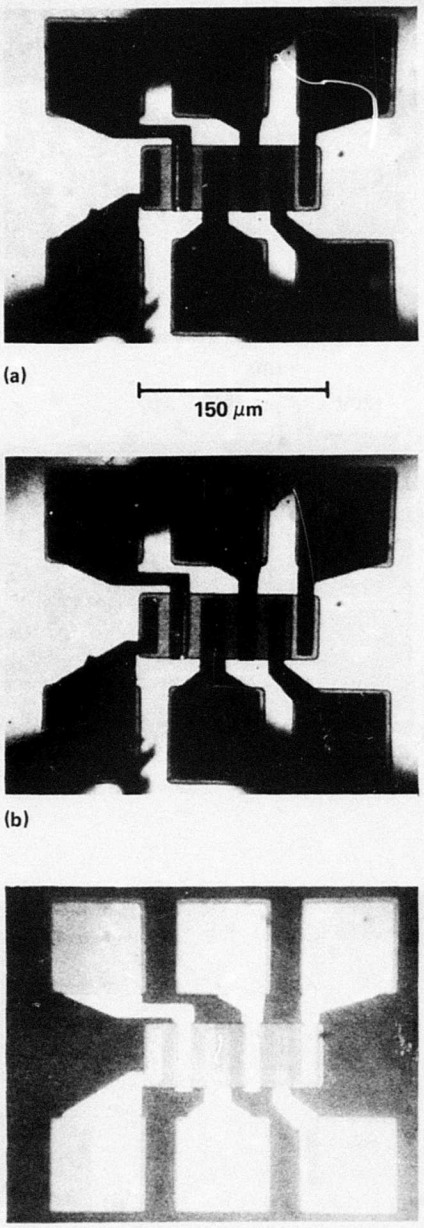

Figure 29. Avalanche emission in the two junctions of the n-gate transistor, shown in Figure 27, and a melt channel across the gate region.

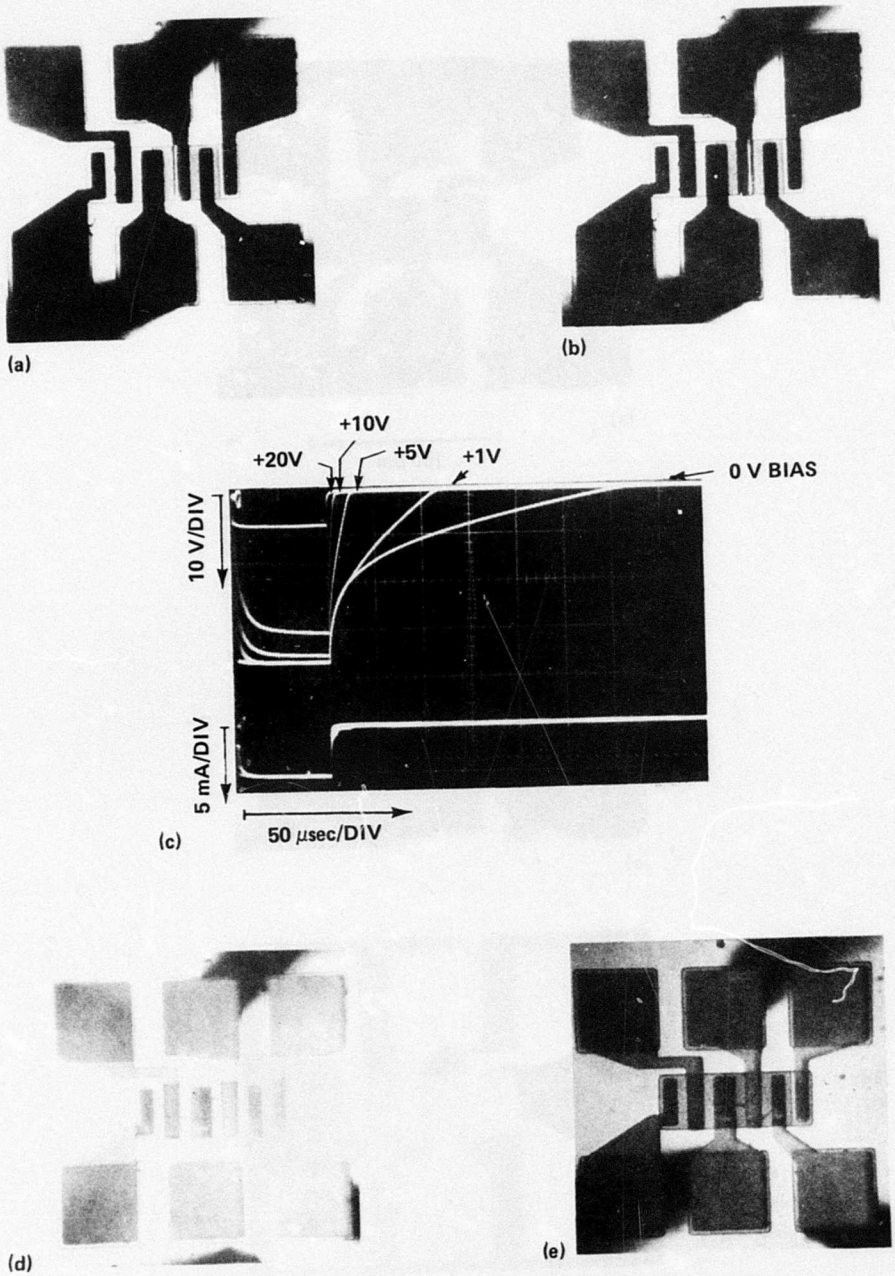

Figure 30. (a and b) avalanche radiation in the two junctions of the p-gate transistor of Figure 27, (c) waveforms for a fixed drain current at several bias levels, and (d and e) damage across the n-regions for two different transistors.

100-μsec constant current pulses were applied with 0 bias, the voltage trace displayed a long decay tail (Figure 30c) like that observed in avalanching diodes under similar test conditions. Increasing the bias level to 1 V causes a substantial reduction in the length of the decay tail, the voltage pulse amplitude remaining practically unchanged. With further increases in the bias voltage, the decay tail continues to shorten, and the voltage pulse amplitude decreases. The avalanche radiation decreases in intensity, and finally becomes extinguished as the bias is increased.

Since the gate region in FET-B is the more heavily doped part of the device, melt damage occurs in the higher resistivity n-regions between the electrodes, as shown in Figures 30d and 30e. The melt channels in Figure 30e are not connected through the p^+ gate material, which indicates that the two high resistivity regions broke down separately. The melt channel through the gate material (barely visible in the photograph) is connected to the melt in the right-hand n-region, but not to the melt in the left-hand n-region.

A third transistor type is shown in Figure 31. The drain electrode occupies the center of the device, with a gate on either side and source electrodes forming the outer boundaries. Thus there are four junctions in each transistor. Figure 32 shows the operating characteristics of the device.

Figure 33 shows five transistors side-by-side in the integrated circuit. The source connection is common to all of the transistors. Avalanche radiation in the central transistor at a current level of 10 mA and with -5 V gate bias is shown in Figure 33a. The radiation is fairly uniform at the left-hand gate, but on the right the emission is less intense except for a bright spot at the upper end of the junction.

Breakdown occurs in these transistors with 100-μsec constant current pulses when the pulse amplitude reaches approximately 65 mA. Again, no dependence of current breakdown threshold on gate bias was found. The current density at the breakdown was approximately 1.1×10^4 A/cm^2. Breakdown can occur in either branch of the gate, and frequently occurs at the upper end of the gate region. In the first two transistors from the right in Figure 33, the melt channel formed near the middle of the gate region, but in opposite branches in the two devices. In the third transistor (the one shown in avalanche in Figure 33a) a melt channel has formed at the upper end of the left-hand branch of the gate, whereas the very bright spot in the avalanche radiation pattern was at the upper end of the right-hand branch. In general, there was no correlation between locations of bright spots in the emission patterns and the breakdown melt filament locations.

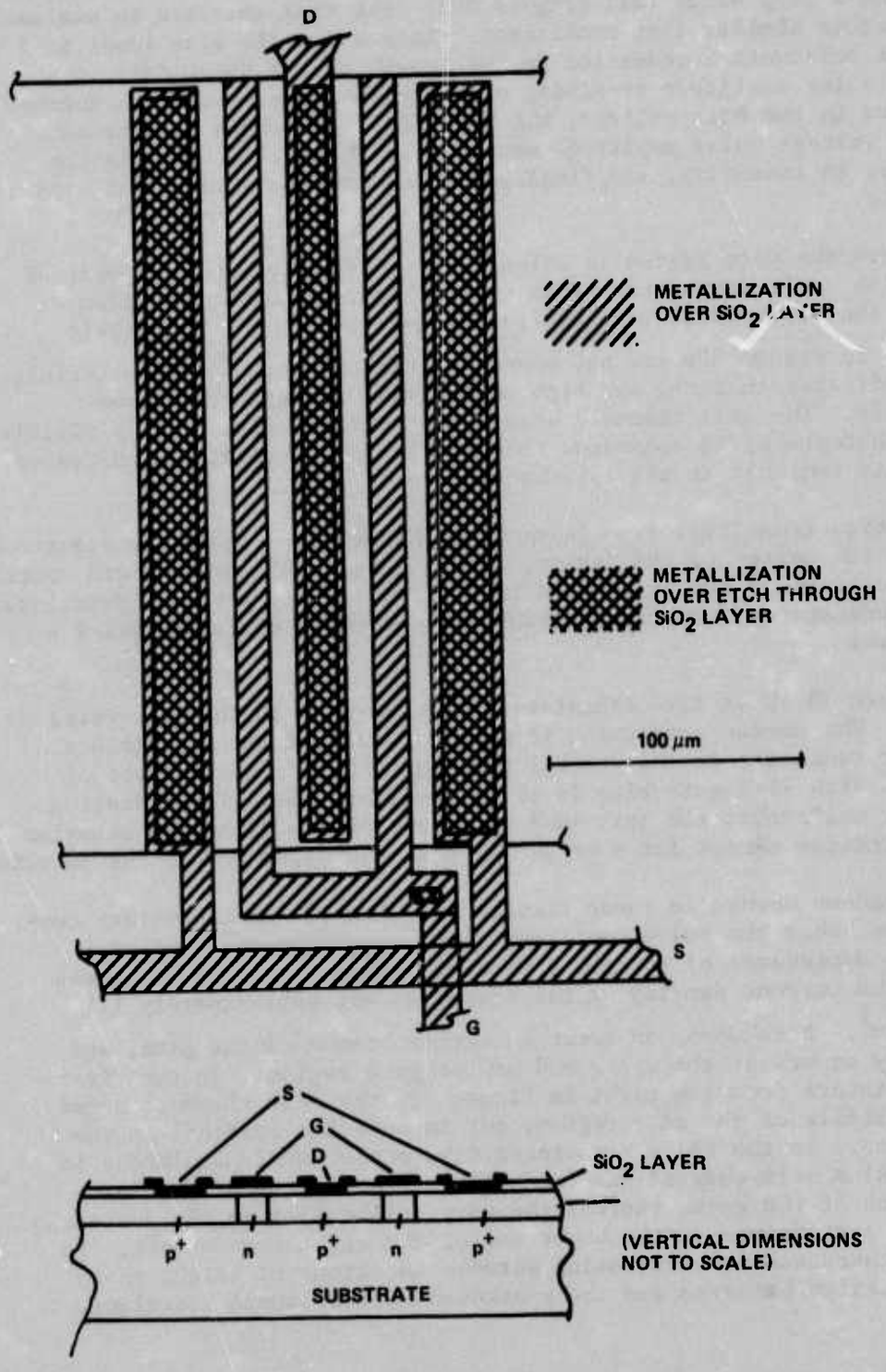

Figure 31. Configuration of silicon-on-sapphire MOS transistor used in an integrated circuit application.

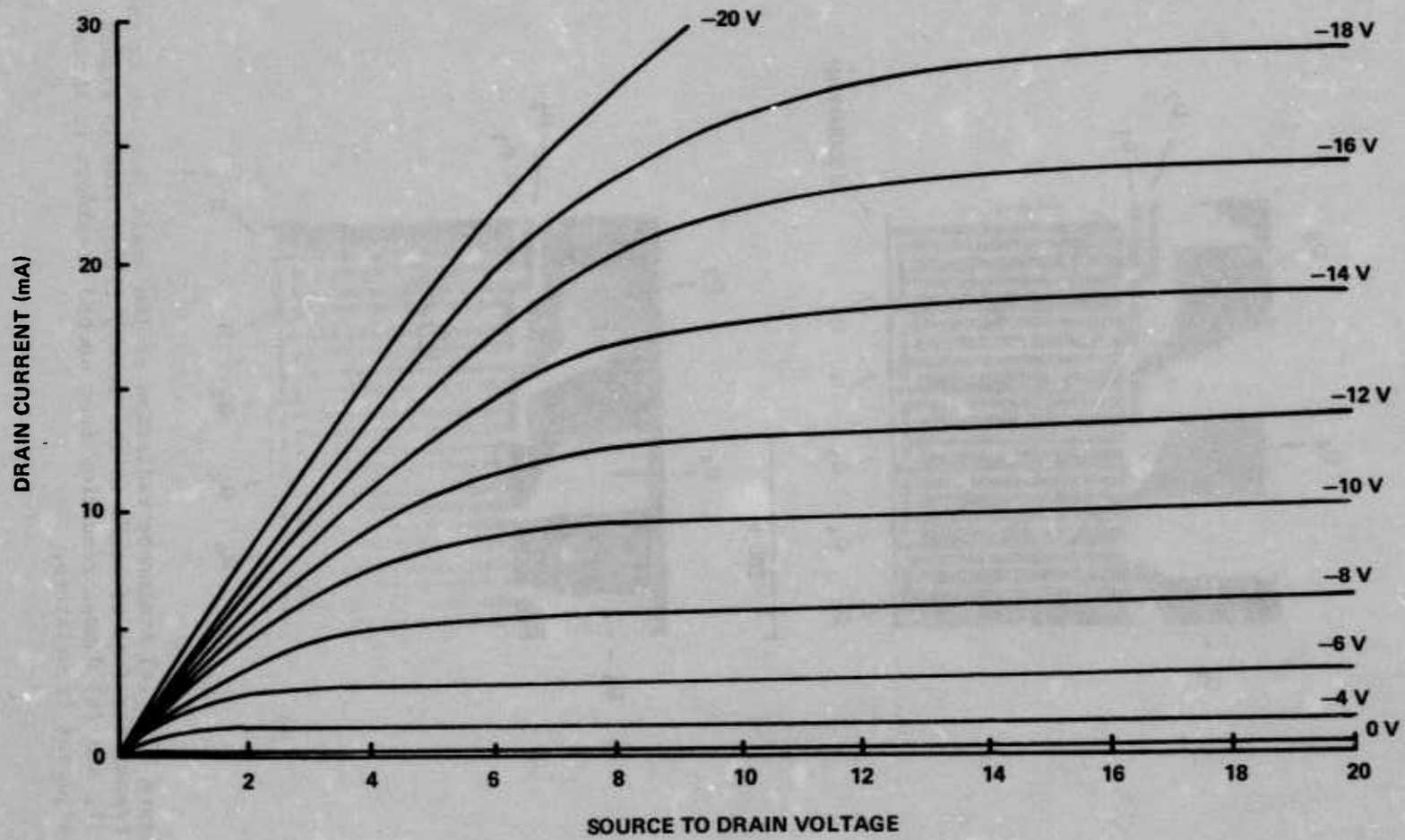

Figure 32. Electrical characteristics of the transistor illustrated in Figure 31.

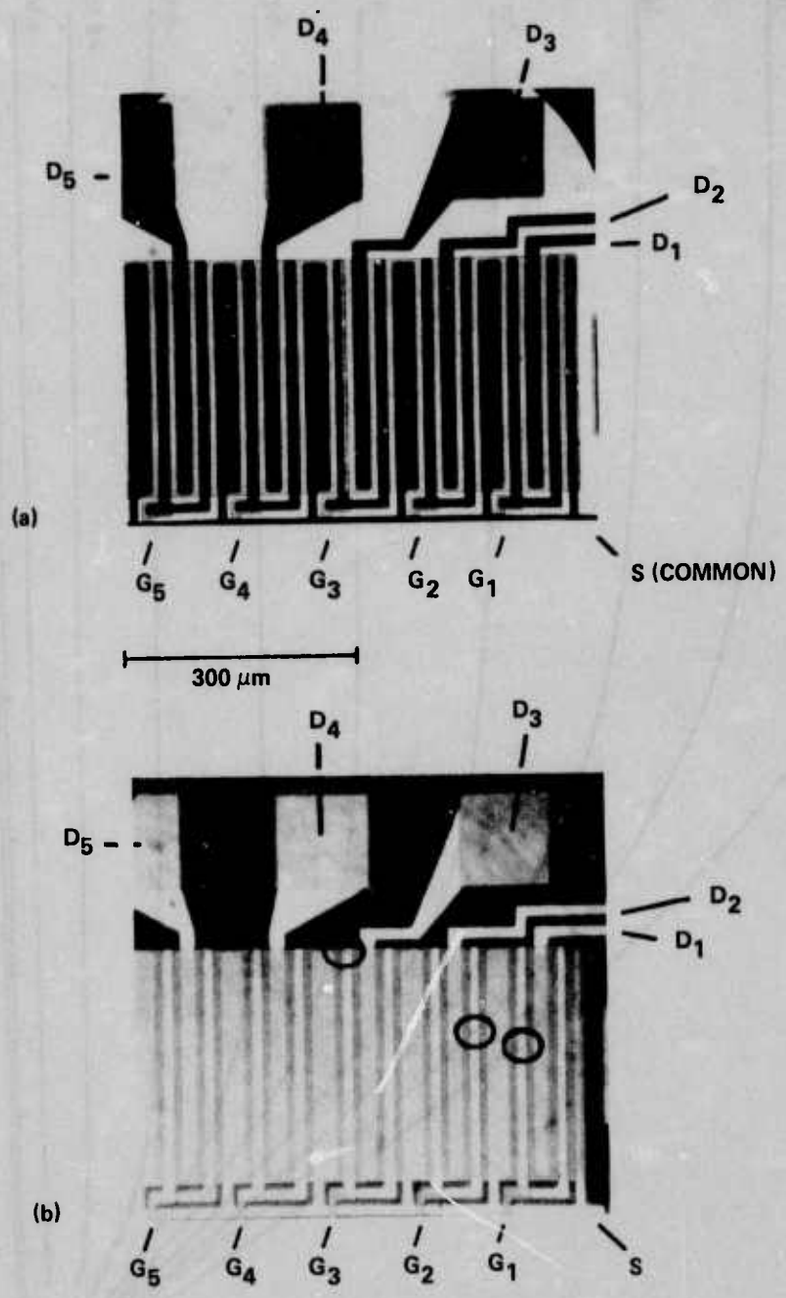

Figure 33. (a) Avalanche radiation at the drain junction in the transistor (one of eight in the array) illustrated in Figure 31, and (b) damage resulting from second breakdown in three adjacent transistors.

It was not possible to use the stroboscopic technique to observe thermal distributions in these devices since the junctions were located under the gate electrode metallizations. Transmitted light could be observed only in the bulk regions between electrodes. Use of the stroboscopic technique revealed darkening in the regions between the electrodes only after junction channeling had occurred and breakdown in the lower resistivity material was imminent.

A variation on the stroboscopic method was attempted, using reflected, rather than transmitted light. The nanolamp was placed at the entrance opening for reflected light on the microscope. All other components of the system were left unchanged. Light from the nanolamp passed through a beam splitter in the microscope and was focused on the bottom side of the sapphire chip. It was thought that increased reflectivity due to local heating should show bright regions to indicate the locations of hot spots.

Although bright regions did appear when melting occurred in the device, the attempt at deriving information from reflected light stroboscopy was generally unsuccessful. Reflection from the bottom side of the substrate cast an obfuscating illumination over the entire image. No change in reflectivity of the silicon material was apparent until a melt was formed. The melted channels showed up clearly, but no new information was thus provided, since the melt locations are easily found by post-breakdown examination of the resolidified material.

c. Discussion

Kennedy and Murley [26] have shown, using a computer simulation, that conduction in an insulated gate field effect transistor (IGFET) is nonuniform through the gate region, in general. In Figure 34, taken from their results, a constriction of the current toward the gate electrode is shown. The current density adjacent to the drain junction, however, remains fairly uniform, even in the presence of a gate bias. If filament nucleation leading to second breakdown originates at the avalanching junction, the current threshold for second breakdown would not be expected to depend strongly on the bias level.

If on the other hand, filamentation originates in the bulk material between source and drain junctions, the second breakdown current threshold should depend strongly on the gate bias, since the bias determines the degree of current crowding toward the gate electrode. A greater crowding effect would produce a higher current density about midway between the source and drain for a given total current through the device.

The authors have shown [6] that nucleation in the bulk material away from a junction, rather than at the junction is the exception in reverse-biased diodes, although such a phenomenon has been demonstrated in p^+-n-n^+ diodes having very low resistivity of the order of 1 ohm-cm or more in the region of highest resistivity, the nucleation mechanism at the junction dominates the filamentation sequence.

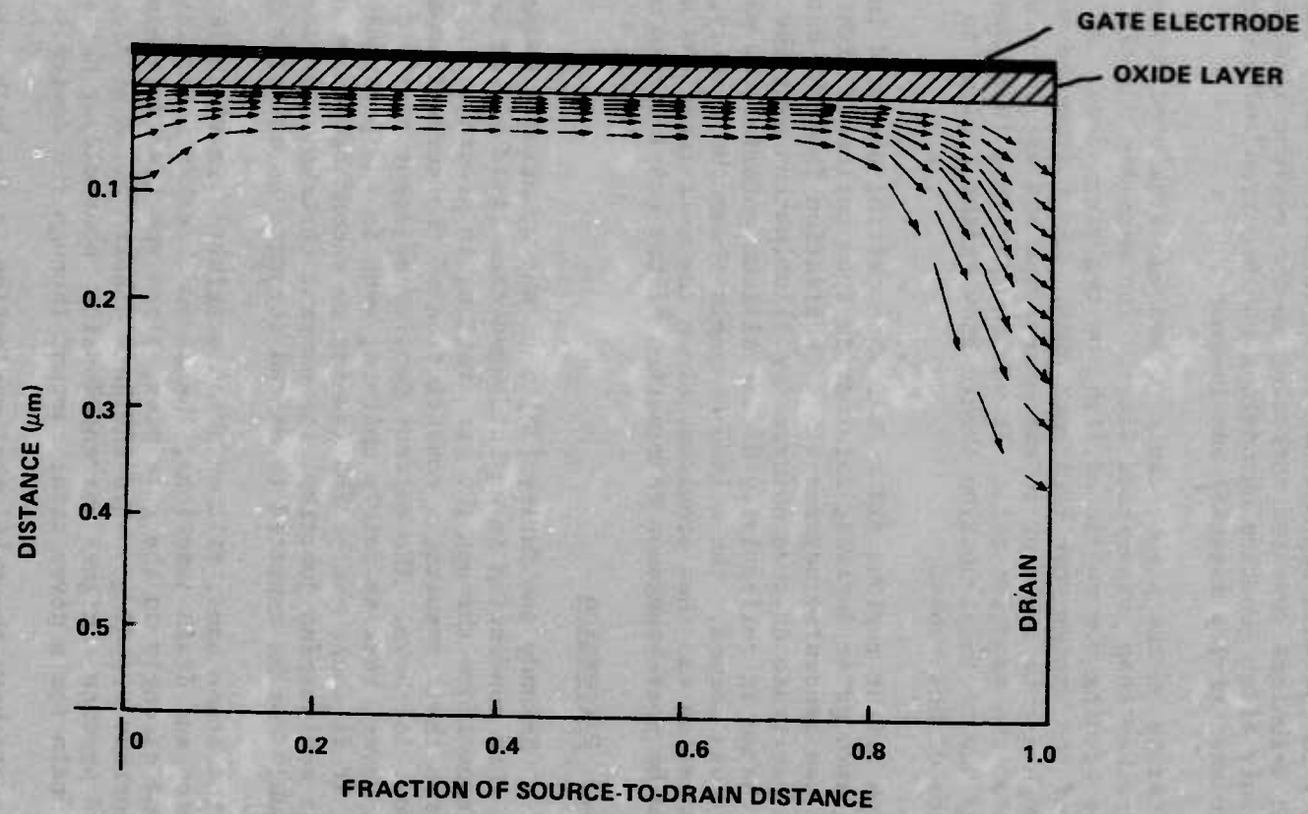

Figure 34. Current in an insulated gate field effect transistor (after Kennedy and Murley).

Although we cannot pinpoint the location of filament nucleation in the transistor structures by direct observation, all of the above considerations support the conclusion that second breakdown in these devices begins with filament nucleation at the reverse-biased (drain) junction.

10. Microstructure

a. Introduction

Although observations of dislocations in silicon have been performed for many years [27], we have not had experiences in such studies. Thus the first phase of the microstructure effort was to learn the techniques for observing dislocations. This has turned out to be more of a task than we anticipated and we have not completed it. The second phase is to compare devices with and without second breakdown damage and to clearly identify the damage sites, correlating observations by the different methods. The third phase is to study damage in transistors which have been subjected to second breakdown under conditions of different, but known, bias and different pulse amplitudes and durations.

The dislocation density in most devices is less than $10^5/cm^2$ [28]. It is desirable to obtain some estimate of the dislocation density accompanying a melt channel. A survey of the literature revealed no clear-cut method for doing this, so the following is offered as a first approximation. Let r be the radius of a melt channel, R the radius of the region surrounding the melt channel that is above 800°C during the lifetime of the melt channel (we assume dislocations can form and propagate if the temperature is above 800°C), h the length of the melt filament, and b the Burgers vector in silicon. The fractional change in volume of silicon upon melting is about 0.1 [29]. Starting with the expression for the volume of a cylinder, we can write the fractional change in volume as follows:

$$V = \pi r^2 h$$

$$\frac{dV}{V} = \frac{2dr}{r} + \frac{dh}{h} = \frac{3dr}{r} \quad .$$

The last equality assumes the system expands isotropically. The increase in cross-sectional area of the filament is

$$dA = 2\pi r dr = \frac{2\pi r^2}{3} \frac{dV}{V} \quad .$$

We shall assume that each dislocation is accompanied by an areal decrease of b^2. Thus the number of dislocations necessary to account for the expansion in cross section of the melt is

$$N = \frac{dA}{b^2} = \frac{2\pi r^2}{3b^2} \frac{dV}{V} \quad .$$

The number of dislocations per unit area is

$$n = \frac{N}{\pi R^2} = \frac{2}{3} \left(\frac{r}{bR}\right)^2 \frac{dV}{V} \quad .$$

Choosing $(r/R) = 0.1$, $dV/V = 0.1$, and $b = 3.84$ Å, we find

$$n = 4.5 \times 10^{11} \text{ dislocations/cm}^2 \quad .$$

The distance between dislocations on the average is

$$d_{avg} = (n)^{-1/2} = 1.5 \times 10^{-6} \text{ cm} \quad .$$

The time duration of a melt filament depends upon the test conditions. A representative time can be taken to be that of the thermal time constant of the system. In silicon-on-sapphire diodes this time constant is about 10 μsec; it is probably not much different from this in bulk silicon devices because the thermal conductivities of silicon and of sapphire are not greatly different. The dynamics of dislocation generation during such short times do not appear to be known at this time.

It should be noted that the long melt filament expands axially as well as radially and the axial expansion should be proportional to the length of the filament. Thus the end of the filament should not only be a region of high temperature but also of very high stress. This probably accounts at least partially for the shape of the filament.

The argument above leads to a dislocation density around a melt channel of about $4.5 \times 10^{11}/\text{cm}^2$ compared to that elsewhere in the device of about $10^5/\text{cm}^2$. The region of high dislocation density should be several microns in diameter, even for very short pulses. Hence this region should be discernible with a light microscope. A density of $4.5 \times 10^{11}/\text{cm}^2$, with an average spacing of 1.5×10^{-6} cm, is too high for resolution by an optical microscope, but is in the range of convenient observation of an electron microscope if the dislocations could be suitably tagged. The region of high dislocation density should be sufficiently large that it is discernible in x-ray topography.

In the above, we have been concerned with dislocations primarily as a diagnostic tool. In previous work [6], we have shown that imperfections play a secondary role in filamentation. Thus, we do not anticipate any correlations between dislocation densities prior to second breakdown and the location of the second breakdown melt channel.

The remainder of this chapter will be devoted to specimen preparation techniques and the work done in optical, electron, and x-ray microscopic methods.

b. Direct Observation of Dislocations

(1) Chemical Etching. Etching is the most widely used method for revealing dislocations on crystallographic surfaces. An etch pit will develop in the region of local strain and disorder where a dislocation line intersects a surface. By using a suitable etch, there exists a one-to-one correspondence between etch-pits and dislocation emergence points. The shape of the etch-pits depends on the particular etchant and on the crystallographic orientation of the surface being being attacked. The same etchant may give rise to variously-shaped pits depending on the symmetry of the crystallographic surface in question. A symmetric sharp-bottomed pit occurs when the dislocation line intersects the crystal surface normally. Angular inclination of the dislocation line gives rise to a sharp-bottomed but asymmetric pit. A three-dimensional network of dislocations can be exposed by a sequence of alternate polishing and etching operations. Plastic deformation is frequently accompanied by a polygonized network of dislocations.

(2) Methods of Observing Dislocations in Silicon

(a) Reflection Optical Microscopy. Etch pits can be observed with an optical microscope using different methods for illumination, polarization, and interference. Useful methods include the following:

1) Reflected white light (bright field) illumination.

2) Dark field illumination. In this case, the incident beam is allowed to fall obliquely on the object plane instead of at normal incidence as is done in bright field illumination. The light entering the microscope is that scattered by surface irregularities, which appear bright against a dark background.

3) Polarized light. Two crossed polaroids are set so that only those rays that are reflected from surface details with their plane of polarization altered are visible.

4) Phase contrast. Phase shifts introduced upon reflection are enhanced in the phase contrast arrangement by the addition of further phase shifts. The interference caused when the rays combine at the image plane may give enhanced contrast.

5) Interference contrast. A beam splitting arrangement provides the basis for interference effects between a reference beam and that reflected from the specimen.

6) Birefringence. When under stress, an isotropic material becomes birefringent; i.e., it has different indices of refraction depending upon the direction and polarization of the light. The state of stress around a dislocation causes variations in light intensity.

(b) Infrared Microscopy. Dash [30] employed infrared microscopy to study dislocations in copper-decorated silicon single crystals. To decorate the dislocations, copper atoms were diffused into the silicon at 900°C. Infrared light was used for observation because bulk silicon is transparent to infrared while it is opaque to visible light.

(c) Scanning Electron Microscopy. A finely-focussed electron beam scans the specimen surface, thus generating secondary electrons from the surface. The brightness of the beam in a CRO display is proportional to the intensity of the secondary electrons.

(d) Transmission Electron Microscopy. The electron microscope is capable, with suitable specimens, of resolving details of a few Angstrom's separation. However, the specimen must be sufficiently thin that the electron beam can pass through it without being strongly absorbed. Thus the bulk silicon device must be examined indirectly through the use of surface replicas.

(e) X-ray Topography. Dislocations in a crystalline lattice produce intensity contrast in diffracted x-rays. The slight variation in orientation of the diffracting planes about a dislocation cause a greater portion of the diverging incident beam to be diffracted by the dislocations than by the surrounding region.

c. Dislocations in Silicon Devices

Dislocations in silicon devices can be introduced in the various stages of device processing, such as crystal growth, slicing of wafers, epitaxy, diffusion of dopants, SiO_2 film deposition. Structural defects produced early in the processing sequence may generate additional defects upon further processing. No one-to-one correspondence between structural defects and electrical characteristics of devices has been found.

Most of the silicon single crystals used in device fabrication are grown by the Czochralski method. During the process of growing a single crystal from a melt, the quartz crucible containing molten silicon introduces considerable oxygen (about 10^8 atoms/cm^3) into the silicon. Oxygen then precipitates causing dislocations. The floating zone method produces crystals with lower dislocation densities. When compared to structural defects introduced by other processing steps, grown-in dislocations are fewer by four to five orders of magnitude [31]. Mechanical operations, such as slicing and lapping, produce damage to the surface

layers. These mechanical faults cause residual strain if not removed by fine polishing. Uncontrolled slip may be introduced by unrelieved strain upon further processing. Diffusion of phosphorous and boron as dopants initially generates sessile (stationary) dislocation loops of interstitials. These loops later interact to produce misfit dislocation loops. According to Dash and Joshi [32], diffusion in silicon takes place via extended interstitials and not vacancies. Epitaxial films and contaminants introduced during epitaxy, such as water vapor, oxygen and organic molecules, can cause defects in the substrate. The SiO_2 masking layer deposited on the surface of an epitaxial layer acts as a source of dislocations. In succeeding etching and diffusion operations, dislocations are produced by mismatch of the coefficients of expansion of the SiO_2 and silicon substrate.

d. Specimen Preparation

(1) Etching. An etchant selectively attacks the surface of the device, reacting more vigorously in regions of high strain. Thus pits are formed which can be seen upon microscopic examination. Prior to etching it is necessary to open the protective housing about the device, sever surface leads, and polish the surface to remove metallizations and passivating layers. The etches employed were those reported to be useful for observing dislocations in silicon.

(a) Dash Etch [30]

Composition: 1:3:10::HF:HNO_3:glacial acetic acid.

The etching time can be varied from a few minutes to overnight, according to the size of the pits desired. Deep etch-pits several hundred micrometers in diameter can be obtained.

(b) Vogel-Lovell Etch [33]

Composition: 3:5:3:2::HF(48 percent):HNO_3(70 percent):glacial acetic acid:3 percent aqueous.

Prior to etching, chemical polishing of the surface is necessary to produce a microscopically smooth surface. The polish used was:

CP_4 polish: 20:12:0.5::Conc. HNO_3:Conc. HF:Br_2 .

Deionized water is used to make the mercuric nitrate solution to avoid precipitation of mercuric chloride by chlorine impurities in distilled water. Etching the surface in the above solution for two minutes produced well-defined pits. Aging the etchant for about 6 weeks in a closed polyethylene bottle improves etching.

(c) Sirota-Tonoyan Etch [34]

Composition: 1:1:1::HF(37 to 38 percent): glacial acetic acid:HNO_3.

The temperature of the solution is maintained at 30° to 35°C and the etching time is 2 to 3 minutes. Etching time can be reduced by diluting with distilled water.

(d) d'Aragona Etch [35]

Composition: 1:2::0.15 molar solution of $K_2Cr_2O_7$:HF(49 percent).

Chemical polishing is recommended for 2 to 3 minutes prior to etching:

Polish: 3:2:2::HNO_3:CH_3COOH:HF .

d'Aragona showed that the etching rate is uniform at 1.5 μm/min. Etching, accompanied by ultrasonic agitation, for 5 minutes produces pits that are suitable for counting dislocation densities in crystals with resistivities between 1 and 10^4 ohm-cm. After a few minutes of etching, the solution turns brown-green due to the formation of Cr^{+++} cations, but the etching rate is not affected.

(2) Replication. Surface replicas for electron microscopy were prepared as follows.

(a) Negative Plastic Replicas. Deposit a drop of 1 percent formvar in dioxane on the wafer surface, drain the excess, and let dry. Transfer the plastic film onto a 400-mesh copper specimen grid.

(b) Direct Carbon Replicas. Vacuum deposit a coating of carbon 100 to 200 Å thick on the specimen surface. Remove the specimen from the vacuum chamber and deposit a drop of 1 percent formvar in dioxane on the carbon. Drain the excess. Lift the composite film by immersing in a water bath.

(c) Shadowed Replicas. Shadow casting is a means by which the hills and valleys of the replicated surface are made more contrasty. A layer of electron-dense material, such as gold, palladium, or platinum, is evaporated with the normal to the surface at an angle of about 45 degrees to the direction of the vapor beam.

e. Results

(1) Optical Microscopy. 2N3512 and 2N3245 epitaxial silicon transistors were opened to expose the silicon wafer inside. Wafer dimensions are 0.019 × 0.019 × 0.004 inch (2N3512) and 0.042 × 0.042 × 0.004 inch (2N3245). The protective SiO_2 film and metallizations were removed using a Buehler Vibromet polisher with 0.5 μm alumina abrasive. Using the Dash etch, the surface was treated for varying times, 40 to 220 seconds. Photomicrographs were taken at regular intervals so that the etch pattern could be observed as it developed. The sample was then repolished to remove all etch-pits and the process repeated. The same procedure was followed for the other etchants, varying the time as appropriate.

The Dash etch applied for 180 seconds to the 2N3254 transistors produced a dense pattern of triangular, flat-bottomed etch pits of varying sizes that covered the entire surface. Figure 35a shows a photomicrograph of a wafer prior to polishing, while Figure 35b shows the same region after polishing and etching. Long lines of overlapping etch pits closely following the contour of the oxide film are observed. The measured average dislocation density both within and outside the film pattern is $10^8/cm^2$. The pits located outside, between the finger-like projections, are shallow and randomly distributed, whereas the pits inside are deeper and linearly arranged. In the center, where one of the lead wires was attached, the pits are shallow and randomly distributed with the same average dislocation density. After 240 seconds of etching, short (1.5×10^{-3} cm) polygonized arrays of pits appeared as shown in Figure 35c. Prolonged etching failed to reveal more details.

The etch pattern for 2N3512 wafers after 40 seconds of etching with Dash etch produced sets of parallel V-bends (Figure 35d). Polygonized arrays of pits also took the shape of V-bends. With a total etching time of 80 seconds, the complex network, shown in Figure 35e, of intersecting V-bends appeared. The density of V-bends inside the remnant of the oxide film was low. The measured average distance between any two successive bends belonging to a single set is 2.5×10^{-4} cm. The spacing between bends of the same set was remarkably uniform.

In both the above cases, the oxide film configuration did not influence the etch patterns after the wafer surface was repolished to remove all traces of pits and was freshly etched.

Similar results were found with each of the etches. The long parallel etch pit lines signify residual strain introduced by oxide deposition and subsequent heat treatments. The V-bends are associated with the motion of dislocations in the epitaxial layer [36]. The triangular etch pits of etchants a-c and the circular pits of etchant d (Figure 35f) are indicative of the 111 orientation of the wafers.

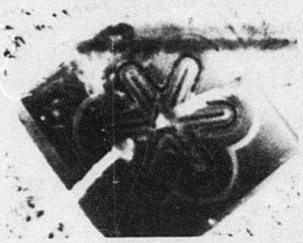

(a) UNTREATED 2N3245 TRANSISTOR WAFER

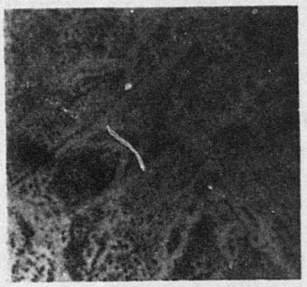

(b) SAME TRANSISTOR DASH ETCHED

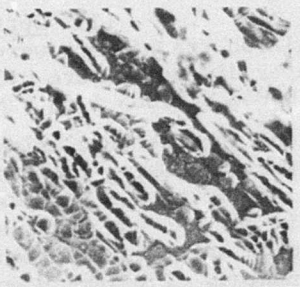

(c) SAME TRANSISTOR WITH FURTHER ETCHING SHOWING POLYGONIZED ARRAYS (WHITE LINES ARE CRACKS DEVELOPED DURING LAPPING)

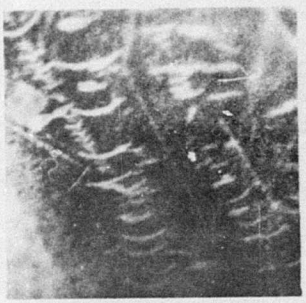

(d) TRANSISTOR 2N3512, DASH ETCHED

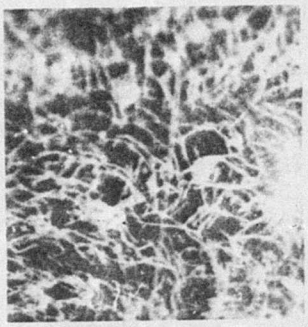

(e) SAME TRANSISTOR WITH FURTHER ETCHING

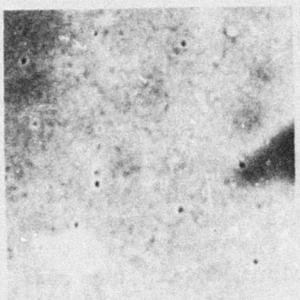

(f) DIFFERENT 2N3512 TRANSISTOR, d'ARAGONA ETCHED

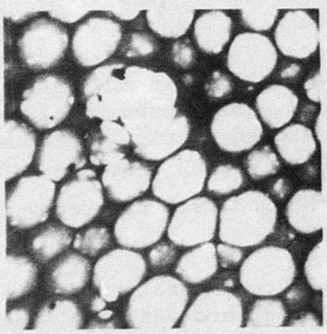

(g) MISFIT DISLOCATION NET, C-Pt SHADOWED REPLICA

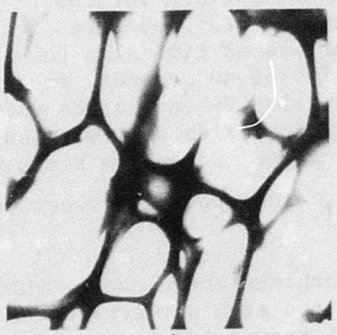

(h) ENLARGEMENT OF PORTION OF (g)

Figure 35. Optical (a-f) and electron (g,h) micrographs.

Optical microscopy of etched surfaces allowed ready observations of dislocations and comparison of these with the geometric configuration of the device.

(2) Scanning Electron Microscopy. The etched wafer was glued with silver paint to the aluminum specimen holder of an AMR1000 scanning electron microscope. Blurred outlines of etch pits were observed with poor resolution compared to the optical microscope. No useful information was obtained, perhaps because of poor electrical contact between specimen and specimen holder.

(3) Transmission Electron Microscopy. Replicas of the etched surfaces were C-Pt shadowed and observed with RCA-EMU2D and Philips EM300 electron microscopes. Polished wafers, both etched and unetched, were observed this way. Difficulty was experienced in lifting the replicas from the wafers. Typical dislocation arrays from etched surfaces are shown in Figures 35g and 35h. An average dislocation density of $10^8/cm^2$ was calculated from these micrographs. Although the dislocation density observed both optically and from replicas was the same, the specific features of the optical pattern could not be correlated with corresponding features of the electron micrographs. (Similar micrographs have been reported by others [32].)

(4) X-ray Topography. The Berg-Barrett camera arrangement for x-ray topography is shown in Figure 36. The camera which we are working with was copied from one designed by Newkirk [37]. Monochromatic radiation (Cu-Kα) and Kodak HRP plates are used with the camera. The x-ray topographic method requires that the crystal be accurately oriented so that the reflecting plane makes an angle of about 45 degrees with respect to the incident beam. The 211 reflection provides this condition. To orient the silicon wafer and to use it in the Berg-Barrett camera, the wafer has to be removed from its header and mounted on the x-ray goniometer. It is necessary to first orient the crystal approximately using the Laue method, and then to obtain the final adjustments in the Berg-Barrett arrangement. (A computer program was developed to reduce the problem of assigning indices to the zone axes measured in the Laue pattern. This program is available on request.)

There have been no x-ray topographic pictures taken to date because we have not yet succeeded in bringing the crystal into proper orientation.

f. Summary

Dislocations have been observed optically and with electron microscopy of surface replicas, but the patterns could not be correlated. The geometry of the dislocation pattern seen optically has been related to the geometry of the oxide pattern of the masking layer in the 2N3245 transistors to a depth of about 10 μm. Below this

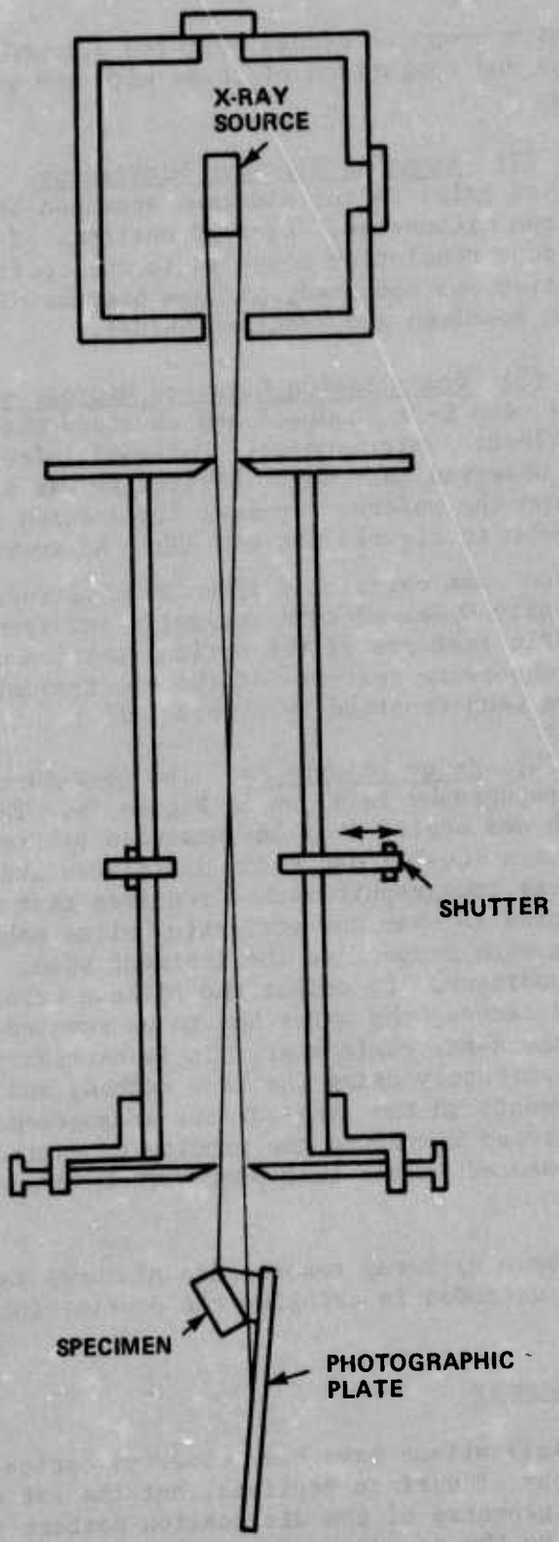

Figure 36. Berg-Barrett camera arrangement for x-ray topography.

depth the pattern is random. Few distinctive features were found in the 2N3512 wafers upon polishing and etching completely through the device. The general features observed (individual etch pits, linear arrays, polygonized arrays, networks of interacting dislocations, and V-pits) are similar in type and density to those reported by Dash and Joshi [32].

Thus far all the work done has been on control transistors in order to become familiar with the techniques and provide a basis for comparison with observations on damaged transistors. In the future, we intend to make a comparison between dislocation patterns of damaged and control transistors as revealed by etching and x-ray topography. Tests will first be done on specimens with visible damage to determine the feasibility of the entire approach. If feasibility is demonstrated, then tests will be made on devices damaged under known conditions, including different emitter base biases and collector-base pulse widths and amplitudes.

11. Summary

The influence of intense pulses of ionizing radiation on the onset of second breakdown has been investigated for diodes of different resistivity under both forward and reverse biases. Aside from a transient photocurrent spike, there is little effect from ionizing radiation unless the radiation intensity is within an order of magnitude of that required to vaporize parts of the device. For such intense illumination in devices with a high resistivity n-region and under reverse bias, the delay time to second breakdown increased. Measurements on diodes of different n-region resistivity show that there is an increase in the second breakdown delay time if the density of carriers generated by the ionizing radiation pulse is greater than the impurity doping density in the part of the diode having the highest resistivity. No change in delay time was observed in any diode operating in forward bias. The photocurrent spike is accompanied by a drop in voltage due to the circuit inductance. The circuit recovers in a time determined by its time constant. This is long enough for the highly localized hot filaments adjacent to the junction to cool appreciably.

The photocurrent accompanying irradiation is due to excitation of electrons from the valence to the conduction band. Study of the voltage and current waveforms, along with previous stroboscopic observations provides a direct means of monitoring thermal effects accompanying the laser irradiation. No evidence of heating due to laser radiation was detected, even when the laser intensity was 80 percent of the level required to vaporize parts of the device.

The complete lack of any detectable heating effect below the laser damage threshold, and the onset of vaporization immediately above the threshold indicates a sharp change in the absorption mechanism at some critical incident intensity. No intermediate damage level was found

wherein simple melting and resolidification occurs. There is either no damage at all or vaporization of parts of the silicon film occurs. The ionization effects do not change appreciably at the damage threshold; the intraband transitions occur as at lower irradiation levels. But the new absorption mechanism increases the absorption coefficient by more than a factor of ten within a few nanoseconds.

Current filamentation was investigated in thin silicon films with a parallel electrode geometry, since such a system had been analyzed previously. Films having high resistivities were damaged as predicted by earlier filamentation models, a narrow filament reaching from one electrode to the other through the center of the device. In very low resistivity films (0.01 ohm-cm or less), the turnover temperature T_2 is high and the (negative) slope of the resistivity-temperature curve is relatively small above T_2. These characteristics are favorable for large heat flow both parallel and perpendicular to the direction of the current. (Heat flow toward the electrodes was not included in the time-dependent computer simulation presented previously.) There is no ballasting of thermal gradients parallel to the direction of the current, so that a temperature buildup can occur midway between the electrodes. The result is a very small, isolated melt spot at the center of the square film. Since such a melt spot is usually quite small compared with the dimensions of the film and isolated from the electrodes, it has negligible effect on the conduction properties of the film.

Temperature measurements were made in silicon-on-sapphire diodes by combining the stroboscopic method with a photomultiplier system to permit measurements on devices during pulse testing. Fluctuations in the output intensity of the nanolamp light source required averaging over a large number of pulses for each point at which a temperature measurement was to be made. Spatial resolution was limited by the low transmitted light level through the hottest regions and the self-luminosity of these hot spots. The best spatial resolution achieved was approximately 0.5 mil, with a temporal resolution of about 1 μsec. The results of the time-resolved measurements showed that the lateral heat flow is an important factor in determining the temperature distribution in silicon-on-sapphire devices, but the greatest heat flux is into the substrate. Large thermal gradients exist in devices undergoing filamentation.

Attempts were made to anneal damage in silicon-on-sapphire diodes, subjecting them to self heating by a dc current. Both forward and reverse bias were applied, and annealing was carried out over times up to 76 hours. No improvement in I-V characteristics was found in any of the annealed devices. The only changes noted were of the nature of slight degradation of the I-V characteristic. Microscopic examination showed no detectable changes due to annealing in the diodes. The improvement of transistor characteristics as a result of annealing found by Brown [25] seems to be related to the relief of localized strains in the high resistivity parts of the device rather than a result of restructuring in the junction.

The use of a double step controlled current pulse for diode excitation in the stroboscopic apparatus showed that the conduction pattern at any time depends principally upon the current amplitude at that time; little influence is derived from the history of the conduction pattern during the pulse up to that time. When the pulse amplitude changes from one level to another the conduction pattern changes within a thermal time constant to that characteristic of the new level. Even if second breakdown occurs during a high amplitude part of the pulse, the diode may revert to avalanche conduction during a later low amplitude portion of the pulse. This allows the occurrence of more than one second breakdown transition in a single multilevel pulse.

Avalanche conduction and damage were observed in silicon-on-sapphire field effect (MOS) transistors using constant current pulse testing with dc gate bias. Damage occurred in the form of melt channels similar to those observed in silicon-on-sapphire diodes. Although bright localized emission spots occur when the source and drain junctions are operated in the avalanche mode, there is no correlation between these bright spots and the location of eventual breakdown filaments. The breakdown current level showed no appreciable dependence on the gate bias. Since the current away from the junctions is crowded into a narrow channel whose width depends on the bias, filament nucleation must originate at the reverse-biased drain junction, growing from that point across the high resistivity part of the transistor.

The attempt to find a convenient microstructure technique for evaluating hidden damage in bulk devices that had undergone second breakdown has been inconclusive. Improvements in technique are required before any assessment of the ideas can be made.

A significant result of the work of this study is that no observations of phenomena associated with second breakdown contradict the description of the second breakdown process as given in the Introduction.

REFERENCES

1. Sunshine, R. A., Avalanching and Second Breakdown in Silicon-on-Sapphire Diodes, Technical Report No. PRRL-70-TR-245, RCA Laboratories, Princeton, N.J., 1970.

2. Sunshine, R. A., and Lampert, M. A., "Stroboscopic Investigation of Thermal Switching in an Avalanching Diode," Appl. Phys. Lett., Vol. 19, 15 May 1971, pp. 468-470.

3. Sunshine, R. A., and Lampert, M. A., Second Breakdown Phenomena in Avalanching Silicon-on-Sapphire Diodes, Technical Report No. PRRL-71-TR-182, RCA Laboratories, Princeton, N.J., 1971.

4. Sunshine, R. A., and Lampert, M. A., "Second Breakdown Phenomena in Avalanching Silicon-on-Sapphire Diodes," IEEE Trans. Electron Devices, Vol. ED-19, July 1972, pp. 873-885.

5. Budenstein, P. P., A Survey of Second Breakdown Phenomena, Mechanisms, and Damage in Semiconductor Junction Devices, Technical Report No. RG-TR-70-19, US Army Missile Command, Redstone Arsenal, Alabama, December 1970.

6. Budenstein, P. P., Pontius, D. H., and Smith, W. B., Second Breakdown and Damage in Semiconductor Junction Devices, Technical Report AD 740226, US Army Missile Command, Redstone Arsenal, Alabama, April 1972.

7. Pontius, D. H., Smith, W. B., and Budenstein, P. P., "Filamentation in Silicon-on-Sapphire Homogeneous Thin Films," J. Appl. Phys., Vol. 44, 1973, pp. 331-340.

8. Budenstein, P. P., Pontius, D. H., and Smith, W. B., "Second Breakdown and Damage in Junction Devices," IEEE Trans. Electron Devices, Vol. ED-20, August 1973, pp. 731-744.

9. Flemming, D. J., "Thermal Breakdown Delay Time in Silicon p-n Junctions," IEEE Trans. Electron Devices, Vol. ED-18, February 1971, pp. 94-97.

10. Ferry, D. K., and Dougal, A. A., "Input Power Induced Thermal Effects Related to Transition Time Between Avalanche and Second Breakdown in p-n Junctions," IEEE Trans. Electron Devices, Vol. ED-13, August/September 1966, pp. 627-629.

11. Mars, P., "Thermal Analysis of p-n Junction Second Breakdown Initiation," Int. J. Electron, Vol. 32, January 1972, pp. 39-47.

12. Mars, P., "Analysis of the p-n Junction Second Breakdown Mode," Int. J. Electron, Vol. 32, February 1972, pp. 203-216.

13. Tasca, D. M., Peden, J. C., and Miletta, J., "Non-destructive Screening for Thermal Second Breakdowns," Proc. IEEE Conf. Nuclear and Space Radiation Effects, Seattle, Washington, July 1972, pp. 38-41.

14. Brown, W. D., "Semiconductor Device Degradation by High Amplitude Current Pulses," Proc. Conf. Nuclear and Space Radiation Effects, Seattle, Washington, July 1972, pp. 42-45.

15. Voss, P., "Infrared Observation of the Breakdown Behavior of High-Voltage P-N Junctions and P-N-P Structures in Silicon," IEEE Trans. Electron Devices, Vol. ED-20, March 1973, pp. 299-303.

16. Warren, A. C., "Reversible Thermal Breakdown as a Switching Mechanism in Chalcogenide Glasses," IEEE Trans. Electron Devices, Vol. ED-19, February 1972, pp. 288-289.

17. Sheng, W. W., Westgate, C. R., and Nguyen, H. P. F., "Thermal Switching in Chalcogenide Glasses," IEEE Trans. Electron Devices, Vol. ED-19, February 1972, pp. 288-289.

18. Larin, F., Radiation Effects in Semiconductor Devices, John Wiley and Sons, Inc., New York, 1968, pp. 216-231.

19. Smith, J. L., "Surface Damage in GaAs from 0.694- and 1.06-μm Laser Radiation," J. Appl. Phys., Vol. 43, August 1972, pp. 3399-3402.

20. Fountain, W. D., Osterink, L. M., and Massey, G. A., "Optically-induced Physical Damage to $LiNbO_3$ Proustite, and $LiIO_3$," pp. 91-97 in Damage in Laser Materials: 1971, NBS Special Pub. 356, SD Catalog No. C 13.10:356, US Government Printing Office, Washington, D.C., 1971.

21. Vershinen, Y. N., Soviet Physics-Solid State, Vol. 11, 1969, pp. 688-691.

22. Agranat, M. B., Krasyuk, I. K., Novikov, N. P., Perminov, V. P., Yudin, Yu. I., and Yampol'skii, P. A., "Destruction of Transparent Dielectrics by Laser Radiation," Soviet Physics JETP, Vol. 33, 1971, pp. 944-948.

23. Yablonovitch, E., "Optical Dielectric Strength of Alkali-Halide Crystals Obtained by Laser-Induced Breakdown," Appl. Phys. Lett., Vol. 19, 1971, pp. 495-497.

24. Fradin, D. W., Yablonovitch, E., and Bass, M., "Confirmation of an Electron Avalanche Causing Laser-Induced Bulk Damage at 1.06 μm," Appl. Optics, Vol. 12, April 1973, pp. 700-709.

25. Brown, W. D., "Semiconductor Device Degradation by High Amplitude Current Pulses," IEEE Annual Conference on Nuclear and Space Radiation Effects, Seattle, Washington, July 1972, pp. 42-45.

26. Kennedy, D. P., and Murley, P. C., "Steady State Mathematical Theory for the Insulated Gate Field Effect Transistor," IBM Journal of Research and Development, Vol. 17, January 1973, pp. 2-12.

27. Amelinckx, S., The Direct Observation of Dislocations, Academic Press, New York, 1964.

28. Marsden, C. P., Ed., Silicon Device Processing, NBS Special Publication 337, 1970.

29. Runyan, W. R., Silicon Semiconductor Technology, McGraw-Hill, New York, 1965, p. 213.

30. Dash, W. C., "Copper Precipitation on Dislocations in Silicon," J. Appl. Phys., 27, 1956, p. 1193.

31. Pomerantz, D. I., "Effects of Grown-In and Process-Induced Defects in Single Crystal Silicon," J. Electrochem. Soc., 119, 1972, p. 255.

32. Dash, S., and Joshi, M., "Diffusion-Induced Defects and Diffusion Kinetics in Silicon," Silicon Device Processing, NBS Special Publication 337, 1970, p. 214.

33. Vogel, F. L., and Lovell, L. C., "Dislocation Etch Pits in Silicon Crystals," J. Appl. Phys., 27, 1956, p. 1413.

34. Sirota, N. N., and Tonyan, A. A., Proc. Acad. Sci. U.S.S.R., Phys. Chem. Dect. (English Transl.), 134, 1960, p. 987.

35. d'Aragona, F. S., "Dislocation Etch for (100) Planes in Silicon," J. Electrochem. Soc., 119, 1972, p. 948.

36. Wang, P., Pink, F. X., and Gupta, D. C., "Structure Faults in Epitaxial and Buried Layers in Layers in Silicon Device Fabrication," Silicon Device Processing, NBS Special Publication 337, 1970, p. 288.

37. Newkirk, J. B., "The Observation of Dislocations and Other Imperfections by X-Ray Extinction Contrast," Transc. Met. Soc. of AIME, 215, 1959, pp. 485-495.